Quantum Light Emission from Waveguide-QED Systems with a Time-Delayed Coherent Feedback

by

Gavin Crowder

A thesis submitted to the University of Ottawa
in partial fulfillment of the requirements for the
Doctorate in Philosophy
degree in
Physics

Examining Committee

The following served on the Examining Committee for this thesis.

External Examiner:

Kanu Sinha
Assistant Professor, College of Optical Sciences and
Dept. of Physics, University of Arizona, USA

Internal Members:

Khabat Heshami
Adjunct Professor, Dept. of Physics,
University of Ottawa, Canada

Angela Gamouras
Adjunct Professor, Dept. of Physics,
University of Ottawa, Canada

Patrick Saull
Adjunct Professor, Dept. of Physics,
Carleton University, Canada

Supervisors:

Lora Ramunno
Professor, Dept. of Physics, University of Ottawa, Canada

Stephen Hughes
Professor, Dept. of Physics, Engineering Physics, and
Astronomy, Queen's University, Canada

Declaration of Authorship

I hereby certify that this thesis is entirely my own original work except where otherwise indicated. I am aware of the University's regulations concerning plagiarism, including those concerning consequent disciplinary actions. Any use of the works of any other author, in any form, is properly acknowledged at their point of use.

Abstract

To continue developing quantum technologies, such as quantum computing, quantum communication and quantum cryptography, we need reliable sources of quantum states of light. These quantum states of light can come in many forms; single photons, entangled pairs, bunched and anti-bunched light, all have uses in current quantum technologies, but for the best performance, this light must maintain its coherence. Time-delayed coherent feedback is a passive feedback method proposed for waveguide quantum electrodynamic systems to improve their performance and unlock new quantum optical phenomena. Additionally, due to its underlying non-Markovian dynamics, feedback is also an interesting theoretical problem to study. In this thesis, we use a quantum trajectory discretized waveguide (QTDW) model to simulate feedback dynamics and investigate its effects in a variety of applications. Originally proposed by Whalen in 2018, we develop the QTDW model beyond its initial implementation to now calculate quantum correlation functions, output spectra, waiting time distributions, and single photon source figures of merit. First, we present an explanation of quantum trajectory theory which is used to model the time dynamics in the QTDW approach, and discuss feedback in the linear regime to highlight the differences between Markovian and non-Markovian dynamics with coherent feedback. We next present nonlinear spectra and multi-photon effects from coherent feedback highlighting how the typical Mollow triplet is dressed by the feedback to create new resonances in the output field. This is followed by a collaborative theory and experiment work which observed our predicted non-Markovian signatures in the nonlinear output spectrum along with new non-Markovian phenomena in the linear regime. We then investigate how pulse-triggered single photon sources can be improved through the inclusion of a time-delayed coherent feedback, presenting the possible improvement to the performance figures of merit. Lastly, the modeling techniques developed for single photon sources with feedback are used to compare the performance of three new off-resonant driving techniques for on-demand single photon sources. These findings show time-delayed coherent feedback is an excellent degree of control to include in future waveguide quantum electrodynamic systems to unlock better performance and new phenomena in the system under investigation.

Acknowledgements

First of all I would like to thank my supervisors, Dr. Stephen Hughes and Dr. Lora Ramunno, for all of their support during my degree. Their advice and feedback have been a fantastic resource to help me grow as a researcher and generally as a professional. I doubt I could have reached the end of my degree without their tireless guidance and I could not have asked for better supervisors.

I would also like to thank Dr. Franco Nori for sponsoring me for an internship at the Center for Quantum Computing in the RIKEN research center. It was a fantastic opportunity to share my research and collaborate with world class quantum optics theorists.

Finally, I would like to thank my wife Karen for all of her support during many long nights of work over the last four years. Also for being a great sounding board whenever I was stuck on a math problem or coding bug, even though most of it sounded like a foreign language.

I was supported throughout my degree by the Natural Sciences and Engineering Research Council of Canada (NSERC) through the Canada Graduate Scholarship program.

Table of Contents

List of Tables

List of Figures

Chapter 1

Introduction

In 2003, Dowling and Milburn wrote that we are "in the midst of a second quantum revolution" [1]. The first quantum revolution was the discovery of quantum theory laid out in the early 20th century by Einstein, Schrödinger, and countless others [2–5]. This second revolution is the application of the ideas of quantum theory to develop new and useful technologies. The 100 year gap between theory and application was due to the engineering innovations which needed to be made to work at the quantum scale which are just now fully being used. At the time of their article, much of the quantum technologies they described were in their infancy. Twenty-two years later, the United Nations has made 2025 the "International Year of Quantum" and we have begun to see useful realizations of these technologies in both fundamental research and industrial applications. Most lauded in popular news, quantum computing has now shown quantum supremacy in a number of realized systems [6, 7] and quantum communication has allowed for fully quantum secure video calls between nations transmitted via satellite [8]. Less well known applications of quantum technology include quantum squeezed light being used in the LIGO experiment to detect gravitational waves [9, 10] and the development of modern atomic clocks, creating a new era of precision for the definition of our second [11]. These are just a few examples of how this second quantum revolution is pushing the bounds of our modern world.

Of course, there is still a long way to go to improve these quantum technologies for broad application in society, with both fundamental and engineering challenges for quantum scientists to overcome. If one asks a quantum scientist how long until there is a generally useful quantum computer, depending on their optimism one can get answers varying from 15-50 years (if they even think a quantum computer is possible to achieve). The reason for this apparent pessimism is the one common problem to all of these technologies, dissipation and scalability [12]. To scale beyond the laboratory clean rooms and cryostats, these tech-

nologies need to improve their fidelity (that is their rate of success) to overcome individual mechanisms of decoherence and loss that come with their sub-components. The race is on to be the first to build quantum systems with a high enough fidelity for fault-tolerant quantum computing and other highly sensitive quantum technologies, with billions being invested by governments and industrial partners to develop these systems [13, 14].

Driving all of these technologies is one aspect of quantum mechanics: entanglement. To use quantum to one's advantage, one must generate entanglement between two quantum objects that can then be used in any of the above applications. There are a variety of things that can act as a quantum object for this purpose, for example, photons [15–17], electrons [18, 19], neutral atoms [20, 21], ions [22–24], and larger nanoscale matter systems [25–30], have all been used to generate entanglement for quantum technologies. In this thesis, we will focus on the entanglement between light and matter and how that can be used to generate quantum states of light that are required to "power" the quantum technologies above.

The invention of the laser in 1960 [31], has given optics a powerful tool that generates high precision and high energy coherent photons. Quantum states of light go beyond this coherent light source, changing the underlying statistics of the photons. For a coherent source, the probability of finding n photons in a pulse containing an average of $\langle n \rangle$ photons follows the Poisson distribution; $P_n = \langle n \rangle^n \, e^{-\langle n \rangle}/n!$ and as a consequence, the variance is $\Delta n^2 = \langle n \rangle$ and there is no correlation in the arrival times of photons (mathematically, $g^{(2)}(t, t+\tau) = 1$). These two characteristics are a lower bound on classical light, but in quantum light one can violate these and have variances lower than $\langle n \rangle$ (this is squeezed light) and anti-correlated arrival times $g^{(2)}(t, t) < 1$ called sub-Poissonian light [32].

When a quantum light source produces photons with $g^{(2)}(t, t) = 0$, it is a single photon source, that is, it produces one photon at a time that can be used in quantum applications [33]. Additionally, single photons can be entangled together with a beam splitter to produce pairs of photons or more exotic states of light such as cluster states [15–17]. These quantum states of light are the engine that powers all of the photonic based quantum technologies of the future.

Improving the production of quantum light is an important area of research, and time-delayed coherent feedback has been proposed as a method of improvement in waveguide quantum electrodynamics (QED) systems [34]. It has been shown to improve the stability and coherent lifetime of photonic systems but is a challenging theoretical problem due to the underlying non-Markovian dynamics in the photonic system [35–48].

In this thesis, we present a theoretical model for time-delayed coherent feedback in waveguide-QED systems and investigate how coherent feedback can be used to improve

quantum light or generate new types of quantum light. Our model uses quantum trajectory theory and collisional waveguide models to calculate the nonlinear response of a quantum two level system coupled to a waveguide which coherently returns the two level system emission after a characteristic delay time.

1.1 Waveguide Quantum Electrodynamics

Generally, QED is concerned with the interaction between a quantum emitter and a quantum electromagnetic field. The different subfields of QED are defined by the type of electromagnetic field that the emitter is interacting with. This can be free space QED where the emitter interacts with a 3D propagating field, it could be cavity-QED where the emitter is embedded in a (quasi-) 0D cavity mode, or, as in this thesis, it could be a the interaction with a (quasi-) 1D waveguide mode [49]. The advantage of this type over the two former regimes is the inherently open nature of the waveguides which by design are nearly lossless. These can serve to engineer strong interactions between multiple emitters [50, 51], multiple photons [52], or emitter-photon interactions (which can be strong coupling between a single emitter and a single input photon [53–55] or between multiple emitters and photons [56–60]).

There are many platforms that can act as a waveguide platform for these interactions such as photonic nanowires [29, 61], plasmonic nanowires [62], optical nanofibres [63], superconducting nanowires [64], and Josephson junction arrays [65, 66]. But the most common waveguide platform are photonic crystals [67–74]. This is a periodic dielectric structure designed to have a band structure which either allows or forbids electromagnetic modes in certain frequency ranges [67]. A common manufacturing approach is to drill (with electron beam lithography) a periodic hole structure in a two-dimensional dielectric slab (such as GaAs or SiN) to create a (photonic) band gap around a frequency of interest. Then, by removing a row of holes, photons are restricted to travel down this row creating what is known as a "W1 photonic crystal waveguide" [69]. An example of this is shown in Fig. 1.1 along with other photonic crystal waveguide modes that can be made. There are many advantages to using these systems to host quantum interactions. Primarily, these waveguide systems have very low propagation loss [74] and support broadband coupling to quantum systems adjacent to the waveguide [68], allowing the photons produced from the quantum interaction to travel down the waveguide to be detected or used in other quantum systems without compromising the coherence. This feature is what allows multiple emitters to interact via the waveguide, leading to (for example) collective effects in the emitters [59, 75]. Additionally, the photonic crystal can be engineered beyond just hosting a waveguide

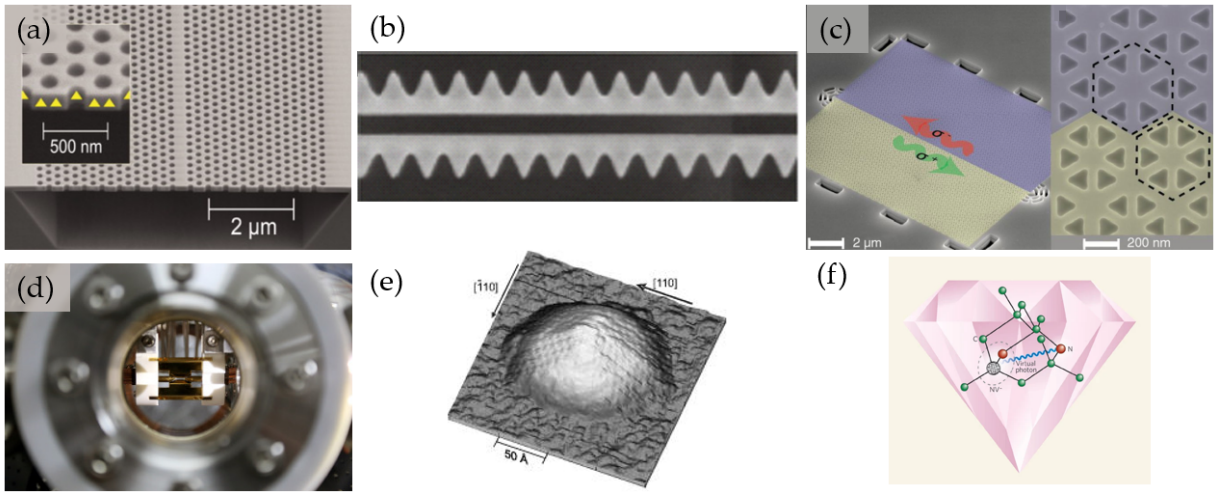

Figure 1.1: (a) - (c) Scanning electron micrograph images of three example photonic crystal waveguides. (a) A W1 photonic crystal waveguide from Sapienza et al. [69], (b) an "alligator" photonic crystal waveguide from Hood et al. [51], and (c) a topological photonic crystal waveguide from Barik et al. [73]. (d) - (f) Example quantum emitters that can be integrated in waveguide-QED systems: (d) trapped ions [24], (e) quantum dots [26], and (f) defect centers in diamond [25].

mode, but also feature locations of chiral coupling (where a quantum emitter will emit unidirectionally) [71, 72, 76], topological band states [73, 77, 78], or nonlinear dispersion in the waveguide [70, 79].

The *quantum emitter* also has many possible forms. Trapped or embedded atoms [80–82], quantum dots [29, 83–88], superconducting qubits [89], defect centers in semiconductors [90–93], and molecules [94, 95] have all been used for quantum light matter interactions in waveguide-QED systems. Some examples of these emitters in waveguide systems are also given in Fig. 1.1. Typically, these are chosen because an energy transition within the system can be isolated to act as a two level system, or a qubit. However, these are certainly not limited to two-level interactions and lots of work has been done taking advantage of some of the other energy transitions that are present. Dark states [96–99] and the biexciton cascade in quantum dots [100–103] are just two such examples.

With these platforms, many advancements in fundamental and applied quantum optics have been achieved. With a single emitter, coherent scattering of a resonant electromagnetic field can lead to complete reflection, single peaked emission [104, 105], or the appearance of sidebands [106–109] depending on the strength of the applied driving field. Pulsed excitation of a quantum emitter will lead to single photon emission [16, 29, 88, 110, 111],

but can also be used to study time-dependent resonance fluorescence [55, 112]. Embedding multiple quantum emitters in the waveguide can allow for collective sub-radiant and super-radiant effects to also be studied in both the Markovian [75, 113, 114] and non-Markovian regimes [59, 60, 115].

Before ending this brief introduction, we would like to highlight another experimental platform that realizes waveguide-QED phenomena, circuit-QED. Although the circuit-QED community typically uses different nomenclature from the waveguide-QED community both are built on the same theoretical framework. Where waveguide-QED experiments tend to operate at optical or near-optical frequencies, circuit-QED uses superconducting nanowires for its waveguides which host microwave modes [64]. Rather than a solid state emitter, superconducting transmon qubits are used which have an anharmonic energy level structure with the bottom two levels being isolated for use as the qubit [89]. These can couple to the nanowires with extremely high efficiencies [116], but lack the band structure engineering and chirality possible with photonic crystals. Nonetheless, circuit-QED has achieved a variety of waveguide-QED phenomena including resonance fluorescence [117–119], lifetime control [37], and collective effects [120–122].

1.2 Single Photon Sources

Single photons are quantum states of light which are a key resource for quantum technology applications. Using individual single photons and a beam splitter, one can create entangled photon pairs for use in quantum computing or quantum cryptography to name a couple applications [15]. Thus, a single photon source (SPS) is a key component in many quantum systems. But for use in quantum technologies, there are three requirements for an ideal SPS. First, it should be deterministic, meaning one could trigger the source to emit a single photon on-demand. Second, when it emits, it should produce one and only one photon. And lastly, the single photons that are produced are indistinguishable from each other, which is a key requirement in quantum applications [33, 87].

Probabilistic sources (i.e., not on demand) were the first robust single photon sources, producing high quality photons at the cost of low emission rates [123]. These types of sources like spontaneous parametric down conversion (SPDC) [124–127] and four wave mixing (FWM) [128] use nonlinear interactions in a crystal to generate pairs of photons, one of which is used to herald the arrival of the second photon that can be used as the SPS. However, because it is a probabilistic process, the emission rate is dependent on the probability for a pair to be generated. This is a compounding problem, where the rate of generating an entangled pair from this source scales with the square of the probability, an

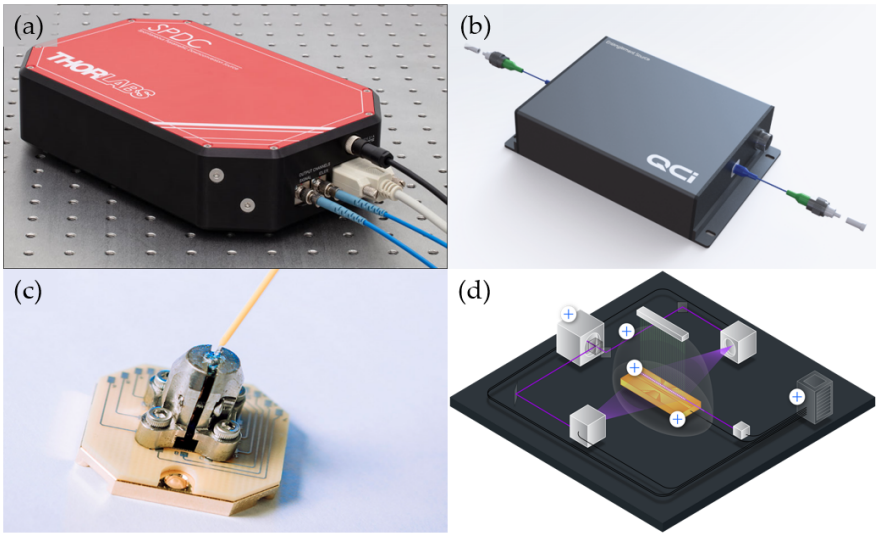

Figure 1.2: Commercially available single photon sources from (a) Thorlabs [137] and (b) QCi [138] based on SPDC, (c) from Quandela [139] using a quantum dot source, and (d) from IonQ using trapped ions (although only available as part of an integrated computing system) [140].

entangled triplet scales with the cube, etc. Even though work has been done to increase the emission from these sources into the MHz regime [125], larger entangled states (for use in technologies such as boson sampling) can quickly have emission rates as low as tens of events a day [129].

This is why *deterministic* sources have been pushed as the state of the art SPSs. A variety of platforms have been used as SPSs including superconducting transmon qubits [119, 130, 131], trapped ions [22, 23], neutral atoms [132, 133], spin-centers in solid state materials like diamond [90, 93, 134], and quantum dot sources [29, 84, 86, 88, 103], each with their own advantages and disadvantages. Individual systems have achieved near perfect efficiency, coherence, or indistinguishability but typically as a trade off with the other two figures of merit [103, 135], with newer systems working to maximize all three [136]. We are beginning to see industrial SPSs being created as a "plug and play" component for an optical laboratory. Figure 1.2 shows a selection of commercially available SPSs using a few of the different platforms above.

Regardless of the platform of interest, all SPSs suffer from three sources of error that reduce their performance. These are multiphoton emission events, non-radiative loss, and pure dephasing [87, 141]. The origin of these sources of error is different for each system and lots of research is being done to improve the stability, excitation schemes, and emission

rate of these systems for overall improvement of the SPSs [16, 142–145].

1.3 Time-Delayed Coherent Feedback

Feedback is the idea of using the output of a process in some way to improve the process and resulting output. It is well used across all kinds of engineering problems [146, 147] and occurs naturally in biological systems [148]. Feedback can be broadly categorized into two main categories: active or passive feedback. Active feedback takes a measurement of the output to inform changes that can be made to a part of the process. Passive feedback has the output of the process designed to partially feed back in and cause continuous adjustments without active oversight.

In quantum optics, active feedback (or measurement-based feedback) has been well used for improved fidelity of entangled state generation [149–151], stabilization of quantum states [152], and investigation of dynamical phases and quantum correlations [153, 154]. This is (typically) done with weak measurements of the output electromagnetic field to adjust some aspect of the quantum optical system like the driving field [155, 156]. By performing these measurements, there is a back-action on the quantum system which spoils the coherence between the output field and the emitter. Coherence is a key resource for quantum systems so preserving it as much as possible is ideal. This is where passive feedback such as a time-delayed coherent feedback has been proposed as a useful addition to quantum optical systems [34].

Time-delayed coherent feedback is an autological term, an optical feedback loop coherently returns the output photon field after a time delay. In waveguide-QED this can be achieved in two ways, either the waveguide loops around to couple with the quantum emitter in two locations or the waveguide is truncated by a mirror that reflects the field back to the emitter. This is shown schematically by Német et al. in Fig. 1.3 [157]. This feedback introduces non-Markovian behavior to the quantum emitter dynamics which poses a challenging theoretical problem to simulate these systems.

A Markovian system means that the evolution depends only on the state of the system at the *local time*, while a non-Markovian dynamic does not, and thus it can draw on information from the past. From a modeling perspective, this is problematic in quantum optical simulations because conventional techniques such as the master equation and the quantum regression theorem [32, 158, 159] rely on a Markovian approximation. Analytical work can be done using delay differential equations in the linear regime [36, 39–41, 160–166] or by making a Markovian approximation on the returning feedback, reducing it to

only picking up a round trip phase change [35, 167]. With these early techniques, work was done that predicted coherent feedback could enhance photon entanglement [40] and squeezing [41, 164], and stabilize optomechanics [39].

To move beyond these limited regimes, specialized techniques needed to be developed to account for the non-Markovian dynamic beyond the linear regime. The first of these techniques used fictitious cascading systems to create copies of the feedback loop that feed into each other and lift the non-Markovian nature [42, 168]. This is limited by the length of simulation that could be achieved, as the end time increases, the number of copies also increases until the Hilbert space becomes untenable. The primary technique used by the community is matrix product states which use a collisional model for the waveguide along with a Schmidt decomposition of the density matrix to reduce the Hilbert space complexity [38, 44, 46, 47, 169, 170]. This is a very powerful approach which can be difficult to implement but can simulate time dynamics, correlation functions, and additional loss channels. However, it is quite difficult and computationally intensive to include pure dephasing, a key aspect of simulating realistic quantum optical systems. To our knowledge only two papers have been published which include pure dephasing with matrix product states [171, 172].

A third model, the quantum trajectory discretized waveguide model is what we use to simulate coherent feedback in this thesis. This model was originally proposed by Whalen [173] and combines quantum trajectory theory with a collisional model for the waveguide. By using quantum trajectory theory, a stochastic simulation technique, the inclusion of additional loss channels including pure dephasing is straightforward with little additional computation necessary. Furthermore, monitoring the quantum jumps that occur can give us additional physical insight into the underlying physics beyond the ensemble average picture through observables such as the waiting time distribution.

Primarily, time-delayed coherent feedback has been studied as a theoretical and computational question, however recently experiments with feedback have begun to reach the non-Markovian regime required to probe the rich physics of these systems. These have been done with superconducting circuits and transmon qubits, initially in 2015 in the Markovian regime [37], but more recently non-Markovian feedback loops have been implemented for the generation of cluster states [17]. These experiments are highlighted in Fig. 1.3.

1.4 Layout of the Thesis

In this thesis, we investigate how quantum states of light can be produced with a time-delayed coherent feedback. We use the quantum trajectory discretized waveguide model

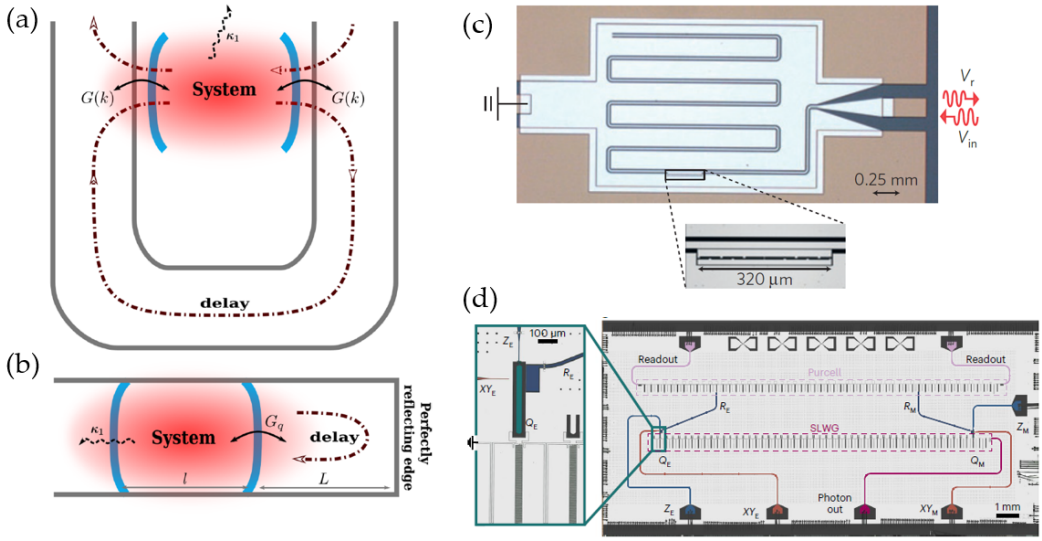

Figure 1.3: Two schematic representations of coherent feedback configurations from Német et al. [157]. (a) The quantum emitter is coupled to the waveguide at two spatial points separated by a time delay. (b) The quantum emitter couples at one location to the waveguide, but the waveguide is truncated by a perfect mirror, returning the emitter output after a time delay. In (c) and (d) two experimental realizations of feedback in superconducting circuits: (c) from Hoi et al. [37] in the Markovian regime, and (d) from Ferreira et al. [17] in the deep non-Markovian regime for cluster state generation.

and extend it to calculate spectra, quantum correlation functions, and single photon source figures of merit. We predict how feedback can affect the emitter's emission spectrum for both short and long delay times as well as the effects on the photon statistics. This is in agreement with an experimental collaboration which observed the additional feedback resonances and other non-Markovian effects in a superconducting circuit with feedback. We also investigate how single photon sources can be improved with feedback and also by using off-resonant excitation techniques to avoid polarization filtering.

An overview of the relevant topics has been discussed in this introductory chapter. In Chapter 2, we present background theory including a derivation of the master equation and quantum regression theorem to highlight the Markov approximation. We also present the formulation of quantum trajectory theory and show its equivalence to the master equation. We derive the equations of motion for feedback in the linear regime to give additional context to later chapters and include a discussion on Markovian vs. non-Markovian nomenclature. We end the chapter with a derivation of the single photon source figures of merit and a discussion of the computational methods used throughout the thesis.

In Chapters 3 to 6 we present published and submitted manuscripts, these are presented verbatim as they were (or will be) published with a preamble giving the context for the paper and noting any inconsistencies in the notation. Chapter 3 is a published manuscript on nonlinear spectra and multi-photon effects that arise from time-delayed coherent feedback. Chapter 4 builds on this with a submitted manuscript on an experimental collaboration which detects these nonlinear and non-Markovian feedback effects in a superconducting circuit with a transmon qubit system. Chapter 5 is a published manuscript showing how feedback can be used to improve single photon source performance in the presence of realistic decay channels. Chapter 6 follows the theme of single photon source improvement and is a submitted manuscript comparing three off-resonant excitation schemes for driving a single photon source. This is without feedback but uses the quantum trajectory approach for calculating the single photon source figures of merit developed in Chapter 5. Finally, in Chapter 7 we conclude and give recommendations for future work. Each of the bibliographies for the four manuscripts have been combined and are presented as a single bibliography at the end of the thesis for ease of reading.

Chapter 2

Background Theory and Methods

To highlight the non-Markovian nature of the results in this thesis, it is important to understand the Markov approximation and how it is applied in quantum optics and coherent feedback systems. We begin with a derivation of the master equation and quantum regression theorem to show how the Markov approximation is made. We then present the formulation of quantum trajectory theory, the method for time evolution simulation in the quantum trajectory discretized waveguide (QTDW) model. We also derive the analytic equations of motion for spontaneous emission in a coherent feedback system, specifically showing the difference between Markovian and non-Markovian results in this phenomena. Although the mathematics we use is Markovian, we describe the resulting dynamics as non-Markovian because of the non-instantaneous effects that are present. This results in non-exponential spontaneous emission decay from the quantum emitter which the quantum optics community commonly describes as non-Markovian. In general, all non-Markovian master equations can be represented by equivalent Markovian equations by expanding the Hilbert space of the quantum system. This is what is done in the QTDW model so although the mathematics is Markovian we continue to use the term non-Markovian to describe the results in keeping with the community's conventions. Lastly, we end with a discussion of the computational methods and software packages used to implement the QTDW model.

2.1 The Markov Approximation in Waveguide-QED Theory

To begin, we derive two key formulas in the theory of open quantum systems, the master equation (for the evolution of the density matrix) and the quantum regression formula (for the calculation of multi-time correlation functions). We highlight how both derivations rely on the Markov approximation which is no longer valid in a time-delayed coherent feedback system unless the mathematical "system" is expanded to include the feedback section of the reservoir (as is done in the QTDW and matrix product states approaches). The approach is adapted from derivations in [158] and [174] and describes a system (in waveguide quantum electrodynamic (QED) theory this is the quantum emitter coupled to the waveguide, e.g., a quantum dot, cavity with embedded emitter, etc.) and its interaction with a larger reservoir (the waveguide itself).

We denote the Hilbert spaces and orthonormal basis by $\mathcal{H}_S$ and $\mathcal{B}_S = \{|\phi_k\rangle_S | k = 1, 2, ..., d_S\}$ for the system with dimension, d_S, and $\mathcal{H}_R$ and $\mathcal{B}_R = \{|\phi_k\rangle_R | k = 1, 2, ..., d_R\}$ for the reservoir with dimension, d_R. The combined space is the tensor product of these; $\mathcal{H} = \mathcal{H}_S \otimes \mathcal{H}_R$ with basis $\mathcal{B} = \mathcal{B}_S \otimes \mathcal{B}_R$. This combined quantum system is closed so it can be described by the Schrödinger equation,

$$i\frac{d}{dt}|\psi(t)\rangle = H|\psi(t)\rangle, \tag{2.1}$$

where $|\psi(t)\rangle$ is a pure state and H is the Hamiltonian of the combined system. Note that throughout the thesis (aside from Ch. 6) we use natural units with $\hbar = 1$.

In general, the total Hamiltonian can be separated as

$$H = H_S + H_R + H_{\text{int}}, \tag{2.2}$$

where H_S is the Hamiltonian of the system, H_R is the Hamiltonian of the reservoir, and H_{int} is the Hamiltonian representing the interaction between the system and reservoir. This interaction term represents QED processes that cause dephasing, spontaneous emission, phonon absorption/emission, and other interactions of relevance in waveguide-QED phenomena.

The combined system density matrix is

$$\chi(t) = |\psi(t)\rangle\langle\psi(t)|. \tag{2.3}$$

This has a time evolution described by the von Neumann equation

$$\frac{d}{dt}\chi(t) = i\left[\chi(t), H\right], \tag{2.4}$$

derived by taking the time derivative of Eq. (2.3) and using the Schrödinger equation.

To derive the master equation, we define

$$\tilde{\chi}(t) \equiv e^{i(H_S+H_R)t}\chi(t)e^{-i(H_S+H_R)t}, \tag{2.5}$$

to transform into the interaction picture. By taking the time derivative of $\tilde{\chi}(t)$, we get

$$\frac{d}{dt}\tilde{\chi}(t) = i[\tilde{\chi}(t), \tilde{H}_{\text{int}}(t)], \tag{2.6}$$

where $\tilde{H}_{\text{int}}(t)$ is

$$\tilde{H}_{\text{int}}(t) \equiv e^{i(H_S+H_R)t}H_{\text{int}}e^{-i(H_S+H_R)t}. \tag{2.7}$$

Then by integrating Eq. (2.6), an explicit expression for $\tilde{\chi}(t)$ is found:

$$\tilde{\chi}(t) = \chi(0) + i\int_0^t [\tilde{\chi}(t'), \tilde{H}_{\text{int}}(t')]dt' \tag{2.8}$$

where we have used that $\tilde{\chi}(0) = \chi(0)$ by definition. Substituting this back into Eq. (2.6) for $\tilde{\chi}(t)$, we obtain

$$\frac{d}{dt}\tilde{\chi}(t) = i[\chi(0), \tilde{H}_{\text{int}}(t)] - \int_0^t [[\tilde{\chi}(t'), \tilde{H}_{\text{int}}(t')], \tilde{H}_{\text{int}}(t)]dt'. \tag{2.9}$$

This describes the evolution of both the system and reservoir. In general, the evolution of the larger reservoir is unaffected by the presence of the smaller system so we are interested in isolating for the system evolution. To do this we take the trace of the combined density matrix over the reservoir dimensions,

$$\rho(t) = \text{Tr}_R[\chi(t)], \tag{2.10}$$

so $\rho(t)$ is the system (or reduced system) density matrix. We also make the assumption that the interaction between the system and reservoir begins at $t = 0$, meaning that any off-diagonal elements of $\chi(0)$ are 0, which gives

$$\rho(0) = \text{Tr}_R[\chi(0)] = R_0'\chi(0), \tag{2.11}$$

where R_0' is a constant. We also define $R_0 = (R_0')^{-1}$ so that $\chi(0) = R_0\rho(0)$ for later use. Note that $R_0 = 1$ if the system and reservoir are initially uncorrelated.

Similarly, we can write the system density matrix in the interaction picture,

$$\tilde{\rho}(t) \equiv e^{iH_S t}\rho(t)e^{-iH_S t} = \mathrm{Tr}_R[\tilde{\chi}(t)], \tag{2.12}$$

and by tracing over the reservoir in Eq. (2.9) (and using the results in Eqs. (2.10) and (2.11)) we obtain the exact master equation in the interaction picture

$$\frac{d}{dt}\tilde{\rho}(t) = -\int_0^t \mathrm{Tr}_R\{[[\tilde{\chi}(t'), \tilde{H}_{\mathrm{int}}(t')], \tilde{H}_{\mathrm{int}}(t)]\}dt'. \tag{2.13}$$

To make Eq. (2.13) generally tractable, two approximations are made: the Born approximation and the Markov approximation. First, in the Born approximation, we take the coupling between the system and reservoir to be weak enough that the reservoir is unaffected. This approximation allows us to assume the combined density matrix only varies from its initial condition to first order in H_{int}. Then,

$$\tilde{\chi}(t) = \tilde{\rho}(t)R_0 + \mathcal{O}(H_{\mathrm{int}}), \tag{2.14}$$

and Eq. (2.13) can be written as

$$\frac{d}{dt}\tilde{\rho}(t) = -\int_0^t \mathrm{Tr}_R\{[[\tilde{\rho}(t')R_0 + \mathcal{O}(H_{\mathrm{int}}), \tilde{H}_{\mathrm{int}}(t')], \tilde{H}_{\mathrm{int}}(t)]\}dt'. \tag{2.15}$$

In this form, note that when the commutators are expanded, $\mathcal{O}(H_{\mathrm{int}})$ will only create terms which are second order or larger in H_{int}. From the Born approximation, we assume weak coupling and these second order terms are negligible, so we can remove $\mathcal{O}(H_{\mathrm{int}})$ to give

$$\frac{d}{dt}\tilde{\rho}(t) = -\int_0^t \mathrm{Tr}_R\{[[\tilde{\rho}(t')R_0, \tilde{H}_{\mathrm{int}}(t')], \tilde{H}_{\mathrm{int}}(t)]\}dt'. \tag{2.16}$$

Next, to make the Markov approximation, we assume that the future evolution of $\tilde{\rho}(t)$ depends only on the present state of the system. This allows us to replace $\rho(t')$ by $\rho(t)$ within the integral. Then the master equation in the interaction picture under the Born-Markov approximation is

$$\frac{d}{dt}\tilde{\rho}(t) = -\int_0^t \mathrm{Tr}_R\{[[\tilde{\rho}(t)R_0, \tilde{H}_{\mathrm{int}}(t')], \tilde{H}_{\mathrm{int}}(t)]\}dt' \equiv \mathcal{L}\rho. \tag{2.17}$$

where $\mathcal{L}$ is the general Liouvillian superoperator acting on ρ. Commonly, the Markov approximation is said to be valid as long as there is no back action from the reservoir

on the system. For any sufficiently large reservoir that satisfies the Born approximation, this condition is satisfied, as long as the reservoir is not engineered to create back action. However, in the case of feedback, the reservoir is exactly engineered to create back action from the feedback loop (part of the waveguide reservoir) onto the coupled quantum system. This is why coherent feedback is often referred to as a non-Markovian dynamic or non-Markovian reservoir in the literature.

Beyond the evolution of the density matrix, it is also useful to calculate multitime correlation functions in quantum systems. For example the first and second order correlation functions of a quantized electromagnetic field give information on the output spectrum and photon statistics respectively. The quantum regression formula is a prescription for calculating these quantities originally derived by Lax [175] which we derive here for a two-time correlation function to show its reliance on the Markov approximation. In the Heisenberg picture, this is

$$\langle O_1(t)O_2(t')\rangle = \mathrm{Tr}_{S\otimes R}\left[\chi(0)O_1(t)O_2(t')\right], \tag{2.18}$$

where O_1 and O_2 are operators that act on the system Hilbert space, $\mathcal{H}_S$. These both follow the Heisenberg equations of motion and so have solutions

$$O_i(t) = e^{iHt}O_i(0)e^{-iHt}, \tag{2.19}$$

and from the von Neumann equation (Eq. (2.4)) we have the solution

$$\chi(t) = e^{-iHt}\chi(0)e^{iHt}. \tag{2.20}$$

Substituting these solutions into Eq. (2.18) and using the cyclic property of the trace yields

$$\langle O_1(t)O_2(t')\rangle = \mathrm{Tr}_{S\otimes R}\left[O_2(0)e^{-iH(t'-t)}\chi(t)O_1(0)e^{iH(t'-t)}\right]. \tag{2.21}$$

Noting that O_2 only operates on the system, we can split up the trace over the system and reservoir to write

$$\langle O_1(t)O_2(t')\rangle = \mathrm{Tr}_S\left\{O_2(0)\mathrm{Tr}_R\left[e^{-iH(t'-t)}\chi(t)O_1(0)e^{iH(t'-t)}\right]\right\}. \tag{2.22}$$

The goal from here is to reduce this to system operators only so we need to continue to evaluate the trace over the reservoir. We first assume that $t' > t$ and set $\tau = t' - t$ then define the term inside $\mathrm{Tr}_R[\cdots]$ as

$$\chi_{O_1}(\tau) \equiv e^{-iH\tau}\chi(t)O_1(0)e^{iH\tau}. \tag{2.23}$$

This is the same form as Eq. (2.20) so satisfies the von Neumann equation with initial condition

$$\chi_{O_1}(0) = \chi(t)O_1(0). \tag{2.24}$$

The reduced system operator for this term is

$$\rho_{O_1}(\tau) \equiv \mathrm{Tr}_R\left[\chi_{O_1}(\tau)\right], \tag{2.25}$$

with initial condition

$$\rho_{O_1}(0) = \mathrm{Tr}_R\left[\chi(t)O_1(0)\right] = \rho(t)O_1(0), \tag{2.26}$$

where we have used that O_1 only acts on the system and the definition of the density matrix in Eq. (2.10). The last assumption we need to make is a Born approximation so that from Eq. (2.14) we can write $\chi(t) = R_0\rho(t)$ and

$$\chi_{O_1}(0) = R_0\rho_{O_1}(0). \tag{2.27}$$

Now, with Eqs. (2.25) and (2.27) and that $\chi_{O_1}(\tau)$ follows the von Neumann equation, these are the same ingredients that we used to derive the master equation above, so in the Born-Markov approximation we can write in an analogous way

$$\frac{d}{d\tau}\rho_{O_1} = \mathcal{L}\rho_{O_1}. \tag{2.28}$$

This gives the solution

$$\rho_{O_1}(\tau) = e^{\mathcal{L}\tau}\rho_{O_1}(0), \tag{2.29}$$

and this can go into the correlation function to get the quantum regression formula

$$\langle O_1(t)O_2(t+\tau)\rangle = \mathrm{Tr}_S\left\{O_2(0)e^{\mathcal{L}\tau}\left[\rho(t)O_1(0)\right]\right\}. \tag{2.30}$$

In a similar way, when $t' < t$, one can use the cyclic property of the trace to get

$$\langle O_1(t)O_2(t')\rangle = \mathrm{Tr}_S\left\{O_1(0)\mathrm{Tr}_R\left[e^{-iH(t-t')}O_2(0)e^{iH(t-t')}\chi(t)\right]\right\}, \tag{2.31}$$

and following a similar procedure to the above derivation the quantum regression formula is

$$\langle O_1(t+\tau)O_2(t)\rangle = \mathrm{Tr}_S\left\{O_1(0)e^{\mathcal{L}\tau}\left[O_2(0)\rho(t)\right]\right\}. \tag{2.32}$$

Both derivations rely on the Markov approximation to get the time evolution from t to $t+\tau$ when evaluating the multitime correlation function, and thus cannot be used when evaluating these correlation functions in the presence of feedback. As highlighted at the

beginning of this section, the non-Markovian dynamics are of the system with relation to the reservoir. Another way to approach simulating feedback systems is to include the feedback section of the waveguide in the system Hamiltonian rather than the reservoir Hamiltonian. This is what is done in the matrix product states approach and in the QTDW method used in this thesis. The mathematics then all remains Markovian and the quantum regression formula can be used, though the dynamics are still referred to as non-Markovian because it is conventionally taken to be from the perspective of the quantum system coupled to the waveguide. Thus, throughout the thesis when we refer to non-Markovian effects, we are referring to the dynamics of the coupled two level system as non-Markovian, even though all of the mathematics remain Markovian in the QTDW approach.

2.2 Quantum Trajectory Theory

In the QTDW model, our approach to simulating feedback systems in this thesis, the time evolution is done using quantum trajectory (QT) theory. In contrast to the master equation which evolves the ensemble average density matrix, QTs evolve individual realizations of the system ket vector which are averaged to find the ensemble average behavior. These can be used to calculate all of the same observables as $\rho(t)$, as well as additional insight into the behavior of individual trajectories which act like a single run in an experimental setup. Unique observables such as the waiting time distribution can be calculated (see Ch. 3, and we note it can be calculated for simple systems with analytic solutions) or we can use this insight to speed up calculations by simulating the experimental setups (see Ch. 5). The QT approach connects naturally to measurements made in experiments and this makes it intuitive to implement and understand. Additionally it is easy to include additional dissipation channels, a major advantage over other computational techniques which simulate coherent feedback such as matrix product states.

Another central advantage of QT theory lies in its computational scaling. By evolving the system ket vector, the computation time scales as $N \times d_S$ where N is the number of trajectories required to converge to the average behavior and d_S is the dimension of the system Hilbert space. The master equation approach scales as d_S^2, so for large Hilbert spaces, the QT technique can be more efficient for time evolution. In the feedback systems, we include the feedback section of the waveguide in the system Hilbert space as a collisional model which can increase the size of the Hilbert space past $d_S > 2500$ (e.g., $d_S = 2552$ for two photons allowed in the feedback loop and 50 bins used to model the loop, which we have tested against matrix product states, a numerically exact technique, and found is

sufficient even for extreme feedback with continuous wave (CW) driving fields [46]). Using a master equation becomes impractical as the computational memory becomes intractable and even on high memory workstations can be very slow to run. The QT approach is also fully parallelizable and convergence typically only requires a few thousand trajectories (though greatly depends on the dynamics being simulated), so can be much faster than the master equation approach.

QT theory was developed simultaneously in three research papers all in 1992, Dalibard et al. [176], Tian and Carmichael [177], and Dum et al. [178], with a full pedagogical development in Carmichael's *Statistical Methods in Quantum Optics 2* textbook [159]. Since then, it has been used to describe phenomena in a variety of quantum optic research papers such as bunching and antibunching in two coupled two level systems [179], stationary inversion via off-resonant pumping [180], entanglement optimization [181], and is well used in non-Hermitian quantum optic system modeling [182–184] in addition to time-delayed coherent feedback [46, 173, 185].

To use QT theory, two components are necessary for the evolution. The system Hamiltonian, H_S, and the dissipation operators, C_j, that represent the interaction between the system and reservoir. For equivalence to the master equation evolution, the dissipation operators must take the well known Lindblad form

$$\mathcal{L}_{\text{diss}}(\rho(t)) = -\frac{1}{2}\sum_j (C_j^\dagger C_j \rho + \rho C_j^\dagger C_j) + \sum_j C_j \rho C_j^\dagger, \tag{2.33}$$

and j runs over as many operators as are needed to describe the system-reservoir interaction. These dissipation operators can represent (for example) spontaneous emission, pure dephasing, incoherent pumping, and phonon-induced interactions. In QT theory, these C_j operators are called *quantum jump* operators and lead to the stochastic dynamics underlying each individual trajectory.

The following is a simplified explanation of the QT process, with a more in depth mathematical explanation afterwards. To evolve a single quantum trajectory, one begins with a pure initial state (which can be initialized through stochastic projection of an initial mixed state) which is evolved under an "effective" *non-Hermitian* Hamiltonian, H_{eff}, until the condition for a quantum jump to occur is met. The jump is applied, and evolution under H_{eff} begins again, until another jump occurs or the end time is reached. This trajectory, and any desired observables, are then averaged along with many other simulated trajectories to get the ensemble average behavior. This process is schematically shown in Fig. 2.1.

Mathematically, let the initial state of the system be $|\psi(0)\rangle$ and the length of each time step be δt. At the beginning of each time step, we stochastically decide whether one of the

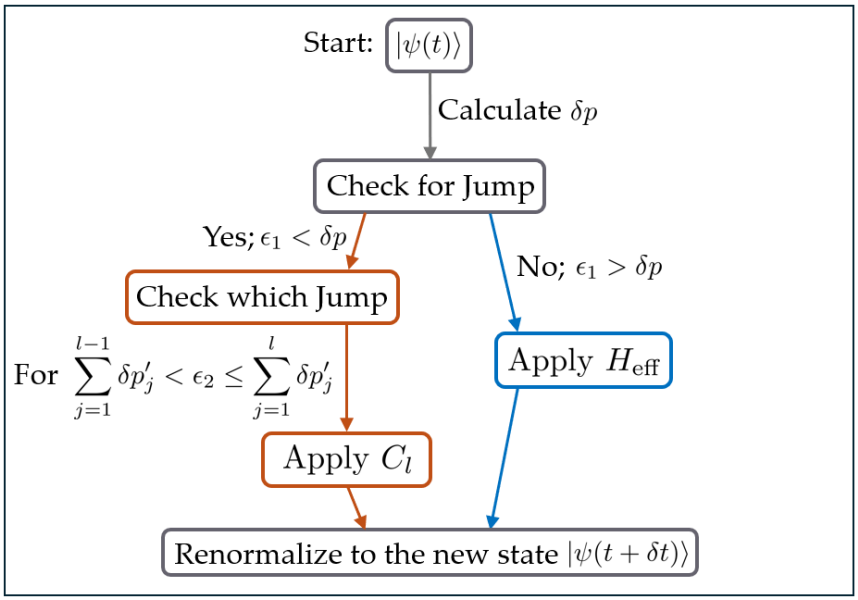

Figure 2.1: Schematic of a single time step in the QT time evolution algorithm.

quantum jump operators, C_j with $j \in [0, 1, ..., N]$, is applied to the system or if evolution under H_{eff} occurs. The probability for quantum jump C_j to occur during the time step from t to $t + \delta t$ is

$$\delta p_j = \delta t \, \langle \psi(t) | C_j^\dagger C_j | \psi(t) \rangle \,, \tag{2.34}$$

then the total probability for a jump to occur is $\delta p = \sum_j \delta p_j$. This is compared against a uniformly distributed random number, $\epsilon_1 \in [0, 1]$. If $\epsilon_1 < \delta p$, then we decide a quantum jump has occurred and must choose which one, continuing the trajectory in (i) and if $\epsilon_1 > \delta p$, then we evolve under H_{eff} in (ii). This step introduces the only requirement for δt in QT theory. The step size, δt, must be small enough such that the chance for one quantum jump in the same time step is small and the chance for two quantum jumps is negligible. These are satisfied when $\delta p \ll 1$, so δt must be chosen such that this is always valid.

(i) If $\epsilon_1 < \delta p$, then the responsible quantum jump must be determined (if there is more than one C_j). To do this, the relative probabilities for each operator (relative to the other C_j) is calculated as

$$\delta p'_j = \frac{\delta p_j}{\delta p}. \tag{2.35}$$

Then, noting that $\sum_j \delta p'_j = 1$, these relative probabilities are used to partition the interval

$[0,1]$ and a second uniformly distributed random number, $\epsilon_2 \in [0,1]$, is used to choose which jump occurs. For this, the cumulative probabilities are used so that if

$$\begin{aligned}
0 &\leq \epsilon_2 \leq \delta p'_1 && \Rightarrow \text{ Operator } C_1 \text{ occurs,} \\
\delta p'_1 &< \epsilon_2 \leq \delta p'_1 + \delta p'_2 && \Rightarrow \text{ Operator } C_2 \text{ occurs,} \\
&&& \vdots \\
\sum_{j=1}^{l-1} \delta p'_j &< \epsilon_2 \leq \sum_{j=1}^{l} \delta p'_j && \Rightarrow \text{ Operator } C_l \text{ occurs,} \\
&&& \vdots \\
\sum_{j=1}^{N-1} \delta p'_j &< \epsilon_2 \leq \sum_{j=1}^{N} \delta p'_j = 1 && \Rightarrow \text{ Operator } C_N \text{ occurs.}
\end{aligned} \tag{2.36}$$

After the responsible quantum jump has been chosen, the corresponding operator (say C_j is responsible) is applied to the ket vector following

$$|\widetilde{\psi}(t+\delta t)\rangle = C_j \, |\psi(t)\rangle \, . \tag{2.37}$$

(ii) If $\epsilon_1 > \delta p$, then no quantum jump occurs, and the ket vector is evolved following

$$H_{\text{eff}} = H_S - \frac{i}{2} \sum_j C_j^\dagger C_j, \tag{2.38}$$

using the Schrödinger equation:

$$i \frac{d}{dt} |\psi(t)\rangle = H_{\text{eff}} |\psi(t)\rangle. \tag{2.39}$$

This evolution can be done numerically using a Runge-Kutta method [186] or other differential equation numerical methods, and has exact solution

$$|\widetilde{\psi}(t+\delta t)\rangle = e^{-iH_{\text{eff}}\delta t} \, |\psi(t)\rangle \, , \tag{2.40}$$

after one time step.

Neither (i) or (ii) are norm conserving, so before moving to the next time step, the ket vector must be renormalized following

$$|\psi(t+\delta t)\rangle = \frac{|\widetilde{\psi}(t+\delta t)\rangle}{\sqrt{\langle \widetilde{\psi}(t+\delta t) | \widetilde{\psi}(t+\delta t)\rangle}}, \tag{2.41}$$

and after this the next time step beginning with $|\psi(t+\delta t)\rangle$ can occur. When the desired end-time is reached, $|\psi(t)\rangle$ is known at each time and can be used to calculate any desired observable for this single trajectory. To find the ensemble average behavior of the observable, these must be averaged across sufficiently many trajectories for convergence to be reached.

2.2.1 Modeling Spontaneous Emission and Rabi Oscillations with QT Theory

To give some concrete examples of simulations with QT theory, we go through two standard quantum optics phenomena. The first is spontaneous emission from an excited two level system (TLS) and the second is Rabi oscillations from a coherently driven TLS with spontaneous emission. The population dynamics of each are presented in Fig. 2.2 for varying numbers of averaged trajectories.

One of the simplest quantum optics systems, spontaneous emission from an excited TLS underlies all quantum optics applications. All systems must emit from some energy transition for a quantum optic system to be detected. The Hamiltonian for this is $H_S = \omega_0 \sigma^+ \sigma^-$ where ω_0 is the transition frequency of the TLS and σ^+ (σ^-) is the Pauli raising (lowering) operator. There is also a single quantum jump operator, $C_1 = \sqrt{\gamma}\sigma^-$, representing spontaneous emission from the TLS to the reservoir, with rate γ. Figure 2.2(a) shows the population evolution of one trajectory for this system. Simply, the TLS remains in the excited state until a jump is determined to occur, then C_1 is applied and the TLS "jumps" into the ground state. Figures 2.2(b) and (c) show the average behavior of the TLS population after averaging 100 and 10000 trajectories respectively. After 100 trajectories, convergence has not occurred, but after 10000 trajectories we clearly recover the expected solution of exponential decay of the population.

Next, we add another element to this system and drive the TLS with a resonant CW laser field. The Hamiltonian in the interaction picture at the laser frequency and with a rotating wave approximation is $H_S = \Omega(\sigma^+ + \sigma^-)/2$, where Ω is the frequency of the Rabi oscillations [106]. We also continue to include spontaneous emission with the C_1 operator (if this is not included, the evolution would not be stochastic and would only be Rabi oscillations). The single QT is shown in Fig. 2.2(d), this shows how the TLS experiences coherent Rabi oscillations between instantaneous quantum jumps (marked by the orange dots). As we average more trajectories in Figs. 2.2(e) and (f), it becomes clear that the quantum jumps create decoherence between the many averaged trajectories. This means the Rabi oscillations in the overall ensemble average are damped until they completely lose

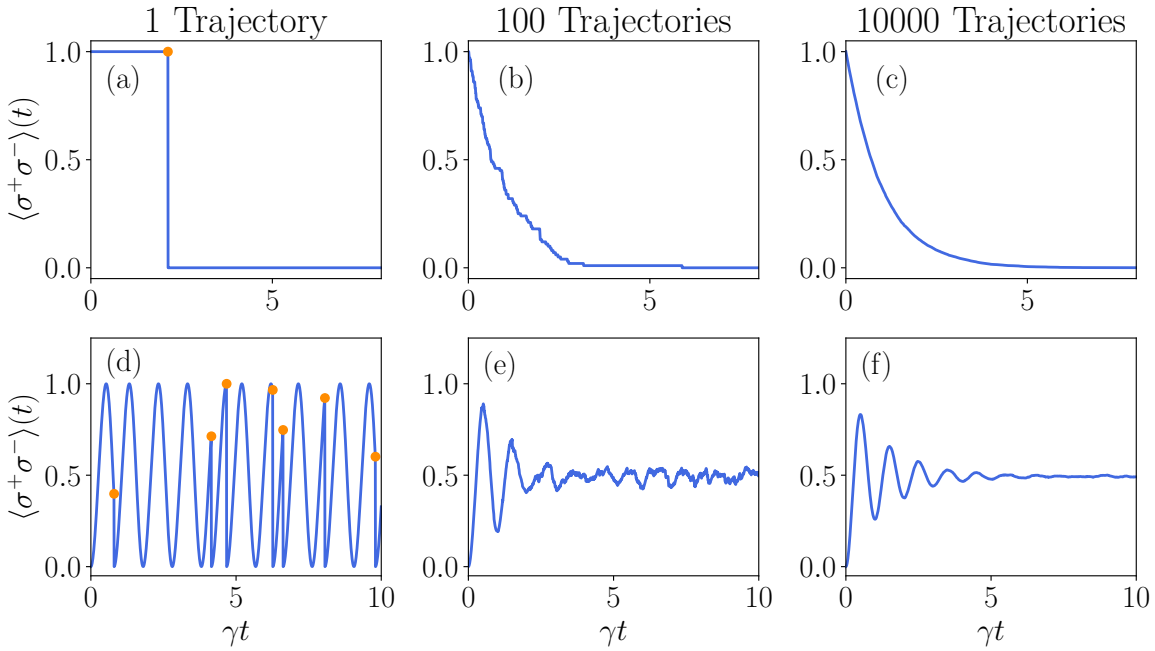

Figure 2.2: Population dynamics for spontaneous emission from an excited TLS for (a) one QT, (b) 100 QTs, and (c) 10000 QTs. Similarly, the dynamics of a coherently driven TLS (initially unexcited) with spontaneous emission for (d) one QT, (e) 100 QTs, and (f) 10000 QTs. The orange dots in (a) and (d) represent times when a radiative quantum jump, with operator $C_1 = \sqrt{\gamma}\sigma^-$, occurred in the trajectory.

coherence and are replaced by the TLS population sitting at 0.5 in the steady state.

2.3 Time-Delayed Coherent Feedback in the Linear Regime

The QTDW model used in this thesis (and matrix product states) are powerful models to investigate coherent feedback effects, but they give little analytical insight to the underlying mathematical physics. This is by design as they are both intended for simulation of these complex systems rather than to derive analytical results. Indeed coherent feedback in the nonlinear regime becomes entirely intractable to derive analytic results for, which is why these models are required. In the linear regime we can get some initial insight to help guide our nonlinear investigations, and aid in our understanding of the simulated coherent

feedback phenomena. In this section, we derive the equations of motion for spontaneous emission with feedback in the linear regime and discuss the nomenclature of Markovian and non-Markovian dynamics used in this thesis and the coherent feedback community as a whole.

The feedback setup we discuss here is a TLS coupled bidirectionally to a waveguide with rate γ. The waveguide terminates in a perfect mirror which returns the TLS field after a characteristic delay time τ and with a round trip phase change $\phi = \omega_0\tau + \phi_{\mathrm{M}}$ where ω_0 is the transition frequency of the TLS. This is the same setup as later chapters, but without a laser drive or any additional dissipation aside from waveguide coupling, see for example Fig. 3.1. The combined system and reservoir Hamiltonian is

$$H = \omega_0\sigma^+\sigma^- + \int \omega b^\dagger(\omega)b(\omega)d\omega + \int G(\omega)(\sigma^+ b(\omega) + b^\dagger(\omega)\ \sigma^-)d\omega, \tag{2.42}$$

where $b^\dagger(\omega)$ ($b(\omega)$) is the raising (lowering) operator of the waveguide field. The third term in the Hamiltonian represents the interaction between the TLS and waveguide. The presence of the feedback loop alters the density of states of the waveguide field so the coupling term $G(\omega)$ picks up a frequency dependence (rather than a constant value typically used for an open waveguide). This term is

$$G(\omega) = \sqrt{\frac{\gamma}{\pi}} \sin\left(\frac{\omega\tau + \phi_M}{2}\right). \tag{2.43}$$

Note that this is different from the coupling form used in later chapters because of a difference in where we choose to measure the phase from. One can think of the TLS as coupling to a unidirectional waveguide at two points with a delay time of τ between them. Then the phase difference in the waveguide field between these two points is $\omega\tau + \phi_{\mathrm{M}}$. The above coupling form is derived if the phase is measured from the midpoint between the two coupling locations, while the later chapters treat the phase as 0 at the first coupling point and put the full phase change in the second coupling point. There is no mathematical difference between the two approaches, it is a free choice of the system where the phase is measured relative to. However, for the respective models it is advantageous to take these two different forms.

The ket vector describing the complete system and reservoir in the *linear* regime is

$$|\psi(t)\rangle = \beta(t)\,|e, \{0\}\rangle + \alpha_\omega^{(1)}(t)\,|g, \{1\}_\omega\rangle\,, \tag{2.44}$$

where $\beta(t)$ is the coefficient for the state with an excited TLS and empty waveguide and $\alpha_\omega^{(1)}(t)$ is the coefficient for the state with the TLS in the ground state and one photon

in the waveguide with frequency ω. For spontaneous emission, this has initial condition $|\psi(0)\rangle = |e, \{0\}\rangle$. This describes a complete system, so the time evolution of $|\psi(t)\rangle$ follows the Schrödinger equation and we can derive the coupled differential equations:

$$\frac{d\beta}{dt} = -i\omega_0\beta(t) - i\int G(\omega)\alpha_\omega^{(1)}(t)d\omega, \tag{2.45}$$

$$\frac{d\alpha_\omega^{(1)}}{dt} = -i\omega\alpha_\omega^{(1)}(t) - iG(\omega)\beta(t). \tag{2.46}$$

We now want to remove the reservoir dependence and reduce the dynamics to the TLS behavior. Equation (2.46) has the solution

$$\alpha_\omega^{(1)}(t) = -iG(\omega)\int_0^t e^{i\omega(t'-t)}\beta(t')dt', \tag{2.47}$$

which can be directly substituted into Eq. (2.45) to get the delay differential equation (after some algebra similar to that done in [185])

$$\frac{d\beta}{dt} = -i\omega_0\beta(t) - \frac{\gamma}{2}\beta(t) + \frac{\gamma}{2}e^{i\phi_M}\beta(t-\tau)\theta(t-\tau). \tag{2.48}$$

This is exactly the equation of motion for spontaneous emission, but with an additional feedback term that kicks in after $t = \tau$, namely the earliest time the field can return from the feedback loop.

2.3.1 Markovian versus Non-Markovian Dynamics

Equation (2.48) highlights what is meant by non-Markovian dynamics when discussing coherent feedback. Clearly, the evolution of $\beta(t)$ is non-Markovian when $t > \tau$, because it explicitly uses the value $\beta(t-\tau)$, the value of β in the past. But the original Hamiltonian itself does not inherently create non-Markovian dynamics, it is only in the removal of the reservoir that the non-Markovian nature appears in the mathematics. This is an important point for coherent feedback systems. Non-Markovian systems can be made Markovian by expanding the system of interest, which is the approach of the QTDW model and matrix product states. These include the feedback section of the waveguide in the (mathematical) "system" rather than the reservoir, allowing the mathematics to remain Markovian. Then even though the model is Markovian, we still describe the dynamics as non-Markovian because we take it from the perspective of the coupled quantum optical system (whatever that may be, though in this thesis it is a TLS).

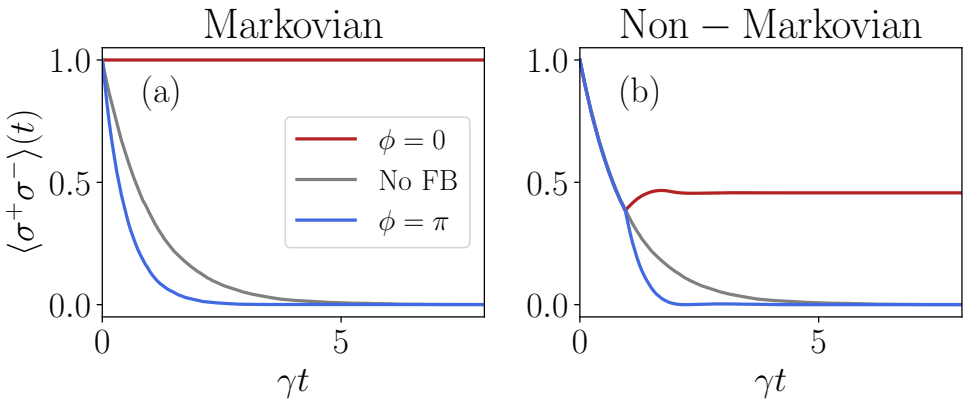

Figure 2.3: Spontaneous emission population dynamics with (a) Markovian coherent feedback and (b) non-Markovian coherent feedback, for two different round trip phase changes. In gray, spontaneous emission to an open waveguide is shown.

Now, we can make a Markovian approximation to Eq. (2.48) to get further insight to the effects of coherent feedback. To do this, the dependence on $\beta(t-\tau)$ must be removed. For a short feedback loop, we can make the approximation $\beta(t-\tau) = e^{i\omega_0 \tau}\beta(t)$, reducing the travel around the feedback loop to an instantaneous phase shift. With this approximation, the dynamics truly are Markovian and the evolution is

$$\frac{d\beta}{dt} = \left[-i\omega_0 - \frac{\gamma}{2}\left(1 - e^{i\phi}\right)\right]\beta(t) = X\beta(t), \tag{2.49}$$

with solution $\beta(t) = e^{Xt}$. The population dynamics are $\langle \sigma^+\sigma^- \rangle (t) = |\beta(t)|^2$ and we can use the solution for $\beta(t)$ to get

$$\langle \sigma^+\sigma^- \rangle (t) = e^{-\gamma(1-\cos\phi)t}, \tag{2.50}$$

giving a feedback modified spontaneous emission rate of $\widetilde{\gamma} = \gamma(1-\cos\phi)$. This is our first result of how feedback significantly alters the behavior of the coupled quantum system. Depending on the choice of round trip phase change, the spontaneous emission rate can be doubled ($\phi = \pi$) or it can be suppressed completely ($\phi = 0$).

In Fig. 2.3 we show the population dynamics with the Markovian approximation in (a) and the full non-Markovian dynamics in (b) (in both we also show spontaneous emission to an open waveguide in gray). The primary difference is simply a delay before the modified spontaneous emission rate occurs. Also, for the enhanced emission (blue line), the non-Markovian exponential decay after $t = \tau$ is $> 2\gamma$ ($\approx 3\gamma$). These may seem like small

changes, but as we will show later in the thesis, not accounting for this delay misses much of the rich physics that is introduced by coherent feedback. The physical explanation for this dependence on ϕ in $\widetilde{\gamma}$ is that the returning feedback field is destructively (when $\phi = 0$) or constructively (when $\phi = \pi$) interfering with the outgoing TLS emission. This interpretation of interference between the outgoing field and returning feedback will underlie all of the more complex results in the non-Markovian and nonlinear regimes.

Another Markovian insight that can be derived in the linear regime is a feedback induced shift to the TLS transition frequency. Rather than deriving the equations of motion for $|\phi(t)\rangle$, one can instead use the Heisenberg equations of motion to calculate $\langle\sigma^-\rangle$ as done by Koshino et al [35]. Making a Markov approximation, the feedback induced shift is derived to be

$$\widetilde{\omega}_0 - \omega_0 = \frac{\gamma}{2}\sin\theta. \tag{2.51}$$

This has been shown to work well for very short feedback loops [37], but as we will show later in Ch. 4, this breaks down for long loops when non-Markovian effects are, of course, also important in the linear regime.

A common shorthand for the Markovian regime in coherent feedback is to write $\tau \to 0$ and act as if the system is directly in front of the mirror. This is a slight oversimplification (although generally works). Instead, what the Markovian regime represents is when the dynamics can be represented purely by an instantaneous phase change picked up after the round trip (neglecting the delay in the dynamics). This is a subtle difference, but if there are multiple coupled systems, means that each system can be affected by a different round trip phase change.

2.4 Computational Methods

For the numerical simulations of the QTDW model in this thesis, we use `Python` and its standard packages for the in-house code purpose built for the coherent feedback simulations. We chose `Python` for the implementation because of the computational community already present in the `Python` ecosystem. `QuTiP` [187], an open-source quantum optics package in `Python`, is already well used within the community, and other mathematical packages are actively developed and improved to make the solvers faster and more efficient. The `scipy` package is well used throughout our code for its extensive functions focusing on efficient memory allocation for sparse matrix operations. This made `Python` the natural choice over languages such as `Matlab`, `C/C++`, and `Fortran` which have more difficult implementations and a less active community. Also, in the open-source spirit of the `Python` community,

we hope to release the codes used in this thesis as part of a numerical paper after the conclusion of this thesis. The following chapter contains the mathematical derivation of the QTDW model, so we only discuss the points relevant to the simulation here.

The feedback section of the waveguide is treated as a collisional model [49, 173, 188]. This means the field is treated in the discrete time domain as small slices of the waveguide field which can contain up to one photon (see Fig. 3.1(b) for a schematic). The full Hilbert space for the loop discretized into N bins is the Kronecker product of N two level systems, which has size $N!$. For a loop with a non-negligible delay (i.e. one that creates non-Markovian dynamics) we typically need $N \approx 50$ to resolve the time dynamics and this would be a full Hilbert space of dimension $\approx 3 \times 10^{64}$, which is impossible to implement in any simulation. Instead we can truncate the total number of photons in the loop to two, and this reduces the size of the Hilbert space to

$$d_{\mathrm{FB}} = \binom{N}{0} + \binom{N}{1} + \binom{N}{2} = 1 + N + \frac{N(N-1)}{2}, \tag{2.52}$$

which is tractable for a high performance workstation up to about $N = 100$ (depending on the performance specs of the workstation).

To include the feedback loop as part of the system Hamiltonian, we can take the Kronecker product of the two spaces, $\mathcal{H}_{\mathrm{TLS}} \otimes \mathcal{H}_{\mathrm{FB}}$, with total dimension $d = 2 \times d_{\mathrm{FB}}$. To build operators that act on the TLS, we take the Kronecker product of the relevant Pauli operator with an identity operator of dimension d. To build operators that act on any of the bins in the feedback loop is not so straight forward due to the photon number truncation (without this we could just take the product of one Pauli operator with $N-1$ two-dimensional identity operators). Instead we manually build the loop operators by finding the matrix coefficients which act on the relevant ket state entries, and then taking the product of this manually built matrix with the two dimensional identity operator.

To give an example of building a loop operator matrix, the ket vector for the loop is

$$|\psi_{\mathrm{W}}\rangle = c^{(0)} |\{0\}\rangle + \sum_{j=1}^{N} c_j^{(1)} |1_j\rangle + \sum_{j=1}^{N-1} \sum_{k=j+1}^{N} c_{j,k}^{(2)} |1_j\rangle |1_k\rangle , \tag{2.53}$$

where $|\{0\}\rangle$ represents an empty loop, $|1_j\rangle$ represents a single photon in the loop in bin j, and $|1_j\rangle |1_k\rangle$ represents two photons in the loop in bins j and k (note the limits of the double sum are set to avoid double counting and $j \neq k$ because there is a maximum of one photon in a single bin). The numerical representation of this ket vector is a column array that begins with $c^{(0)}$, followed by each $c_j^{(1)}$ in ascending order of j, and then followed by

$c^{(2)}_{j,k}$ where we write all coefficients for $j = 1$ and $k \in [j+1, N]$, followed by all coefficients for $j = 2$, etc. Then to find the photon population in the m'th bin, $\langle B^\dagger_m B_m \rangle$, we put a value of 1 along the diagonal in the $m+1$'th entry (with the $+1$ because we must account for the 0 photons in the loop entry). We also put a value of 1 along the diagonal for all coefficients $c^{(2)}_{j,k}$ where j or $k = m$.

We make a few additional comments on the computational implementation of the model. These matrices are extremely large, but primarily contain entries which are 0. Thus, we make extensive use of the functions in the `scipy.sparse` package which is an efficient linear algebra package using sparse matrix techniques. This is essential to speed up the numerical performance of the QTDW model and avoid extraneous calculations and memory use. The between jump evolution over a time step of length Δt follows the propagator $\exp[-iH_{\text{eff}}\Delta t]$, which we numerically calculate using the `scipy.sparse.linalg.expm` function. As discussed in the previous section on QT theory, the QTDW model is completely parallelizable due to the independence of each trajectory from all other trajectories. To take advantage of this we use the `mpi4py` package to do a simple parallelization of the code that runs all trajectories and calculates the relevant observables in parallel before taking the final average over all trajectories on a single node.

When we initially started work on the QTDW model, other quantum optics numerical packages did not have the ability to build ket vectors with a truncated Hilbert space, so could not be used. Since our publications with the QTDW model, `QuTiP` [187] has updated their library to build truncated Hilbert spaces for use in collisional waveguide models. Also, very recently (April 2025), a new package called `WaveguideQED.jl` [189] was published focusing entirely on simulating collisional models in waveguide-QED using `Julia`. These packages can both now be used to simulate non-Markovian coherent feedback population dynamics, but have not implemented the efficient calculation of quantum correlation functions in their packages. This is a requirement for the output spectrum and photon statistics calculations presented in this thesis.

Chapter 3

Quantum trajectory theory and simulations of nonlinear spectra and multi-photon effects in waveguide-QED systems with a time-delayed coherent feedback

This work is published as: G. Crowder, L. Ramunno, and S. Hughes, "Quantum trajectory theory and simulations of nonlinear spectra and multiphoton effects in waveguide-QED systems with a time-delayed coherent feedback", Phys. Rev. A **106**, 013714 (2022) [190] and is reproduced here verbatim, in a consistent style for the thesis. After our initial implementation of the quantum trajectory discretized waveguide (QTDW) model in [46] for the simulation of population dynamics, this paper significantly expanded on the model to calculate multitime quantum correlation functions. We use this to investigate how coherent feedback can affect the output spectra and photon statistics. For a short loop, by varying the round trip phase change, we show how the output photons can be switched between bunching and antibunching. We also show that the central peak of the Mollow triplet can be broadened or completely suppressed. For longer loop lengths, we show how new resonances appear in the output spectrum, a consequence of the Mollow triplet being dressed by the Fabry-Pérot resonances set up by the feedback loop. All of the calculations, simulations and writing was done by myself. Feedback and editing were provided by Lora Ramunno and Stephen Hughes and all authors revised the work following comments made by reviewers in the submission process. Note that there is a typo in the manuscript in

Eq. (3.25), the lower limit of the integral should be $-\infty$.

Abstract

We study the nonlinear spectra and multi-photon correlation functions for the waveguide output of a two-level system (including realistic dissipation channels) with a time-delayed coherent feedback. We compute these observables by extending a recent quantum trajectory discretized-waveguide (QTDW) approach which exploits quantum trajectory simulations and a collisional model for the waveguide to tractably simulate the dynamics. Following a description of the general technique, we show how to calculate the first and second order quantum correlation functions, in the presence of a coherent pumping field. With a short delay time, we show how feedback can be used to filter out the central peak of the Mollow triplet or switch the output between bunched and anti-bunched photons by proper choice of round trip phase. We further show how the loop length and round trip phase affects the zero-time second order quantum correlation function, an indicator of bunching or anti-bunching. New resonances introduced through the feedback loop are also shown through their appearance in the incoherent output spectrum from the waveguide. We explain these results in the context of the waiting time distributions of the system output and individual trajectories, uniquely stochastic observables that are easily accessible with the QTDW model.

3.1 Introduction

Feedback has been well used as a stabilizing and control mechanism both in photonics and other areas of cutting-edge technology [36, 39, 43, 146–148, 152, 161, 167, 191–193]. Most commonly, measurement-based feedback has been employed where the output of the system is used to act back on the system to achieve better stability, state generation and error suppression [152, 192–198]. This type of feedback control is common practice in laser design and has also been shown to improve quantum systems as well [146, 170]. However, for use in many quantum technology applications, it is important to preserve the system *coherence*. Thus, a time-delayed coherent feedback has been studied as an avenue of increasing the coherent lifetime in such systems. In contrast to measurement-based

feedback, coherent feedback is integrated at the system level and no measurements are taken to avoid introducing further decoherence in the system [35–43, 45–47, 161, 167–170, 173, 185, 191, 199–204].

The regime of waveguide quantum electrodynamics (QED), where quantum systems are coupled together via waveguide modes, is especially sensitive to loss of coherence [50, 52, 53, 57, 58, 60, 205–218]. These systems have many applications in quantum information technology, where they can act as sources for single photons or pairs of photons, photon frequency converters, and single photon detectors which can be further integrated into circuit QED architectures [219]. Previous work has shown that including coherent feedback in waveguide-QED systems can significantly improve the coherent lifetime of the system or enhance the system emission beyond the typical spontaneous emission rate [36, 37, 42, 43, 45, 201] as well as enable the generation of shaped single photon sources [202]. Not only has it been shown to improve these systems, but also to introduce new system behavior beyond well-known waveguide-QED results, such as new resonances produced by the waveguide modes set up by the feedback [38, 185].

By including a time-delayed coherent feedback in the waveguide-QED system, a non-Markovian dynamic is introduced in the evolution which adds an additional complexity to the simulation of such systems. Typical models (e.g., Lindblad master equations) make the Markovian approximation, that the evolution of the system only depends on the state of the system at the present, which is no longer valid when feedback is included. Instead, a "collisional model" of the waveguide can be used where the waveguide is accounted for at the Hamiltonian level as a series of interactions with a localized coupled quantum system [49, 173, 188, 203, 220]. By expanding the Hamiltonian in this way, Markovian numerical solutions are again possible which are less restricting than the specialized non-Markovian mathematical solutions which have also been used [36, 185]. Note that we refer to the unique dynamics that arise from the introduction of the feedback using the common nomenclature of non-Markovian, since the round trip memory effects are still included in this model.

When the waveguide is included in the Hamiltonian, the Hilbert space can quickly become very large and so specialized methods are used to model its evolution. When limited to the linear regime, results can be computed analytically but this significantly restricts the phenomena that can be investigated [36, 167, 221, 222]. A popular method for modelling coherent feedback is matrix product states (MPSs) [38, 44, 46, 171, 201, 218, 223, 224], a powerful technique where tensor networks are used to limit the entanglement within the Hilbert space. Quantum trajectory (QT) theory is a less popular technique which has also recently been used to investigate the effects of a time-delayed coherent feedback [46, 173, 185]. This technique uses stochastic individual realizations of the system to obtain

the ensemble average behavior of the system [176–178, 225, 226]. The advantage of this technique is that it can give unique insights into the underlying stochastic phenomena of the system behavior and numerically, it scales linearly with the Hilbert space and is completely parallelizable.

Previous QT approaches have been limited to the observables of the coupled quantum system rather than the waveguide output, important for experimental investigations of feedback. In this paper, we extend a previous QT discretized waveguide (QTDW) model to investigate the quantum correlation functions and waiting time distribution function, a uniquely accessible observable from QT theory, of the waveguide output. These observables give intuitive and powerful insight into the multi-quanta effects present when a time-delayed coherent feedback is introduced to the system. Additionally, they are also readily available to experimental realizations of these systems, and thus give fresh insight into the experimental observables.

The rest of our paper is organized as follows: In Sec. 3.2.1, we present the waveguide-QED model of interest and introduce the QT formalism used in our approach which accounts for the full non-Markovian dynamics introduced by the feedback loop. Subsequently, in Sec. 3.2.2, we define the waveguide population parameters of interest and in Sec. 3.2.3, we explain how to compute the first and second order quantum auto-correlation functions in the QT picture. In Sec. 3.3, we show our results, including how a time-delayed feedback can act to increase the coherence of the system output and introduce multi-quanta resonances. We also show how these results are affected by the inclusion of Markovian output channels such as pure dephasing, which is important for modelling realistic qubits. These results are explained through examples of individual trajectories and the waiting time distribution of the waveguide output, an experimentally accessible observable. Lastly, in Sec. 3.5 we conclude.

3.2 Theory

3.2.1 Model and Hamiltonian

We investigate a typical setup for including feedback in a waveguide-QED system, which includes a two level system (TLS), such as a single atom or quantum dot (QD) or flux qubit, coupled to a truncated waveguide depicted in Fig. 3.1(a). The TLS has ground (excited) state represented by $|g\rangle$ ($|e\rangle$) and couples bidirectionally to the waveguide with total radiative decay rate γ [38, 46].

The TLS is driven with a continuous wave (CW) laser of Rabi frequency Ω and the detuning between the laser and TLS is $\delta = \omega_0 - \omega_{\mathrm{L}}$, where ω_{L} is the frequency of the laser and ω_0 is the frequency of the TLS. The location of the TLS is chosen as a reference to be $x = 0$, and the waveguide is truncated with a mirror (which we assume is lossless and introduces a phase change of ϕ_{M}) at $x = -L_0/2$. Then the round trip length of the feedback loop is L_0 which introduces a delay time of $\tau = L_0/c(\omega_0)$, where $c(\omega_0)$ is the group velocity of the waveguide mode of reference frequency ω_0 in the waveguide.

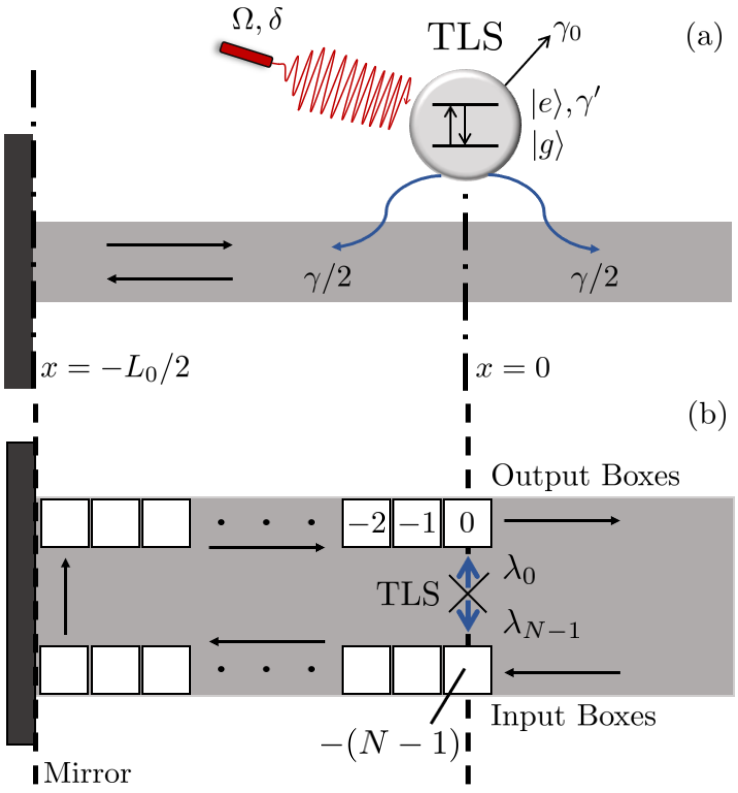

Figure 3.1: (a) Model of the waveguide-QED system of interest, which includes a TLS with ground state $|g\rangle$ and excited state $|e\rangle$ embedded in a terminated waveguide of length L_0. The TLS couples symmetrically to the waveguide with a total decay rate of γ. The TLS is driven by a CW laser of strength Ω and detuning $\delta = \omega_0 - \omega_L$. The TLS also undergoes off-chip decay with rate γ_0 and pure dephasing with rate γ'. (b) Representation in the QTDW picture where the modes of the waveguide have been discretized into spatial bins. There are N bins created by the discretization and bin n spans a spatial length from $-n\Delta t$ to $-(n+1)\Delta t$ relative to the output bin. In the QTDW model, the TLS couples to bins $N-1$ and 0 with coupling constants λ_{N-1} and λ_0 respectively.

The main Hamiltonian for this system, $H = H_0 + H_{\text{pump}} + H_{\text{W}} + H_{\text{I}}$, includes four important components: the non-interacting Hamiltonian for the TLS, H_0, the Hamiltonian of the CW-laser drive, H_{pump}, the non-interacting Hamiltonian for the waveguide, H_{W}, and the interaction Hamiltonian, H_{I}, between the TLS and waveguide.

In the interaction picture of the laser drive frequency, ω_{L}, the Hamiltonian of the TLS and the pump is

$$H_0 + H_{\text{pump}} = \delta\sigma^+\sigma^- + \frac{\Omega}{2}(\sigma^+ + \sigma^-), \tag{3.1}$$

where σ^+ (σ^-) is the Pauli raising (lowering) operator, and we have applied a rotating wave approximation. We have also adopted natural units with $\hbar = 1$. Next, in the (continuous) frequency domain, the waveguide Hamiltonian is

$$H_{\text{W}} = \int_{-\infty}^{\infty} d\omega\, (\omega - \omega_{\text{L}})\, b^\dagger(\omega) b(\omega), \tag{3.2}$$

where we choose $b^\dagger(\omega)$ ($b(\omega)$) to be the raising (lowering) operator for the propagating photon modes in the waveguide. These field operators have the usual commutator $[b(\omega), b^\dagger(\omega')] = \delta(\omega - \omega')$.

Finally, the influence of the feedback loop is seen in the interaction Hamiltonian through a modification of the typical coupling rates:

$$\begin{aligned} H_{\text{I}} = \int_{-\infty}^{\infty} d\omega \Bigg[\Bigg(& \sqrt{\frac{\gamma}{4\pi}}\sigma^+ b(\omega) \\ & + \sqrt{\frac{\gamma}{4\pi}} e^{i(\phi_M + \omega\tau)} \sigma^+ b(\omega) \Bigg) + \text{H.c.} \Bigg], \end{aligned} \tag{3.3}$$

where the coupling to the right propagating mode picks up the round trip phase change. The form of this interaction is derived in Appendix 3.7.

A full derivation of the QTDW model is given in Ref. [46], including the component Hamiltonians in the discrete frequency picture, thus we only highlight the important points of the model below. In that paper the formalism is also derived to allow for an open waveguide where the left and right moving fields are treated independently, important for systems such as two QDs spatially separated in the waveguide where chiral coupling can also play a significant role in the system behavior [71–73, 76–78, 218, 227–232]. To represent the waveguide with a collisional model, we transform Eq. (3.2) to the discrete time domain with operators B_n, using a discrete Fourier transform on the waveguide mode

operators in the discrete frequency picture ($b(\omega) = \sqrt{L_0/2\pi}b_k$). This gives the explicit relationship

$$\begin{aligned} B_n &= \frac{1}{\sqrt{N}} \sum_{k=0}^{N-1} b_k e^{i(\omega_k - \omega_0)n\Delta t}, \\ b_k &= \frac{1}{\sqrt{N}} \sum_{n=0}^{N-1} B_n e^{-i(\omega_k - \omega_0)n\Delta t}, \end{aligned} \tag{3.4}$$

where N is the total number of discrete bins used to model the waveguide, Δt is the corresponding time discretization, and $\omega_k = 2\pi k/L_0$, which assumes linear dispersion for the waveguide mode. In this domain, the delay time from the round trip can be expressed as $\tau = N\Delta t$. Note, the commutator for the time domain operators is $[B_n, B_{n'}^\dagger] = \delta_{n,n'}$, and B and $B^\dagger$ have dimensionless units. We make the approximation that N is chosen sufficiently large (equivalently Δt sufficiently small) that the probability to have more than one photon in any individual bin is negligible, which is valid when $\Delta t \ll 1/\gamma$. Formally, B_n represents the slice of the waveguide field that interacts with the TLS over a certain time interval, $[n\Delta t, (n+1)\Delta t)$. We can equivalently represent these B_n as a spatial section of the waveguide through the intrinsic relationship between the space and time domains related by the group velocity.

By transforming into this discrete spatial bin model, the waveguide is effectively a sequence of bins which pass the feedback (and output) field forward one bin each time step. Mathematically, this is seen through the evolution of the time domain operator, B_n, under the waveguide Hamiltonian:

$$U_{\mathrm{W}}^\dagger(\Delta t) B_n U_{\mathrm{W}}(\Delta t) = e^{-i\delta\Delta t} B_{n-1}, \tag{3.5}$$

where $U_{\mathrm{W}}(\Delta t) = e^{-iH_{\mathrm{W}}\Delta t}$. The derivation for this relation is presented in Appendix 3.8. Note that only the two spatial bins located at the position of the TLS interact with the TLS at a single time. This is shown schematically in Fig. 3.1(b).

The TLS and pump Hamiltonians, $H_0 + H_{\mathrm{pump}}$, are unmodified by our transformation into the discrete time domain. The interaction Hamiltonian becomes

$$H_{\mathrm{I}} = \left(\sqrt{\frac{\gamma}{2\Delta t}} \sigma^+ B_{N-1} + e^{i\phi} \sqrt{\frac{\gamma}{2\Delta t}} \sigma^+ B_0 \right) + \mathrm{H.c.}, \tag{3.6}$$

where $\phi = \phi_{\mathrm{M}} + \omega_0 \tau$ is the round trip phase change. The TLS first interacts with the $(N-1)^{\mathrm{th}}$ bin which then passes the field from bin to bin around the loop and returns to the TLS after N time steps to interact with the TLS again in bin 0. Thus, the TLS couples to bins $N-1$ and 0 with coupling constants $\lambda_{N-1} = \sqrt{\gamma/2\Delta t}$ and $\lambda_0 = e^{i\phi}\sqrt{\gamma/2\Delta t}$. The

form of this interaction Hamiltonian was fully derived in Sec. IV A (b) of Ref. [46] for reference.

The ket vector, in factorized form, for the complete TLS and waveguide system is

$$|\psi(t)\rangle = |\psi_{\rm S}(t)\rangle\,|\psi_{\rm W}(t)\rangle\,, \tag{3.7}$$

where $|\psi_{\rm S}(t)\rangle$ is the ket vector for the TLS and $|\psi_{\rm W}(t)\rangle$ is the ket vector for the waveguide from $x = 0$ to $x = -L_0/2$, which we limit to a maximum of two photons in this section of the waveguide.[1] We justify this approximation later in our results where we report the population for two photons in the feedback loop.

The waveguide field in the $x > 0$ region is modeled through simulated measurements of the output field in the 0'th bin. The ket vector can be split as

$$|\psi(t)\rangle = |\psi_0(t)\rangle\,|0_0\rangle + |\psi_1(t)\rangle\,|1_0\rangle\,, \tag{3.8}$$

where $|0_0\rangle$ is an empty bin 0 and $|1_0\rangle$ represents a photon in bin 0. Before moving the final bin forward and out of the waveguide section of interest, its information is retrieved by projecting the full ket vector into one of the two states $|\psi_0(t)\rangle$ or $|\psi_1(t)\rangle$ with respective probabilities $\langle\psi_i(t)|\psi_i(t)\rangle$. This process is not norm conserving so renormalization must occur each time step.

Two dissipation channels are also included in our model as quantum jump operators: off-chip decay from the TLS, $C_0 = \sqrt{\gamma_0}\sigma^-$, with rate γ_0 and pure dephasing in the TLS, $C_1 = \sqrt{\gamma'}\sigma^+\sigma^-$, with rate γ'. Following standard QT theory, these are included in the system evolution through stochastic application of the jump operator with probabilities $\langle C_0^\dagger C_0\rangle$ and $\langle C_1^\dagger C_1\rangle$ for off-chip decay and pure dephasing respectively. The Hamiltonian is also modified to a non-Hermitian effective Hamiltonian

$$H_{\rm eff} = H_0 + H_{\rm pump} + H_{\rm I} - \frac{i}{2}\sum_{j=0}^{1} C_j^\dagger C_j, \tag{3.9}$$

which is used to evolve the combined TLS and waveguide ket vector whenever no quantum jump occurs. The inclusion of the final term (which is non-Hermitian) moves the model beyond that of the semi-classical weak excitation approximation approaches. Both quantum jumps are Lindblad channels which have the superoperator form

$$\mathcal{L}(\rho) = -\frac{1}{2}\sum_{j=0}^{1}\left(C_j^\dagger C_j\rho + \rho C_j^\dagger C_j\right) + \sum_{j=0}^{1} C_j\rho C_j^\dagger, \tag{3.10}$$

[1] These ket vectors are $|\psi_{\rm S}(t)\rangle = a(t)\,|g\rangle + b(t)\,|e\rangle$ and $|\psi_{\rm W}(t)\rangle = c^{(0)}(t)\,|\{0\}\rangle + \sum_{j=1}^{N} c_j^{(1)}(t)\,|1_j\rangle + \sum_{j=1}^{N-1}\sum_{k=j+1}^{N} c_{j,k}^{(2)}(t)\,|1_j\rangle\,|1_k\rangle$, which can be multiplied together to get the form in Eq. (3.13).

where ρ is the density matrix for the TLS. These dissipation channels could be dealt with through additional collisional interactions, however, this is not necessary as we take them to be Markovian, and doing so would add to the size of the Hilbert space and increase the computational complexity of the problem.

A single time step for a simulation with this model follows a four step process:

1. Evolve $|\psi(t)\rangle$ using a regular QT step under the effective Hamiltonian, H_{eff}, with the two quantum jump operators C_0 and C_1.

2. Take a *simulated measurement* on the final bin of the waveguide by calculating the population of the bin, N_{B_0} (defined in Eq. (3.11)), and comparing it to a uniformly distributed random number, $x \in (0, 1)$. The ket vector is then projected according to whether a photon is detected or not.

3. Evolve the waveguide bins under H_{W} which acts to step each bin forward one space. Note that the final bin is emptied and contains no information so it can be dropped while the incoming bin is empty for this setup, although this is not a strict limitation in the model.

4. Renormalize the complete system ket vector since the operation of measuring and moving the bins along does not conserve the norm.

3.2.2 Waveguide Population Observables in the QTDW Approach

To investigate the photon population dynamics in the waveguide, we begin with the probability of finding a photon in a single waveguide bin j within the feedback loop,

$$N_{B_j}(t) = \langle\psi(t)|B_j^\dagger B_j|\psi(t)\rangle\,, \tag{3.11}$$

where bin j is travelling towards the mirror if $j \geq N/2$, or travelling away from the mirror if $j < N/2$. As the spatial length of the bins depends on Δt, then so does N_{B_j} so that the total population around the whole loop does not. Thus, a more useful quantity to use is the flux through a particular bin,

$$n_{B_j}(t) = N_{B_j}(t)/\Delta t, \tag{3.12}$$

which is in units of 1/s. The flux of the outgoing bin (at $j = 0$) then gives an observable for the photon flux leaving the system, independent of our choice of Δt, which will prove very useful.

Another useful quantum observable is the photon number distribution function in the feedback loop, namely the probability to have zero, one, or two photons in the feedback loop. With this metric, we can evaluate the applicability of our "two-photons-in-the-loop" approximation. Since the QTDW model directly evolves the ket vector for the system (Eq. (3.7)), this becomes a straight-forward quantity to compute if desired. However, with other techniques such as MPS, these quantities have been calculated via the correlation functions, which can be computationally demanding and does not scale well with the total simulation run time [44, 233].

Explicitly, the ket vector is

$$\begin{aligned}|\psi(t)\rangle = &\left[\alpha^{(0)}(t)\,|g\rangle + \beta^{(0)}(t)\,|e\rangle\right]|\{0\}\rangle \\ &+ \sum_{j=1}^{N}\left[\alpha_j^{(1)}(t)\,|g\rangle + \beta_j^{(1)}(t)\,|e\rangle\right]|1_j\rangle \\ &+ \sum_{j=1}^{N-1}\sum_{k=j+1}^{N}\left[\alpha_{j,k}^{(2)}(t)\,|g\rangle + \beta_{j,k}^{(2)}(t)\,|e\rangle\right]|1_j\rangle\,|1_k\rangle\,,\end{aligned} \tag{3.13}$$

and thus the probabilities can be read off almost immediately as

$$p(0,t) = |\alpha^{(0)}(t)|^2 + |\beta^{(0)}(t)|^2, \tag{3.14a}$$

$$p(1,t) = \sum_{j=1}^{N} |\alpha_j^{(1)}(t)|^2 + |\beta_j^{(1)}(t)|^2, \tag{3.14b}$$

$$p(2,t) = \sum_{j=1}^{N-1}\sum_{k=j+1}^{N} |\alpha_{j,k}^{(2)}(t)|^2 + |\beta_{j,k}^{(2)}(t)|^2, \tag{3.14c}$$

where $p(n,t)$ represents the probability of having n photons in the loop at time t.

Lastly, an important experimental observable is the waiting time distribution (WTD) [159], $W(t')$, for photons detected via the waveguide. This is defined as the distribution of delay times, t', between detection events via the waveguide output channel,

$$W(t') = \frac{N\left(\{A\}|t(A_j) - t(A_{j-1}) = t'\right)}{N_{\text{tot}}}, \tag{3.15}$$

where N_{tot} is the total number of photons detected via the waveguide and $\sum_j N\left(\{A\}|t(A_j) - t(A_{j-1}) = t'\right)$ is the number of detections in the detection record $\{A\}$ with delay time t', between the A_j'th event and the previous event, A_{j-1}. Since simulating

these detection events are a direct part of the QTDW approach to modelling the response, we can record a jump record for each trajectory and then easily calculate the waiting times for each trajectory. This is uniquely accessible by using a QT based approach as the WTD requires individual realizations of the system rather than the ensemble average. This observable can be very useful in explaining the phenomena seen in the ensemble average response as we will show in Sec. 3.3.

3.2.3 Output Quantum Correlation Functions

In previous work with QT based approaches to modelling feedback [46, 185], the results were restricted to how the feedback affected the population of the TLS. Although many useful insights can be gained from this population dynamic, in this paper we focus our observables around the output photons leaving through the waveguide, which is more practical and experimentally relevant. Below, we also show how to calculate the first- and second-order quantum auto-correlation functions for waveguide output photons where we use the first order correlation function to calculate the incoherent spectra. This is usually an extremely difficult theoretical problem for the usual master equation approach because the quantum regression theorem cannot be used for a non-Markovian dynamic [158]. By including the waveguide at the Hamiltonian level, the QTDW model side steps this problem and we can directly calculate the correlation functions at any photon bin, including the output bin.

We begin by describing how to obtain the second-order quantum auto-correlation function as it is the more straightforward of the two. Since we are working with a CW pump field, we are interested in the steady state behavior of the following two-time correlation function:

$$[g^{(2)}_{\text{out}}(t_2)]_{\text{ss}} = \frac{\langle B_0^\dagger(0) B_0^\dagger(t_2) B_0(t_2) B_0(0)\rangle_{\text{ss}}}{\langle B_0^\dagger B_0\rangle_{\text{ss}}^2}, \tag{3.16}$$

where t_2 represents the time after steady state is reached (defined here at (0) in the correlation function). Due to the stochastic nature of the QT technique, we calculate this quantity for individual trajectories and then average over a large number of realizations to arrive at the ensemble average. For good convergence, typically thousands of trajectories are required, which in total take on the order of tens of minutes to run on a single computer.

In the numerical algorithm, an initial set of regular trajectories must first be run to identify when steady state is reached, denoted by t_{ss} which is defined as 0 in Eq. (3.16). Then, the trajectory, $|\psi(t)\rangle$, is run following the prescribed algorithm until t_{ss} is reached.

On the final time step, the process is stopped before the simulated measurement is done on the final bin of the system in step 2 of the algorithm (to avoid losing the information in the 0^{th} bin). At this point, the operator B_0 is applied to the ket vector, $|\psi'(t_{\text{ss}})\rangle = B_0\,|\psi(t_{\text{ss}})\rangle$, i.e., we force a simulated detection of a photon in the bin leaving the system. Then the final two steps of the algorithm are finished by stepping all of the bins forward and renormalizing. The new $|\psi'\rangle$ is then evolved forward in time following the four-step algorithm, with the observable

$$G^{(2)}_{\text{out}}(t_2) = \langle\psi'(t_2)|B_0^\dagger B_0|\psi'(t_2)\rangle\,, \tag{3.17}$$

being calculated at each time step. The final normalized second order correlation function is

$$[g^{(2)}_{\text{out}}(t_2)]_{\text{ss}} = \frac{G^{(2)}_{\text{out}}(t_2)}{\langle B_0^\dagger B_0\rangle_{\text{ss}}}, \tag{3.18}$$

where, due to the renormalization that already occurs each time step when evolving $|\psi'(t_2)\rangle$, $\langle B_0^\dagger B_0\rangle_{\text{ss}}$ is used rather than the square as appears in Eq. (3.16).

As a consequence of the approximation that there is only one photon in any single bin[2] (which is not a serious restriction as the bin populations are typically very small), this formally sets

$$[g^{(2)}_{\text{out}}(0)]_{\text{ss}} = 0. \tag{3.19}$$

However, the quantity $[g^{(2)}_{\text{out}}(\Delta t)]_{\text{ss}}$ can be used as an analogous value to $[g^{(2)}_{\text{out}}(0)]_{\text{ss}}$ because it gives the smallest time step between photon emissions in the QTDW model and can still indicate whether sub- or super-Poissonian light is being emitted.

The *incoherent* spectrum from the waveguide output is also a good observable to investigate multi-quanta effects, as it will contain resonances beyond those from the TLS, and shows signatures of coherent bath control through feedback. This spectrum is obtained from

$$\begin{aligned} S^{\text{out}}_{\text{incoh}}(\omega) = \int_0^\infty dt_2 e^{i(\omega-\omega_{\text{L}})t_2} \Big[&\langle B_0^\dagger(t_2)B_0(0)\rangle_{\text{ss}} \\ &- \langle B_0^\dagger(0)\rangle_{\text{ss}}\,\langle B_0(0)\rangle_{\text{ss}}\Big]\,, \end{aligned} \tag{3.20}$$

where the first term in the integrand is the unnormalized first order auto-correlation function, $G^{(1)}_{\text{out}}(t_2)$, and the second term is composed of steady-state expectation values that can be readily calculated with the QTDW model.

[2]Note that we can still have two photons in different spatial bins.

Calculating $G^{(1)}_{\text{out}}(t_2)$ with the QTDW model is less intuitive than the second order correlation function [176, 178, 225]. Similar to our approach for the second order correlation function, the first step is to identify when steady state is reached, t_{ss}, from the ensemble average system dynamics. Then the trajectory is evolved until t_{ss}, but on the final time step we stop before step 2 of the algorithm, as we did before when calculating $[g^{(2)}_{\text{out}}(t_2)]_{\text{ss}}$. Here, the process differs, two copies of the system ket vector are made, a "lead trajectory" which is unmodified, $|\psi'_{\text{lead}}(0)\rangle = |\psi(t_{\text{ss}})\rangle$, and a "follower trajectory" to which we apply B_0, $|\psi'_{\text{fol}}(0)\rangle = B_0\,|\psi(t_{\text{ss}})\rangle$ The time step is then completed for the lead trajectory by completing steps 3 and 4 of the algorithm. For the follower trajectory, the bins are stepped forward in step 3, but in step 4 the trajectory is renormalized as

$$|\psi_{\text{fol}}(0)\rangle = \frac{|\psi'_{\text{fol}}(0)\rangle}{\sqrt{\langle\psi'_{\text{lead}}(0)|\psi'_{\text{lead}}(0)\rangle}}, \tag{3.21}$$

so that it follows the normalization of the lead trajectory.

The lead trajectory then evolves following the four-step algorithm, during which it continues to have stochastic jump events from C_0, C_1, and (simulated) detections from the final bin. The *follower* trajectory evolves by following the same sequence of jump events that the lead trajectory underwent and at the end of each time step is then projected onto the length of the lead trajectory following Eq. (3.21). To calculate the correlation function, we compute

$$G^{(1)}_{\text{out}}(t_2) = \langle\psi_{\text{lead}}(t_2)|B_0^\dagger|\psi_{\text{fol}}(t_2)\rangle\,. \tag{3.22}$$

However, rather than calculating this at the end of each time step, it needs to be calculated after step one of the algorithm is completed but before the final bin is measured in step two.

If the normalized correlation function is desired, then one can calculate this through

$$[g^{(1)}_{\text{out}}(t_2)]_{\text{ss}} = \frac{G^{(1)}_{\text{out}}(t_2)}{\sqrt{\langle B_0^\dagger(t_2)B_0(t_2)\rangle_{\text{ss}}\,\langle B_0^\dagger(0)B_0(0)\rangle_{\text{ss}}}}, \tag{3.23}$$

where the first expectation value in the denominator is the bin population of B_0 at time t_2 from the lead trajectory and the second expectation value is the population of B_0 from the lead trajectory when $t_2 = 0$.

3.3 Results

In this section, we apply our extended QTDW approach to several systems. First we show that it correctly produces feedback induced changes to the Mollow triplet and explain

these changes in the context of $[g^{(2)}_{\rm out}(t_2)]_{\rm ss}$ and $W(t')$. Then we characterize the effect of the delay time, τ, and the round trip phase change, ϕ, on the waveguide output and the photon number distribution in the feedback loop. Finally, we drive the system with a strong CW-pump to excite the additional resonances from the feedback loop in the output spectrum.

A single TLS excited by an on-resonance CW laser, with Rabi frequency $\Omega = 2\pi\gamma$, will emit a spectrum with the distinctive Mollow triplet, including a central resonance at the frequency of the laser $\omega_{\rm L}$ and two side peaks at $\omega - \omega_{\rm L} = \pm\Omega$. By introducing a relatively short feedback loop, the central peak can disappear, such that with the proper choice of the round trip phase only the side peaks remain [38]. In Fig. 3.2(b) the incoherent output spectra for the TLS without feedback (with round trip time $\tau \to \infty$), and the TLS coupled to a short feedback loop (with round trip time $\tau = 0.1\gamma$) are shown, where in the short loop case two values of round trip phase are considered, $\phi = 0$ and $\phi = \pi$. When $\phi = 0$, the effect of feedback is such that the spectral peaks have the same heights as the no feedback case, but are all broadened. For $\phi = \pi$, the side peaks are significantly sharpened and the central peak almost completely removed.

In the Heitler regime, when the Rabi frequency is small, the spectrum becomes single peaked and the Mollow Triplet is no longer seen [104, 105, 158]. For a Rabi frequency of $\Omega = 0.2\pi\gamma$, Fig. 3.2(a) shows the output spectrum both with and without feedback. With this weak pump and short delay time, the field within the waveguide remains quite weak. A choice of $\phi = 0$ again leads to broadening of the central peak as the weak field constructively interferes with itself. When $\phi = \pi$, the single photon in the loop field destructively interferes with the TLS output and only a very small output flux remains. This causes the central peak to be suppressed and only extremely sharp sidepeaks remain. For a Mollow triplet, the side peaks are at $\pm\Omega$, however the feedback modifies this as these two peaks are no longer purely the dressed states of the TLS and laser. Instead, these states are dressed by the additional field modes that are set up in the waveguide causing the peaks to shift.

To achieve maximal constructive and destructive interference, the condition for the round trip phase change is $\Omega\tau/2 - \phi = (2k-1)\pi$ for destructive interference and $\Omega\tau/2 - \phi = 2k\pi$ for constructive interference with $k \in \mathbb{Z}$. For the interference to be complete (i.e. no output for the case of destructive interference) there is a further requirement of $\Omega\tau = 2n\pi$ for $n \in \mathbb{Z}$ to match the phase of the Rabi oscillations. For a short loop and weak drive, this interference occurs maximally when $\phi \approx 0$ for constructive interference and $\phi \approx \pi$ for destructive interference.

This is readily seen by comparing the output flux from the loop, $n_{B_0}(t)$, in Fig. 3.2(c),

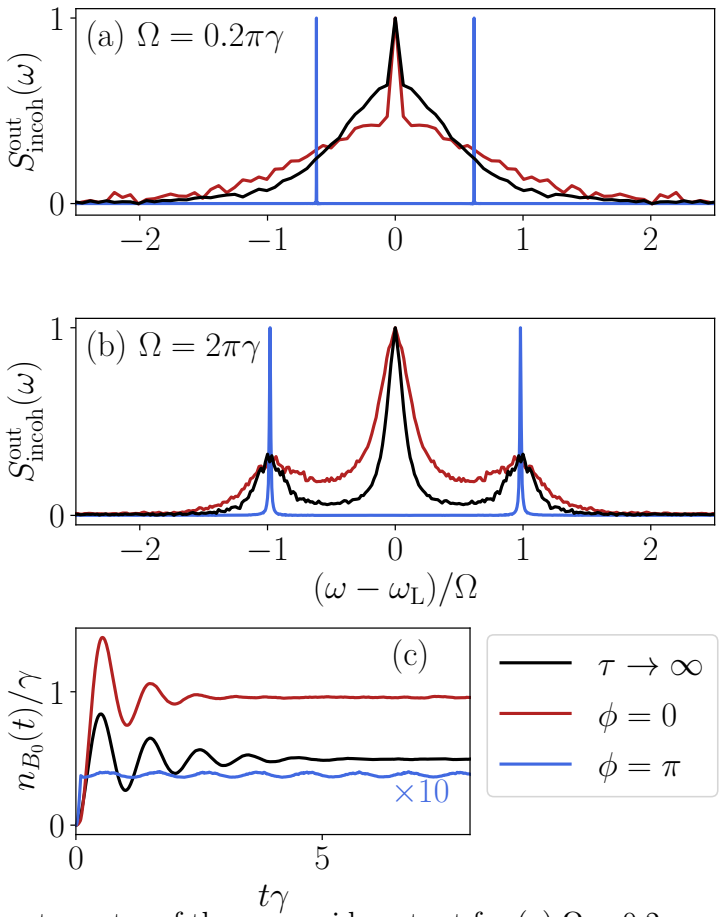

Figure 3.2: Incoherent spectra of the waveguide output for (a) $\Omega = 0.2\pi\gamma$ and (b) $\Omega = 2\pi\gamma$. For the spectrum in (b) the output photon flux is in (c). For a TLS driven on resonance without feedback, $\tau \to \infty$ (black) and with a short feedback loop, $\tau = 0.1\gamma^{-1}$, for $\phi = 0$ (red) and $\phi = \pi$ (blue); 20,000 trajectories were used for $\tau \to \infty$ and $\phi = \pi$, and 50,000 trajectories for $\phi = 0$.

for the three setups. In the *one-photon-in-the-loop* approximation, the output from the waveguide at $\omega_{\rm L}$ will be suppressed when $\phi = \pi$ is consistent with the findings in Refs. [168, 173, 185]. The approximation is good in the limit when $\gamma\tau \to 0$, i.e. when the field in the feedback loop is weak ($\gamma \to 0$) or the dynamics can be treated in the Markovian regime ($\tau \to 0$), but fails when the non-Markovian dynamics are required. Allowing for two photons in the loop, as we do here, means that the feedback *cannot* match the phase requirements for destructive interference of the two different photon frequencies simultaneously when $\phi = \pi$ [46]. Thus, the loop acts to meet the phase requirements of the central $\omega = \omega_{\rm L}$ peak (and thus suppress the peak) while the side peaks remain.

When the feedback interferes constructively when $\phi = 0$, the waveguide emission from the system is much faster and this acts to broaden the emission while retaining the general Mollow triplet shape. For intermediate choices of ϕ between 0 and π, the interference is no longer maximal and as the phase is varied, the observables vary continuously between the behavior of the two maximal interference cases.

The photon counting statistics of the waveguide output are also strikingly affected by the introduction of a time-delayed coherent feedback. By virtue of having only two energy levels, a TLS in an infinite waveguide will nominally emit sub-Poissonian light with $[g^{(2)}_{\text{out}}(0)]_{\text{ss}} = 0$. The response is similar when a short feedback loop, $\tau = 0.1\gamma^{-1}$, is included with $\phi = 0$ and these are overlaid in Fig. 3.3(a). When feedback is included, the response remains sub-Poissonian but loses the second-order correlations in time much faster (the red line in Fig. 3.3(a) decaying to steady state more quickly than the black) due to the increased output from the system. However, when $\phi = \pi$, as in Fig. 3.3(b), the statistics of the outgoing light switches to highly super-Poissonian over a period of time equal to the delay time of the feedback. These two starkly different regimes can allow feedback to be used to tune the characteristics of the outgoing light depending on the intended use.

In Fig. 3.2, a relatively short feedback loop is used, $\tau = 0.1\gamma^{-1}$, in order to maintain coherence between the returning field in the feedback loop and the emitted field from the TLS. As the delay time increases, the feedback becomes increasingly sensitive to meeting the exact phase matching conditions for interference as the coherence between the two fields decreases. However, other channels for decoherence, such as pure dephasing, also have an effect on how well the feedback works.

In Fig. 3.4 we have introduced the Lindblad output channels (off chip decay and pure dephasing), to see to what degree they disrupt the effect of feedback when $\phi = \pi$ leading to destructive interference. Off chip decay from the TLS is included in Fig. 3.4(a) at a rate of $\gamma_0 = 0.1\gamma$ which is typical of state of the art TLS sources such as QDs [234, 235]. This output channel does not greatly affect the response of the output flux because whenever a quantum jump occurs, the TLS is emptied and so any returning feedback is met with no field; thus, no interference occurs and the system quickly returns to its steady state behavior. However, when pure dephasing is included in Fig. 3.4(b), we see a much more pronounced effect as the output flux out of the system is increased approximately twentyfold when $\gamma' = \gamma$. In this case, when a jump occurs, the phase of the TLS flips. The returning feedback is thus met with constructive interference and the output from the system is enhanced leading to the increased flux out of the system. Note though, that the steady state output flux when $\gamma' = \gamma$ is still much reduced from the case without feedback which is shown as the black line in Fig. 3.2(c). In the case of $\phi = 0$, similar physics is seen when including these output channels. Off-chip decay continues to have little effect on the

steady state output flux while dephasing now works to spoil the constructive interference in the output fields. This causes the steady state output flux to decrease as the dephasing rate increases, from $[n_{B_0}/\gamma]_{\rm ss} \approx 0.45$ without any output channels to $[n_{B_0}/\gamma]_{\rm ss} \approx 0.34$ when $\gamma' = \gamma$. To limit the amount of pure dephasing in QD systems, usually one works at lower temperatures, and gated QDs can also reduce the charge noise significantly [236, 237].

Pure dephasing can also act to qualitatively change the emitted spectrum. Under off-resonant pumping, the Mollow triplet becomes asymmetrical when pure dephasing is included [109, 238, 239]. We show how the inclusion of feedback affects this result in Fig. 3.5. The detuning between the laser and TLS is $\delta = 5\gamma$ and the Rabi frequency if $\Omega = 2\pi$. The rate of pure dephasing is $\gamma' = 0.5\gamma$. When a short feedback loop is included ($\tau = 0.1\gamma^{-1}$), the spectral asymmetry is not as pronounced. When $\phi = 0$, the asymmetry remains, however now the largest peak is the central peak. When $\phi = \pi$, only a small amount of asymmetry in the spectrum shape remains and the peak heights are now symmetrical. For the remaining results we will neglect the two dissipation channels to present optimal results as we remain on resonance.

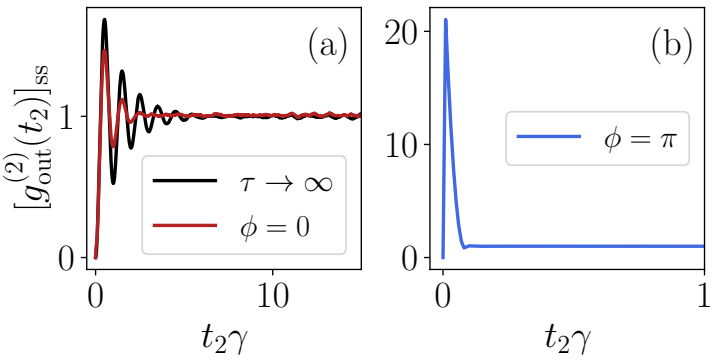

Figure 3.3: The second-order quantum correlation function for the three setups described in Fig. 3.2(b). For both with and without feedback in (a) the output is sub-Poissonian while in (b) it is super-Poissonian. Note that in (b) the correlation function begins at 0 but then immediately jumps to >1 on the next time step since there is a maximum of one photon in each bin. These results are an average of 20,000 trajectories each.

The WTDs of the waveguide output give us additional insight into how feedback is changing the system dynamics. Without feedback, in Fig. 3.6(a), the system goes through periodic peaks of photon emission which quickly die off as the waiting time gets much longer than the lifetime of the TLS. As expected, there is a very small probability of back to back jumps since the output light is sub-Poissonian.

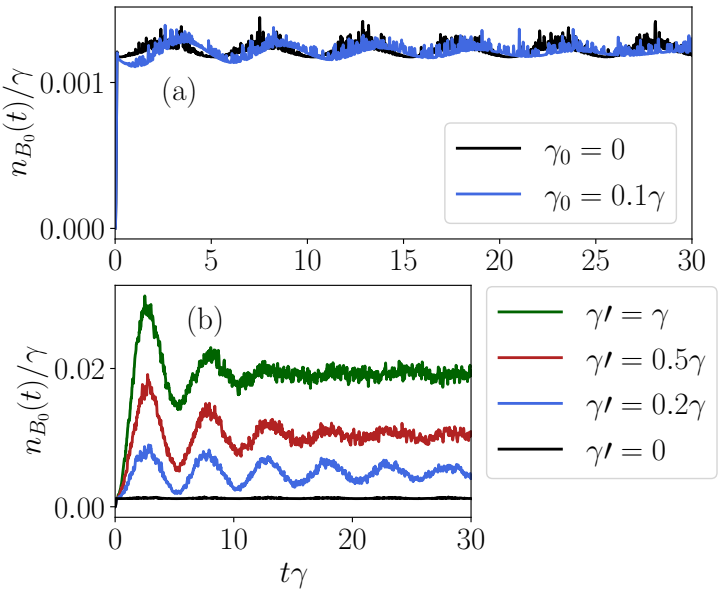

Figure 3.4: Effect on the output photon flux from the inclusion of the Lindblad output channels; (a) off chip decay and (b) pure dephasing. The TLS is driven on resonance with $\Omega = 0.4\pi\gamma$ with a feedback loop of delay time $\tau = 0.1\gamma^{-1}$ and $\phi = \pi$. Each result is an average of 20,000 trajectories.

When feedback is introduced, as shown in Fig. 3.6(b), there is a sharp jump at the beginning of the WTD, over the length of the delay time, indicating that there is a significant population of back-to-back emissions occurring. After this initial spike, the distribution is almost flat, out to very long waiting times; indeed the graph in Fig. 3.6(b) is truncated for readability and the distribution tapers out to $t' = 60\gamma^{-1}$. This indicates that if a photon pair emission does not occur, the next emission is uncorrelated with the previous emission, which agrees with the correlation function of Fig. 3.3(b). This dynamic also plays out in the output flux from the system after a jump event occurs.

Figure 3.6(c) shows a snapshot of the output flux in a trajectory immediately after a jump occurs for two separate jump events. The flux immediately increases and becomes much larger over the timescale of a single round trip. This sharp increase is due to the suppressed probability of a single photon in the loop from the destructive interference of the output bin. If a photon is detected, than it is more likely to have a second photon in the loop coming around than it is to have an empty loop. If a second emission event does not occur before the round trip ends then the flux settles back into the near constant value before the jump occurred. There are slight fluctuations in the between jump output flux,

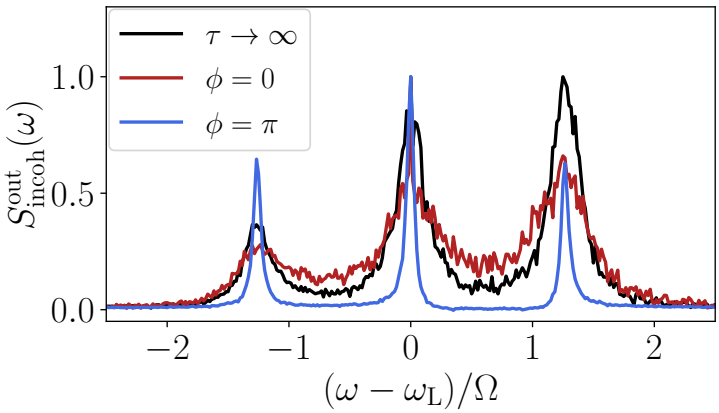

Figure 3.5: Asymmetric Mollow triplet from the TLS driven off resonance ($\delta = 5\gamma$, $\Omega = 2\pi\gamma$) with pure dephasing ($\gamma' = 0.5\gamma$) with and without feedback ($\tau = 0.1\gamma^{-1}$). Each result is an average of 20,000 trajectories.

which is what determines the peak output flux after a jump occurs.

We now turn to investigating the effect of increasing the length of the feedback loop (and thus the delay time). Figs. 3.7(a) and (b) show the effect of increasing the delay time on the anti-bunching and bunching for both $\phi = 0$ and $\phi = \pi$, respectively; here, the pump strength is decreased to $\Omega = 0.4\pi\gamma$ to avoid driving too many of the system resonances, which increase the complexity of the photon counting statistics. As the loop length increases, both setups show worse statistics as they become less anti-bunched and less bunched. This is again due to the loss of coherence between the feedback and TLS. When $\phi = 0$, increasing the delay time acts to increase probability of having two photons in the loop. Therefore, when a jump occurs the remaining field in the feedback loop is non-zero. Conversely, when $\phi = \pi$, the loss of coherence causes the destructive interference between the one photon in the loop field and TLS to no longer be perfect. Somewhat counter intuitively, this means when a jump occurs, it becomes less probable that there are two photons in the loop as the loop increases in length.

It is interesting to note that the larger population in the loop actually increases the likelihood of a photon pair emission when $\phi = \pi$. When $\tau = 2\gamma^{-1}$, the WTD for the waveguide output is shown in Fig. 3.7(c) for $\phi = 0$ and (d) for $\phi = \pi$. The lifetime of the WTD when $\phi = \pi$ is much longer showing the increased waiting time between individual jumps, but also the initial peak is larger than the $\phi = 0$ case showing an increase in photon pair emission. Figure 3.7(e) and (f) show the probability for one and two photons in the loop in the steady state as a function of delay time for $\Omega = 0.4\pi\gamma$ and $\Omega = 2\pi\gamma$,

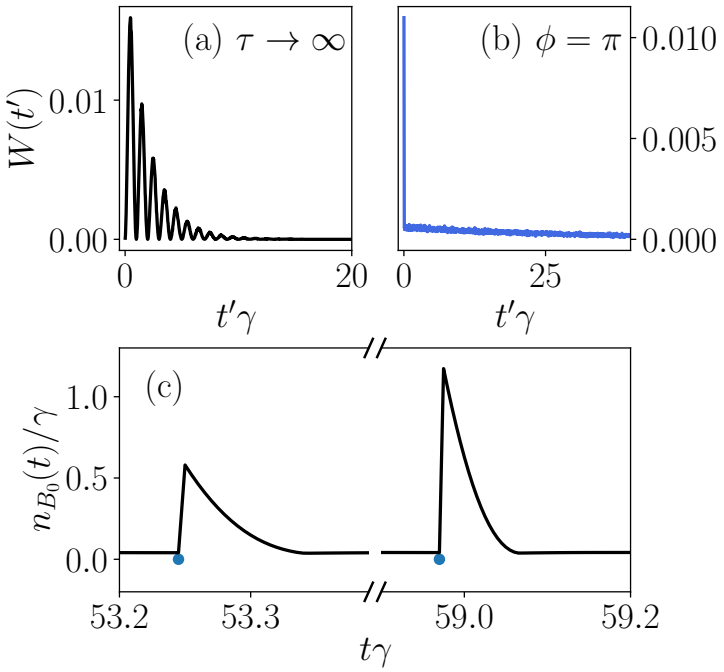

Figure 3.6: The WTDs for a TLS driven on resonance with $\Omega = 2\pi\gamma$ and with (a) no feedback or (b) feedback from a short loop with $\tau = 0.1\gamma^{-1}$ and $\phi = \pi$. In (c) two jump events during a trajectory are shown for the setup in (b) to illustrate the increase in output flux after a jump occurs.

respectively, when $\phi = 0$ (note that the probabilities for one or two photons remain about same in the steady state when $\phi = \pi$). The probability to have two photons in the loop remains small past a delay time of $\tau = 2\gamma^{-1}$. For example at $\tau = 2.5\gamma^{-1}$, the probability is $p(2, t_{\rm ss}) \approx 0.03$ for $\Omega = 0.4\pi\gamma$ and the probability is $p(2, t_{\rm ss}) \approx 0.11$ for $\Omega = 2\pi\gamma$, small enough for our approximation of a maximum of two photons in the loop to be valid.

In Fig. 3.8, we compare the time dynamics of the $p(n, t)$ as we vary the round trip phase change, delay time, pump strength and introduce off-chip decay and pure dephasing. In Figs. 3.8(a) and (b) we plot $p(n, t)$ as a function of the round trip phase change and the delay time, respectively, for $n = 1$ and 2. As expected, we see that for $\phi = \pi$ the long-lived system Rabi oscillations are passed on to the loop probabilities, while for $\phi = 0$ we do not see these oscillations. The increasing delay time also acts as expected to increase the probabilities of having both one and two photons in the loop since the feedback loop itself is longer and holds more of the emitted field from the TLS. In Fig. 3.8(c) the pump strength is increased to $\Omega = 2\pi\gamma$. Although the probability to have one photon in the loop

remains approximately the same, the probability for two photons almost doubles as the TLS is pumped harder. We also see the Rabi oscillations reflected in the loop probabilities die out faster for the larger pump strength. Lastly, we introduce both Lindblad output channels with $\gamma_0 = 0.1\gamma$ and $\gamma' = 0.5\gamma$ in Fig. 3.8(d), which act to decrease the probability to find either one photon or two photons in the loop and reduce the Rabi oscillations.

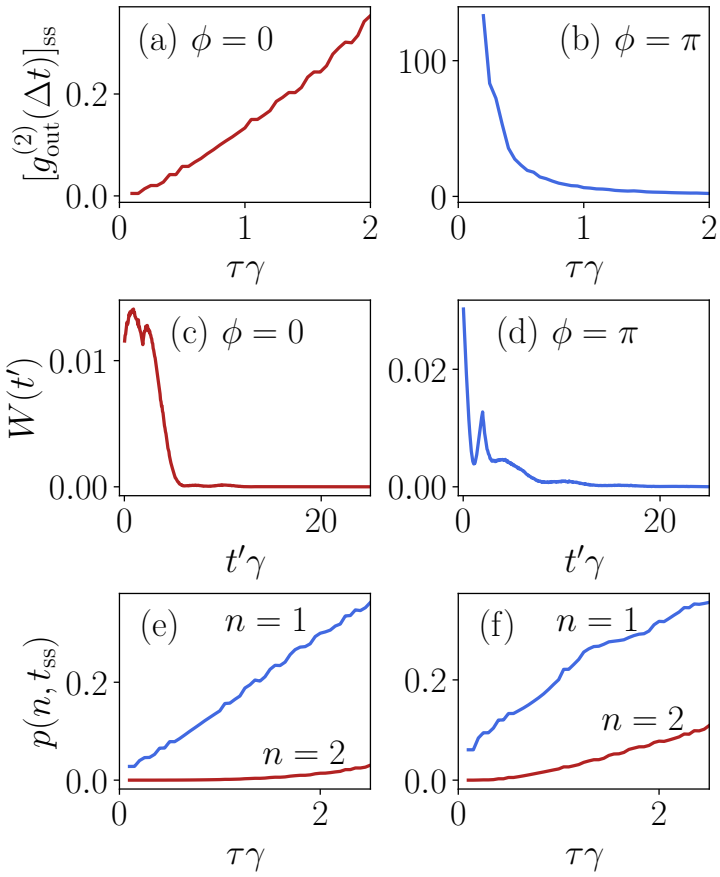

Figure 3.7: Comparison of the near-equal time second-order correlation function as a function of delay time for a TLS driven on resonance with $\Omega = 0.4\pi\gamma$ and round trip phase change of (a) $\phi = 0$ and (b) $\phi = \pi$. For the setup with the longest delay time in (b) ($\tau = 2.0\gamma^{-1}$), we show the WTD in (c) for $\phi = 0$ and in (d) for $\phi = \pi$. We show the probability to have $n = 1$ and 2 photons in the loop (the blue and red lines respectively) as a function of delay time when $\phi = 0$ for drive strengths of (e) $\Omega = 0.4\pi\gamma$ and (f) $\Omega = 2\pi\gamma$. The results are an average of 10,000 trajectories for each delay time.

As the delay time from the feedback loop becomes non-negligible, the peak bunching

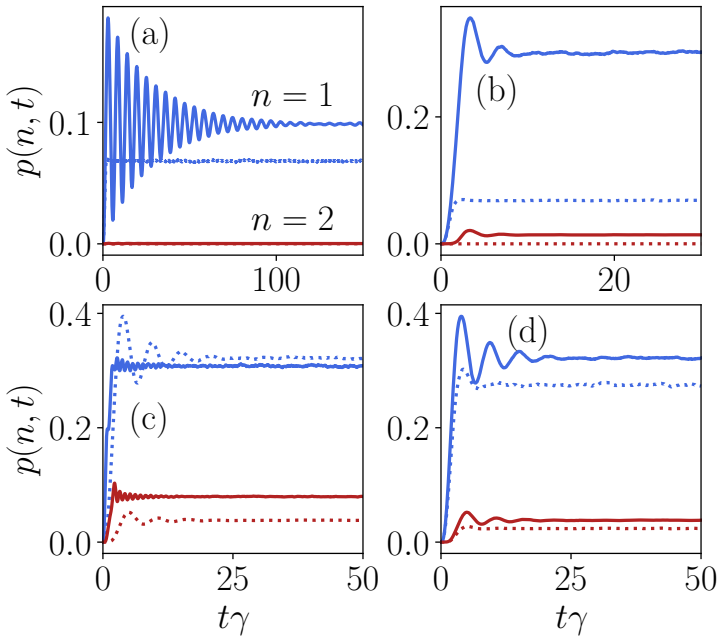

Figure 3.8: Time evolution of the probability of having $n = 1$ and 2 photons in the loop (the blue and red lines, respectively). In (a), we set $\Omega = 0.4\pi\gamma$ and $\tau = 0.5\gamma^{-1}$ for $\phi = 0$ (dashed) and $\phi = \pi$ (solid). In (b), $\Omega = 0.4\pi\gamma$ and $\phi = 0$ for $\tau = 0.5\gamma^{-1}$ (dashed) and $\tau = 2\gamma^{-1}$ (solid). In (c), $\tau = 2\gamma^{-1}$ and $\phi = \pi$ for $\Omega = 0.4\pi\gamma$ (dashed) and $\Omega = 2\pi\gamma$ (solid). Lastly, in (d) when $\Omega = 0.4\pi\gamma$, $\tau = 2\gamma^{-1}$, and $\phi = \pi$, we compare the case with no outputs (solid, $\gamma_0 = \gamma' = 0$) to that where both Lindblad output channels are included (dashed, $\gamma_0 = 0.1\gamma$ and $\gamma' = 0.5\gamma$). Each result is an average of 20,000 trajectories.

does not occur when $\phi = \pi$ as for the short loop but rather at $\Omega\tau/2 - \phi = (2k-1)\pi, k \in \mathbb{Z}$ as shown in Fig. 3.9 for three different choices of loop length. This condition arises due to phase matching of the Rabi oscillations in the TLS with the phase of the returning field. Matching this condition would always give the peak bunching in the one photon in the loop limit; however, when two photons are present this is not the case as the peaks shift slightly and are not always the dominant phase choice for bunching as shown in Fig. 3.9(c). Here, $\tau = 2.0\gamma^{-1}$ and $\Omega = 0.4\pi\gamma$, so we would expect the peaks at $\phi = 0.6\pi, 1.4\pi$; instead these are present but the central peak is at $\phi = \pi$. This likely comes back to the fact that when there is a probability for two photons in the loop, they both cannot be phase matched at the same time for complete interference. Thus, at the longer loop lengths when the loop population increases, a maximal $[g^{(2)}_{\text{out}}(\Delta t)]_{\text{ss}}$ occurs when $\phi = \pi$ and the returning field interferes at the center frequency rather than trying to match the one photon in the loop

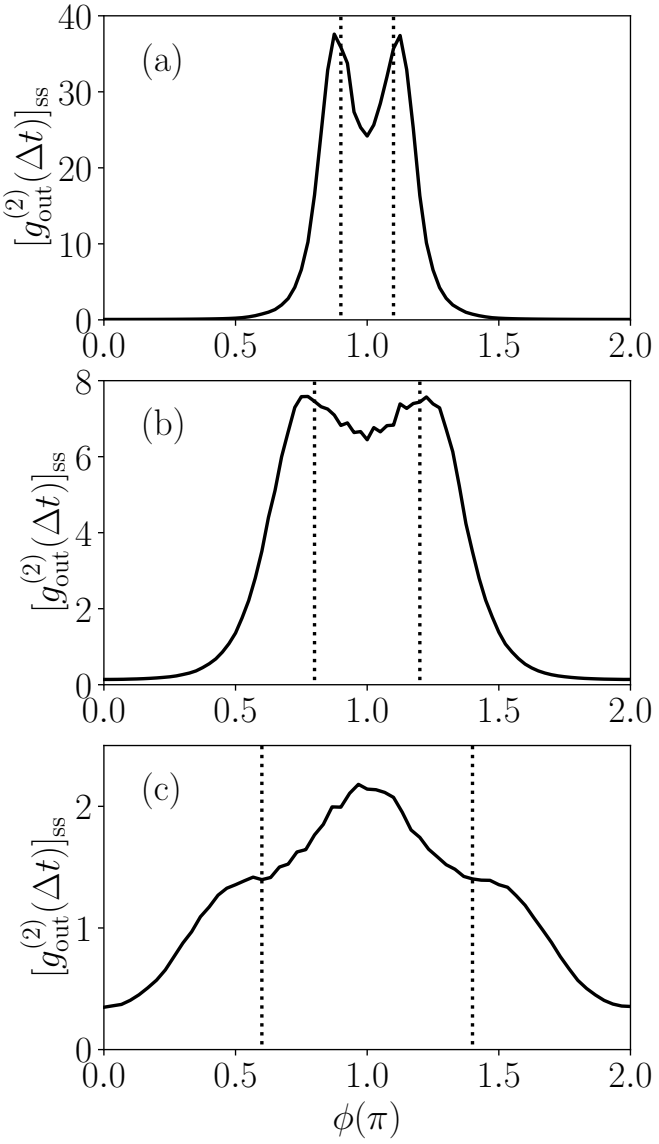

Figure 3.9: Comparison of the near-equal time second-order correlation function as a function of the round trip phase change, for three delay times: (a) $\tau = 0.5\gamma^{-1}$, (b) $\tau = 1.0\gamma^{-1}$, and (c) $\tau = 2.0\gamma^{-1}$. The vertical lines denote the phase matching condition $\Omega\tau/2 - \phi = (2k-1)\pi, k \in \mathbb{Z}$. The TLS is driven on resonance with $\Omega = 0.4\pi\gamma$. The result for each round trip phase change is an average of 10,000 trajectories.

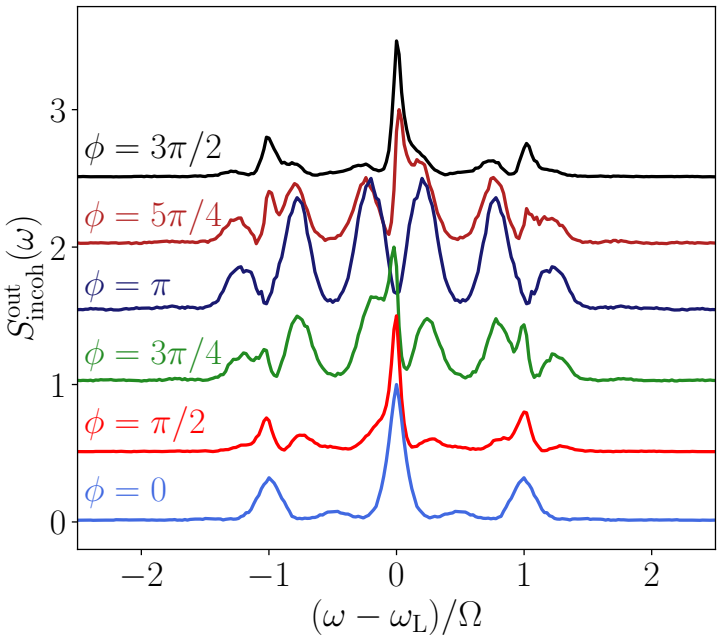

Figure 3.10: Four incoherent output spectra when the system is driven on resonance with $\Omega = 2\pi\gamma$ and the feedback is introduced with a delay time of $\tau = 2.0\gamma^{-1}$ for round trip phase changes of $\phi = 0$, $\phi = \pi/2$, $\phi = \pi$, and $\phi = 3\pi/2$. Each spectra is an average of 20,000 trajectories.

field.

Furthermore, as the population in the loop increases this gives rise to additional resonances in the output spectrum arising from the feedback loop. These additional resonances are at $\omega - \omega_{\text{L}} = (2\pi k + \phi)/2\pi\tau$ and we show example spectra in Fig. 3.10 for $\Omega = 2\pi\gamma$, $\tau = 2.0\gamma^{-1}$, and six choices of round trip phase change. These resonances are a result of the multi-mode cavity resonances set up via multiple round trips around the feedback loop, where the TLS acts as a second mirror, analogous to the Fabry-Pérot resonances set up in a closed cavity coupling to the Mollow triplet. The cavity QED physics that begins to be introduced is fully picked up by the QTDW model at the system level where truncating to two photons in the loop is analogous to truncating the cavity to a ground state and two excited state levels.

3.4 Discussion on Potential Experimental Systems to Exploit Coherent Feedback

For optical frequencies, state of the art qubits in typical photonic waveguides typically exhibit decay rates on the order of $\gamma = 1$ ns^{-1} [235]. For example, if we embed such emitters into a low loss SiN waveguide (assuming a group index of 2), then the required waveguide length of $L_0/2 = 0.75$ cm for a "short" feedback loop, with delay time $\tau = 0.1\gamma^{-1}$. Such integration schemes have now been demonstrated experimentally, using QD nanowires and SiN waveguides [27]. For the more extreme delay time of $\tau = 2\gamma^{-1}$, as used in Fig. 3.10, then $L_0/2 = 15$ cm. So low loss waveguides are required, though the lengths could be reduced by designing slow light waveguides modes with a larger group index. To control the tuning of the round trip phase, this would require moving the QD a distance of half a wavelength to change the phase from $\phi = 0$ and $\phi = \pi$, or a means to tune the mirror phase or group velocity.

In order to shorten the required feedback length, the QD can also be placed in a cavity (such as a Fabry-Pérot cavity or ring resonator) to include a Purcell factor, P_F, to the decay rate. This would decrease the required waveguide length to be $L_0/2P_F$. For example, a modest Purcell factor of 10, would decrease the range of the waveguide length to be $L_0/2 \in [0.75, 15]$ mm, where waveguide loss is less of a problem.

At microwave frequencies, one can also exploit highly developed circuit QED systems [240, 241], where multiple qubits can be controlled in position with great precision [242] (even multiple qubits can be spatially controlled to fractions of a wavelength). Here the physical length scales are of course much larger, but all the results equally apply in scaled units.

3.5 Conclusions

We have introduced an open-system quantum optics theory to study the nonlinear behavior of an optically pumped TLS in a waveguide system, with a time-delayed coherent feedback. To do this, we described an extension to a previous QT model of coherent feedback [46] to explicitly characterize the waveguide output from the system. We have shown how one can obtain the first- and second-order correlation functions using the QTDW model and in turn the incoherent output spectra. We then showed a number of results focusing on how the multi quanta effects from the feedback loop affect the output observables. Notably, with the proper phase matching conditions, the feedback can be used to filter out the

central laser peak, switch the system through anti-bunched and bunched light output, and enhance the photon pair emission from the system. We also show how the feedback loop can introduce new resonances into the output spectra.

By focusing on incorporating practical experimental observables, along with the unique stochastic insights from QT theory, this approach is useful to connect to experimental realizations of time-delayed coherent feedback. The inclusion of pure dephasing, an important experimental consideration, is a natural addition to the QTDW model but can be added into the MPS formalism with some added complexity [171]. To continue expanding on the practical usefulness of this approach, the addition of incoming photon wavepackets from the waveguide input rather than a CW-drive is necessary to investigate the effect of feedback on the single photon source properties of the TLS. Also, an expansion of the TLS to multi-exciton or biexciton systems will more accurately represent the experimental reality of embedded QDs [101].

3.6 Acknowledgements

This work was supported by the Natural Sciences and Engineering Research Council of Canada, the Canadian Foundation for Innovation, the National Research Council of Canada, Queen's University and the University of Ottawa. We thank Dan Dalacu and Robin Williams for support and useful discussions.

3.7 Appendix A: Deriving the Interaction Hamiltonian

The free field of the waveguide is described by

$$\mathcal{E}(x) = \mathcal{E}_{-}(x) + \mathcal{E}_{+}(x), \tag{3.24}$$

where $\mathcal{E}_{-}(x)$ and $\mathcal{E}_{+}(x)$ are the left and right propagating fields respectively, with the explicit form

$$\mathcal{E}_{\pm}(x) = \mp\frac{1}{\sqrt{2\pi}}\int_{\infty}^{\infty} e^{\pm i\omega x/c} b(\omega) d\omega, \tag{3.25}$$

where c is the group velocity of the waveguide mode with frequency ω. Due to the reflection from the mirror, we can write $\mathcal{E}_{+}(0)$ in terms of $\mathcal{E}_{-}(0)$ by including the phase change picked

up from the round trip,

$$\mathcal{E}_+(0) = e^{i(\phi_M + \omega\tau)}\mathcal{E}_-(0), \tag{3.26}$$

where $x = 0$ is the location of the mirror. Then the interaction between the TLS and this free field at $x = 0$ is

$$H_{\mathrm{I}} = \sqrt{\frac{\gamma}{2}}\sigma^+\frac{\mathcal{E}_-(0)}{2} + \sqrt{\frac{\gamma}{2}}\sigma^+\frac{\mathcal{E}_+(0)}{2} + \mathrm{H.c.} \tag{3.27}$$

Next, substituting Eqs. (3.25) and (3.26) into Eq. (3.27), we get our interaction Hamiltonian

$$H_{\mathrm{I}} = \int_{-\infty}^{\infty} d\omega \left[\left(\sqrt{\frac{\gamma}{4\pi}}\sigma^+ b(\omega) + \sqrt{\frac{\gamma}{4\pi}}e^{i(\phi_M+\omega\tau)}\sigma^+ b(\omega)\right) + \mathrm{H.c.}\right]. \tag{3.28}$$

3.8 Appendix B: Deriving the Evolution of the Waveguide Operators

Generally, the free evolution of the waveguide is described by the unitary operator $U_{\mathrm{W}}(t) = e^{-iH_{\mathrm{W}}t}$ and the evolution of each discrete bin is $U_{\mathrm{W}}^\dagger(t)B_nU_{\mathrm{W}}(t)$. Over one time step these exponentials can be expanded to first order in Δt to be

$$U_{\mathrm{W}}(\Delta t) = e^{-iH_{\mathrm{W}}\Delta t} = 1 - iH_{\mathrm{W}}\Delta t, \tag{3.29}$$

which can be substituted into the evolution of B_n to get

$$U_{\mathrm{W}}^\dagger(\Delta t)B_nU_{\mathrm{W}}(\Delta t) = (1 + iH_{\mathrm{W}}^\dagger\Delta t)B_n(1 - iH_{\mathrm{W}}\Delta t). \tag{3.30}$$

Then expressing this in terms of the b_k operators and expanding to first order in Δt, we get

$$\begin{aligned} U_{\mathrm{W}}^\dagger(\Delta t)B_nU_{\mathrm{W}}(\Delta t) = \frac{1}{\sqrt{N}}\sum_{k=0}^{N-1} b_k e^{i(\omega_k-\omega_0)n\Delta t} \\ + \frac{i\Delta t}{\sqrt{N}}\sum_{k,k'=0}^{N-1}(\omega_k - \omega_{\mathrm{L}})e^{i(\omega_{k'}-\omega_0)n\Delta t}\left(b_k^\dagger b_k b_{k'} - b_{k'}b_k^\dagger b_k\right). \end{aligned} \tag{3.31}$$

Noting that the commutation relation for b_k is $[b_k, b_{k'}^\dagger] = \delta_{k,k'}$ this reduces to

$$\begin{aligned} U_{\mathrm{W}}^\dagger(\Delta t) B_n U_{\mathrm{W}}(\Delta t) &= \frac{1}{\sqrt{N}} \sum_{k=0}^{N-1} b_k e^{i(\omega_k - \omega_0) n \Delta t} \\ &- \frac{i\Delta t}{\sqrt{N}} \sum_{k,k'=0}^{N-1} (\omega_k - \omega_{\mathrm{L}}) \delta_{k,k'} b_k e^{i(\omega_{k'} - \omega_0) n \Delta t}, \\ &= \frac{1}{\sqrt{N}} \sum_{k=0}^{N-1} b_k e^{i(\omega_k - \omega_0) n \Delta t} \left(1 - i\Delta t(\omega_k - \omega_{\mathrm{L}})\right), \\ &= \frac{e^{-i(\omega_0 - \omega_{\mathrm{L}})\Delta t}}{\sqrt{N}} \sum_{k=0}^{N-1} b_k e^{i(\omega_{k'} - \omega_0)(n-1)\Delta t}, \\ &= e^{-i\delta \Delta t} B_{n-1}, \end{aligned} \tag{3.32}$$

where we have used that

$$(1 - i\Delta t(\omega_k - \omega_{\mathrm{L}})) = e^{-i(\omega_k - \omega_{\mathrm{L}})\Delta t} \tag{3.33}$$

to first order in Δt.

Chapter 4

Resonance fluorescence of an artificial atom with a time-delayed coherent feedback

This work is a submitted manuscript to Nature Communications. I am a co-first author on the work along with Ching Yeh Chen of the National Tsing Hua University in Taiwan. The other co-authors on the paper are Z.-Q. Niu, P. Y. Wen, Y.-H. Lin, J.-C. Chen, Z.-R. Lin, F. Nori, S. Hughes and I.-C. Hoi. The manuscript is reproduced here in the consistent thesis style. This work is a joint experimental and theoretical work that follows up on the predictions of Ch. 3. Here, a transmon qubit coupled to a superconducting circuit terminated by a grounding plane (acting as a mirror) is the coherent feedback system of interest. We present experimental and simulated results in the linear and nonlinear regime which highlight the non-Markovian nature of this system. In the linear regime, the reflection coefficient is observed as a function of the round trip phase change and the pump frequency. We find the feedback induced frequency shift no longer follows the Markovian prediction in [35] and additionally there is a tilt introduced to the complex plane response of the reflection coefficient. In the non-linear regime, experimental results confirm our previous predictions of new resonances appearing in the spectrum with coherent feedback. C. Y. Chen was the primary student working on the experiments with support from Z.-Q. Niu, P. Y. Wen, Y.-H. Lin, J.-C. Chen, Z.-R. Lin, and I.-C. Hoi. I did all of the simulations, including expanding the quantum trajectory discretized waveguide (QTDW) method to simulate the reflection coefficient. Myself and C. Y. Chen both worked on the interpretation of the experimental data to extract the relevant parameters for simulation of the coherent feedback system with the QTDW model. We both also worked on the writing

of the manuscript with feedback and edits from S. Hughes, I.-C. Hoi, and F. Nori. F. Nori initiated the collaboration between the experimental and theoretical sides and provided funding for an internship at the Theoretical Quantum Physics Laboratory and Center for Quantum Computing in RIKEN, a research center in Japan where we were able to work in person on the collaboration.

Abstract

The model of light-matter interaction in quantum electrodynamics typically relies on the Markovian approximation, which assumes that the system's future evolution depends solely on its current state, effectively treating it as a "memoryless" process. However, this approximation is not valid in scenarios when retardation effects are significant. These memory and retardation effects have the potential to improve existing quantum technologies (e.g., large-scale quantum networks, quantum information processing) and unlock new phenomena for future applications. In this work, we show theory and experiments of a time-delayed coherent feedback system using a transmon artificial atom (treated as a qubit) embedded in a superconducting circuit waveguide. By using a feedback loop with a delay time comparable to the qubit relaxation time, pronounced non-Markovian effects appear in the dynamics of the qubit evolution. We also show how the resonance fluorescence spectrum, including elastic and inelastic scattering (such as the well-known Mollow triplet), can be significantly modified through the interaction between the qubit and feedback loop to show genuine non-Markovian phenomena that cannot be explained with instantaneous coupling parameters.

The interaction between a two level system (TLS) and an electromagnetic field is a foundation in quantum optics, with applications in fundamental optical physics and quantum technologies [243]. This system has led to a diverse range of intriguing optical physics, such as photon-antibunching [244], single photon sources [245], squeezed light [246] and Mollow triplets [117, 119, 247]. Under resonant (or near-resonant) driving, the TLS exhibits resonance fluorescence [107], where the emitted spectrum [248] can result in the distinctive Mollow triplet with strong driving [106], featuring a central peak at the frequency of the TLS and two side peaks offset by the Rabi frequency of the pump field. Fluorescence spectra have been demonstrated in various physical systems, including natural atoms [249,

250], chiral artificial atoms [251, 252], quantum dots [108, 109, 247], and superconducting circuits [117–119]. These platforms have also been studied with exotic driving fields such as a squeezed vacuum [246], a dynamical drive [112, 253, 254] and entangled photons [255].

Superconducting circuits provide an exciting platform for studying non-Markovian time delay effects on resonance fluorescence in a single artificial atom waveguide system [64, 256, 257]. A major advantage of these circuits is their low loss and the sub-wavelength control of the light-matter interaction made possible by tuning the qubit's frequency within the circuit. In recent years, considerable progress has been made toward achieving strong coupling between superconducting artificial atoms and propagating microwave photons [240, 251, 258]. Thus superconducting artificial atoms and circuits make excellent candidates for exploring waveguide quantum electrodynamics (QED), with precise tunability.

Using superconducting QED systems, a wide range of quantum field phenomena have been demonstrated. These include resonance fluorescence [117], photon routing [259], non-classical microwaves [260], the cross-Kerr effect between two fields [261], lifetime control of artificial atoms [37], amplification without population inversion [262], the collective Lamb shift between two superconducting qubits [121], giant atoms [240], photon-mediated interactions between atoms [120, 122], and deterministic photon loading [263, 264]. These experiments have inspired new directions for exploiting finite time delay effects of a single atom within the framework of waveguide QED.

In the realm of waveguide-QED, theoretical work has predicted that a time-delayed coherent feedback can significantly alter the characteristics of resonance fluorescence by introducing new resonances and changing the photon output statistics [38, 43, 167, 190, 265]. In contrast to measurement-based feedback [152, 155, 266], *coherent feedback* is included at the system level to avoid measurements (and the resulting wavefunction collapse), and thus one can preserve the coherence of the system dynamics, a key resource in quantum technology applications. Furthermore, a finite time delay is also included with the feedback, so that the system output returns after a non-trivial delay time, which introduces non-Markovian (i.e., non-instantaneous, retardation) dynamics to the system evolution [17, 36, 41, 42, 46, 48, 161, 168, 172, 185, 190, 191, 203, 267–271]. This is a challenging dynamic to simulate because conventional model approaches, such as the master equations, use a Markov approximation which fails in the presence of a time-delayed coherent feedback [32, 272]. Here, we use a quantum trajectory discretized waveguide (QTDW) method which includes the feedback at the system level to be able to describe the non-Markovian system with Markovian equations [46, 173, 190, 271].

In this work, we use a superconducting circuit and transmon artificial atom platform (treated as a two level qubit) to implement a coherent feedback loop with a delay time on

the order of the qubit's radiative lifetime. By controlling the qubit and pump frequencies, the reflection coefficient is recorded to characterize the qubit and feedback loop. We also show the experimental and simulated fluorescence spectrum as a function of pump power at two contrasting round trip phase changes, which quantitatively agree. These results highlight a new quantum optics regime where a time-delayed feedback changes the well-known Mollow triplet, and we show simulation results which highlight that this regime shows a pronounced non-Markovian response.

These feedback effects go to the root of time-delayed non-instantaneous coupling which can produce new and exotic quantum optical states. For example, the time delay can be strategically chosen for the returning field to interfere (constructively or destructively) with the qubit emission during an excitation protocol, with applications to improving performance of single photon sources [271] or generating new resonances [190]. Also, the time delay can be lengthened to be longer than an individual pulse to interfere with the qubit output between sequential excitations such as in cluster state generation protocols [17]. Here, the time delay is on the order of the qubit lifetime and sets up nodes where the Mollow triplet sidepeaks are suppressed and can introduce new resonances through *dressing* of the Fabry-Pérot modes beyond the three peaks of the Mollow triplet.

4.1 Time-Delayed Coherent Feedback System

4.1.1 Theoretical Model

As illustrated in Fig. 4.1(a), a transmon qubit couples bidirectionally to the waveguide with a total relaxation rate of Γ in an open transmission line and a resonance frequency of ω_0. The presence of a mirror at the end of the waveguide allows the propagating fields (microwaves) to interact with the qubit after each round trip with a delay of $\tau = L_0/c(\omega_0)$, where L_0 is the round trip length of the feedback loop and $c(\omega_0)$ is the group velocity of the waveguide mode with reference frequency ω_0 [37]. The feedback loop also introduces a round trip phase change $\phi = \phi_{\mathrm{M}} + \omega_0\tau$, where ϕ_{M} is the mirror phase change, in this case $\phi_{\mathrm{M}} = \pi$ and we calculate ϕ relative to the antinode when $\omega_0/2\pi = 4.9$ GHz.

The qubit is excited by a continuous-wave (CW) field through the waveguide, with Rabi frequency Ω_0 and frequency ω_{p}. Since the pump is introduced through the waveguide, it will set up a standing wave due to its reflection off the mirror, leading to an effective Rabi frequency of $\Omega_{\mathrm{eff}} = \Omega_0(1 + e^{i\phi_{\mathrm{p}}})$ with $\phi_{\mathrm{p}} = \phi_{\mathrm{M}} + \omega_{\mathrm{p}}\tau$. In particular, when $\phi_{\mathrm{p}} = 0$ (π), the qubit is located at an antinode (node) of the pump's electromagnetic field. We

also include pure dephasing effects in the qubit with rate γ', an important dissipation channels to include in order to compare simulated observables with real experiments, and a phenomenological radiative loss term with rate γ_{L} dependent on ϕ (for example with $\gamma_{\mathrm{L}} \approx 0$ when $\phi = 0$ and $\gamma_{\mathrm{L}} = 0.075\Gamma$ when $\phi = -0.632\pi$).

The main Hamiltonian and QTDW model used to simulate the qubit and feedback system is presented in the Supplementary Material. In the following results, the complex reflection coefficient is calculated following a novel extension of the QTDW model. Typically, the waveguide field entering the feedback loop is assumed to be vacuum, but we now relax this assumption and introduce waveguide bins which enter as a superposition between the vacuum state and the single photon state. This is valid when the total flux present in the loop is less than the truncation of the number of photons in the feedback loop, $\Omega_0\tau < 2$, which is the case when dealing with results in the relatively weak pumping regime.

There are two restrictions to this approach; there must be a negligible probability for two photons to enter the system at once, $\Omega_0 dt \ll 1$ (where dt is the bin width in the QTDW model), and, more stringently, the total flux present in the loop be less than the truncation of the number of photons in the feedback loop, $\Omega_0\tau < 2$ for a maximum of two photons in the feedback loop.

4.1.2 Experimental Methods

Figure 4.1(b) shows an optical image of our device, a superconducting transmon qubit [273] strongly coupled to a one dimensional (1D) open transmission line [117, 259] with characteristic impedance $Z_0 \approx 50\ \Omega$. This system acts as a near perfect waveguide creating an excellent platform to study waveguide-QED experiments. A unique property of these qubits is the ability to control the transition energy determined by

$$\hbar\omega_0(\Phi_{\mathrm{ext}}) \approx \sqrt{8E_J(\Phi_{\mathrm{ext}})E_C} - E_C, \tag{4.1}$$

where E_C is the charging energy, a constant given by $E_C = e^2/2C_\Sigma$, where C_Σ is the total capacitance of the qubit. The Josephson energy, $E_J(\Phi_{\mathrm{ext}})$, is determined by $E_J(\Phi_{\mathrm{ext}}) = E_{J,0}|\cos(\pi\Phi_{\mathrm{ext}}/\Phi_0)|$ where Φ_{ext} is the applied external magnetic flux, which can be controlled by the current, I, and $\Phi_0 = h/(2e)$ is the flux quantum. In this experiment, the characterization of the qubit is shown in Fig. 4.6 and the extracted parameters are given in Table 4.1 (the extraction technique can be found in Refs. [262, 274]), which introduces an anharmonicity allowing the qubit to be treated as a TLS with ground state $|0\rangle$ and first excited state $|1\rangle$.

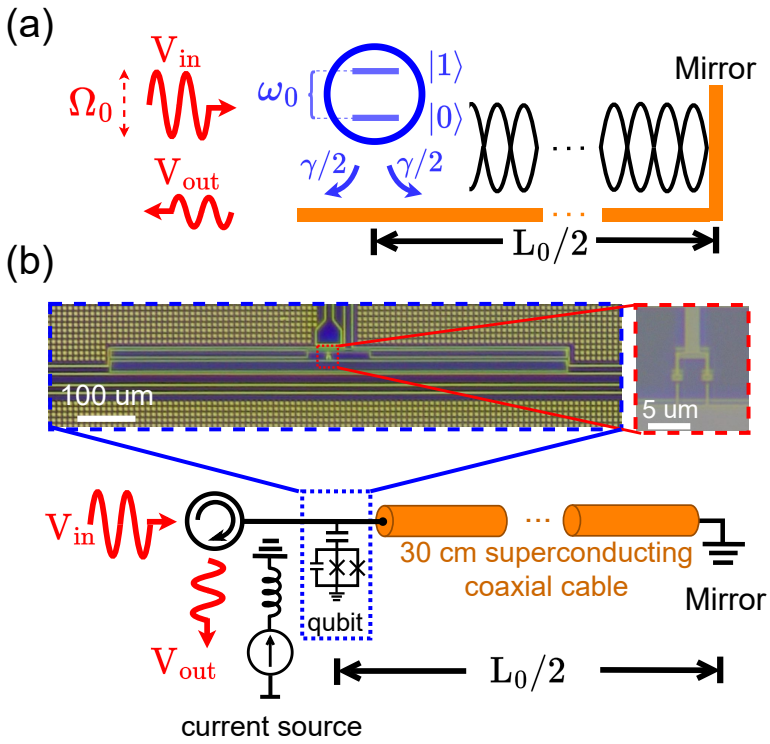

Figure 4.1: (a) Schematic of the qubit-mirror in a quasi-1D system. The round trip length is L_0 and the qubit couples to the waveguide symmetrically with total relaxation rate Γ. The qubit is pumped with frequency (ω_p) and Rabi frequency (Ω_0) directly through the waveguide. (b) Optical microscope images of the transmon qubit and the experimental setup. The blue dashed rectangle shows the qubit capacitively coupled to a 1D transmission line and the red dashed square shows the superconducting quantum interference device (SQUID) with a tunable frequency through the applied external magnetic flux. One end of the transmission line couples to the feedback loop terminated by a connection to the grounding plane that acts as the mirror, and the material of the superconducting coaxial cable is NbTi. The other end connects to a three port circulator through which the input signal enters the waveguide and the output signal is detected. The details of the setup can be found in Fig. 4.5 in the Supplementary Material.

In order to access the non-Markovian regime with time-delayed feedback, we need a time delay between the qubit and mirror on the order of the qubit lifetime ($1/\Gamma$). To achieve this, the transmission line is connected to a superconducting coaxial cable which is truncated by connecting the center conductor to the grounding plane with a shorted terminator, contributing the mirror phase change: $\phi_M = \pi$. This superconducting cable has $L_0/2 \approx 0.3$ m, corresponding to a round trip delay time of $\tau = 3.63$ ns. The characterization

method is shown in the Supplementary Material. Although the qubit-mirror distance is fixed, we can change the round trip phase change, ϕ, by controlling ω_0 and corresponding effective wavelength. This allows the qubit to be tuned to the node or antinode of the waveguide field, i.e., a round trip phase change that varies from π to 0. Further details of the experimental setup are available in the Supplementary Material.

4.2 Elastic Scattering of an Incident Microwave Field - Linear Regime

Before studying the nonlinear regime of the resonance fluorescence, we investigate the elastic scattering of the system with a weak pump ($\Omega_0 \ll \gamma_\mathrm{d}$, where γ_d is the decoherence rate, which approximately reflects the loss of quantum coherence from both energy relaxation and pure dephasing), to characterize the qubit response in the linear regime. This is done using a Vector Network Analyzer (VNA) to send the input voltage, V_in, with a frequency around ω_0, sent in through the waveguide and the outgoing voltage, V_out, measured to retrieve the reflection coefficient $r = \langle V_\mathrm{out}\rangle/\langle V_\mathrm{in}\rangle$. By controlling the external magnetic flux, Φ_ext, via applying current, I, the qubit frequency is swept from 4.75 GHz $< \omega_0/2\pi <$ 5.08 GHz (equivalent to a range of $-1.16\pi < \phi < 1.24\pi$) and the pump frequency is swept from 4.75 GHz $< \omega_\mathrm{p}/2\pi <$ 5.15 GHz. This maps out a parameter space containing the 18th and 19th nodes of the standing waveguide mode.

Figures 4.2(a)–(d) show the measured and simulated reflection coefficients as functions of the pump frequency, ω_p, and the round trip phase change, ϕ. The offset from the resonance condition between the pump and qubit (black line) is caused by a feedback induced shift from ω_0 to $\widetilde{\omega}_0$ [35, 276]. The qubit will be aligned with a node in the standing waveguide mode when $\omega_0/2\pi = 4.772$ GHz or 5.047 GHz corresponding to $\phi = -\pi$ or π, respectively.

At $\phi = 0$, when the qubit is at the antinode of the standing waveguide mode, indicated by the red arrow in Figs. 4.2(a)-(d), the interaction between the qubit and feedback results in enhanced spontaneous emission. At this point, the reflection spectroscopy is dominated by coherent scattering (elastic scattering), so the qubit fully reflects the resonant pump field without sending energy into the feedback loop, giving $|r| \approx 1$, but the phase is flipped indicating the scattering from the qubit. Perfect reflection also occurs when $\phi = \pm\pi$, but without a phase change. This is because the qubit is now at a node of the standing wave and is invisible to the incoming pump field. Thus, no scattering from the qubit occurs, indicating that the qubit is completely transparent to the waveguide field and perfect

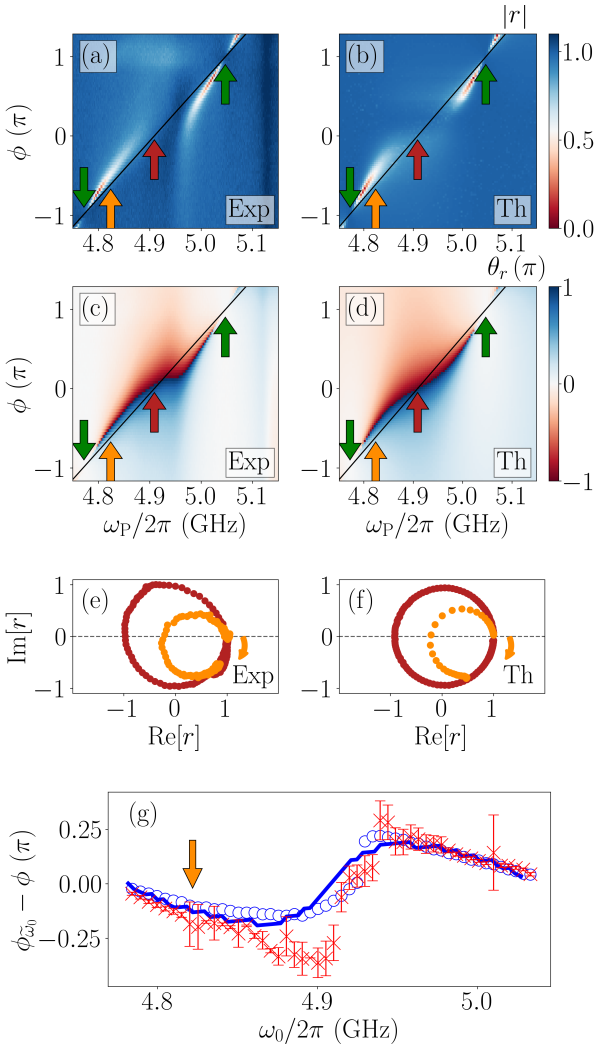

Figure 4.2: Single-tone spectroscopic measurement of the reflection coefficient r as a function of ϕ and ω_p using a weak pump ($\Omega_0 \ll \gamma_\mathrm{d}$). (a) and (b) show the magnitude response, $|r|$, and (c) and (d) show the phase response, θ_r, of the experimental and simulated r respectively (the full spectroscopy is shown in Fig. 4.6 of the Supplementary Material). The node and antinode frequencies of the pump field are indicated by the green and red arrows respectively. The solid black line in these graphs indicate the expected qubit bare resonance frequency ω_0 without coupling to the continuous photonic mode, calculated by the extracted anharmonicity and maximum qubit frequency. (e) and (f) respectively show experimental and simulated line cuts from (a)-(d) of r in the complex plane for fixed ω_0 indicated by the red ($\omega_0/2\pi = 4.9$ GHz, $\phi = 0$) and orange ($\omega_0/2\pi = 4.822$ GHz, $\phi = -0.632\pi$) arrows. The orange arrows show the tilted angle of the complex plane. (g) shows $(\widetilde{\omega}_0 - \omega_0)\tau$ of the experimental (blue data points) and simulated (blue solid curve) as the tilted angle $\phi_{\widetilde{\omega}_0} - \phi$, and directly extracted tilted angle from the complex plane (red crosses data points) versus ω_0. The orange arrow points out the corresponding $\phi_{\widetilde{\omega}_0} - \phi$ of the orange complex plane in (e) and (f). The disagreement between data and theory around 4.9 GHz is likely due to the qubit coupling to a stray resonance [275].

reflection from the mirror occurs.

Between $\phi = 0$ and $\phi = \pm\pi$ when the probing frequency is on resonance, incoherent scattering (i.e., from phase jumps due to pure dephasing) by the qubit produces a dip in the reflected field when $\omega_p \approx \widetilde{\omega}_0$. As ϕ changes from 0 to $\pm\pi$, the feedback modified effective relaxation rate, $\widetilde{\Gamma}$, will change from its maximum to 0 because the qubit is effectively moving from an antinode to a node of the standing wave of the waveguide mode. When $\widetilde{\Gamma}$ is close to $\gamma_L/2 + \gamma'$, part of the incident photons will be scattered incoherently through pure dephasing or intrinsic loss, which means $|r|$ can drop to 0 [277]. Then finally, the dip becomes narrower and eventually disappears, with no phase change, because the qubit sits at a node and is not pumped by the standing wave mode when ϕ_p approaches $\pm\pi$.

Although our system is in the non-Markovian regime, we can still use the experimental response in Figs. 4.2(e) to extract information for $\widetilde{\Gamma}$ and γ_d by the circle fit technique [278]. The corresponding fitting function is

$$r(\omega_p) = 1 - \frac{i\widetilde{\Gamma}(\omega_p)}{\Delta + i\gamma_d(\omega_p)}, \tag{4.2}$$

where $\Delta = \omega_p - \widetilde{\omega}_0$. Figures 4.2(e) and (f) show the reflection coefficient in the complex plane as the pump field frequency changes for $\widetilde{\omega}_{\phi=0}/2\pi = 4.9$ GHz and $\widetilde{\omega}_{\phi=-0.632\pi}/2\pi = 4.806$ GHz, respectively corresponding to $\phi = 0$ (red circle) and $\phi = -0.632\pi$ (orange circle). We compared the complex plane of the reflection coefficient with the experimental data, and demonstrate an excellent fit.

For $\phi = 0$, in Fig. 4.2(e), the extracted parameters from the qubit's reflection response are in Table 4.2. Since the qubit is at an antinode, $\widetilde{\Gamma}_{\phi=0} \approx 2\Gamma$, or double the relaxation rate of the qubit in an open waveguide [37, 167, 185]. The product $\Gamma\tau = 1.097$ tells us the feedback is operating in the non-Markovian regime as the delay time and qubit lifetime are similar. Because $\widetilde{\Gamma}_{\phi=0}$ is larger than the other dissipation channels, elastic scattering dominates and the radius of the circle in the complex plane ($|r|$) is ≈ 1. When $\phi = -0.632\pi$, $\widetilde{\Gamma}_{\phi=-0.632\pi}$ is much closer to $\gamma_L/2 + \gamma'$ and the dip in the reflection coefficient occurs leading to a smaller radius of the circle. Additionally we observe a feedback induced frequency shift of 16 MHz ($\omega_0 = 4.822$ GHz and $\widetilde{\omega}_0 = 4.806$ GHz).

A subtle but interesting non-Markovian effect appears here even in the linear regime. From Eq. (4.2) one expects a symmetric Lorentzian in $|r|$, however in the non-Markovian regime an asymmetry appears which tilts the circle in the complex plane shown in Figs. 4.2(e) and (f). The angle of this tilt is $(\widetilde{\omega}_0 - \omega_0)\tau$ and arises because of the feedback induced shift to the qubit frequency. In the Markovian regime ($\tau \sim 0$), all frequencies see a single round

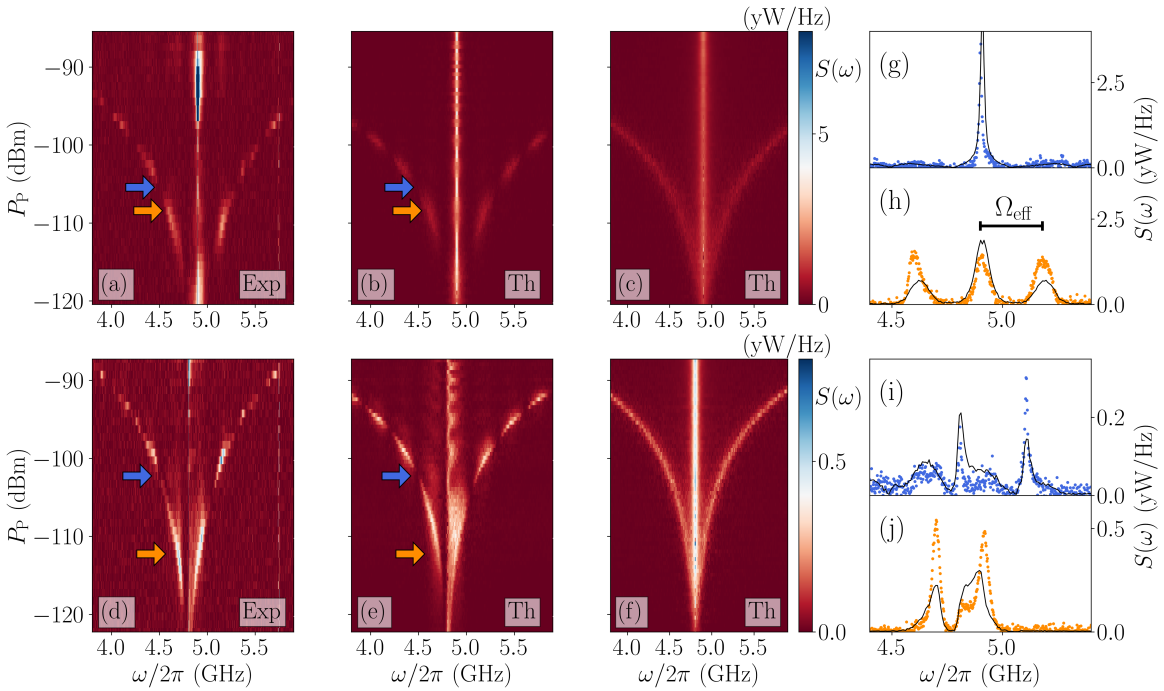

Figure 4.3: Resonant fluorescence emission spectra of the qubit as a function of the pump power, P_p and the detected radiation ω, with $\omega_\mathrm{p} = \widetilde{\omega}_0$. For (a)-(c) $\phi = 0$ and (d)-(f) $\phi = -0.632\pi$. In (a) and (d) the experimental results are shown while in (b) and (e) we show the corresponding simulated results. For comparison, the simulated spectral response with a Markovian feedback loop is shown in (c) and (f). Under the strong pump, the qubit energy level split is Ω_eff, creating three transitions frequency, $\widetilde{\omega}_0 \pm \Omega_\mathrm{eff}$ and $\widetilde{\omega}_0$. In (g)-(j) we show individual spectra with the experimental data as colored dots and the simulated response as a solid curve. For $\phi = 0$, in (g) $P_\mathrm{p} = -105.4$ dBm and in (h) $P_\mathrm{p} = -108.4$ dBm. For $\phi = -0.632\pi$, in (i) $P_\mathrm{p} = -102.3$ dBm and in (j) $P_\mathrm{p} = -112.3$ dBm. The QTDW simulation results use 1000 trajectories per spectrum in (b), (c), (e), and (f) and 10,000 trajectories per simulated spectra in (g)-(j). [279]

trip phase change, ϕ, while in the non-Markovian regime the round trip phase change for a frequency ω' is $\phi_{\omega'} = \omega'\tau + \phi_\mathrm{M} = (\omega' - \omega_0)\tau + \phi$ where the second equivalency we get by writing ϕ_M in terms of ϕ. Due to the feedback induced change in the qubit frequency, the round trip phase change that is seen by the qubit emission is $\phi_{\widetilde{\omega}_0} = (\widetilde{\omega}_0 - \omega_0)\tau + \phi$. This readily shows the non-Markovian tilt that is introduced is equivalent to $\phi_{\widetilde{\omega}_0} - \phi$, as shown in Fig. 4.2(g), the difference between the round trip phase change of the qubit emission in the non-Markovian and Markovian regimes.

4.3 Resonance Fluorescence Response - Non-linear Regime

When the qubit is pumped by the resonant microwave ($\Delta = 0$), its state evolves at an effective Rabi frequency Ω_{eff}. When the Rabi frequency of the pumping field is much larger than the natural linewidth of the qubit ($\Omega_{\text{eff}} \gg \gamma_{\text{d}}$), the system response includes non-linear dynamics beyond the interference effects of the linear response. In this regime (i.e., without feedback), the energy levels of the qubit become dressed, creating three transition frequencies that appear as distinct spectral components known as the Mollow triplet [106]. These frequencies are $\widetilde{\omega}_0$ and $\widetilde{\omega}_0 \pm \Omega_{\text{eff}}$. To investigate the effect of feedback on the spectral response of the system, the spectra were recorded as a function of pump power, P_{p}, by applying the pumping field from a radio frequency (RF) source, resonant with the qubit, to the sample with an effective attenuation, A, and sampling the amplified output signal with a spectral analyzer (SA) and normalized to the system gain, G. The extracted values are shown in Table 4.2 in the Supplementary Material.

Figure 4.3 shows the spectral response at two different phase values, with $\phi = 0$ in Figs. 4.3(a)-(c) and $\phi = -0.632\pi$ in Figs. 4.3(d)-(f). Figures 4.3(c) and (f) show the simulated response with Markovian feedback. In this regime, the feedback is reduced to two phase changes, ϕ and ϕ_{p}, which change the effective relaxation rate from the qubit and the effective Rabi frequency respectively. Then, in this regime, as the pump power increases the two sidebands will move further from the central peak following $\widetilde{\omega}_0 \pm \Omega_{\text{eff}}$. Qualitatively, this is the same behavior as the response from a qubit pumped without feedback.

When the feedback is included with a time delay on the order of the qubit lifetime, non-Markovian dynamics appear from the interference between the returning feedback and the qubit output which make qualitative changes to the spectral response. We observed these changes experimentally in Figs. 4.3(a) and (d) which match our simulations in Figs. 4.3(b) and (e), with example slices of the experimentally observed spectra in Figs. 4.3(g)-(j). For $\phi = 0$ with $\omega_0/2\pi = 4.9$ GHz, Figs. 4.3(a) and (b), the presence of the Mollow triplet oscillates as the pump power, P_{p}, increases.

In contrast to the Markovian regime, where the sidepeaks existed continuously, the macroscopic delay time introduces nodes where the sidepeaks are not observed. These nodes occur when the round trip phase change at that frequency results in destructive interference; $\phi_{\text{node}} = (2k-1)\pi$, for $k \in \mathbb{Z}$. This can be written with respect to a phase

change that is known, ϕ_{p}, to get

$$\omega_{\mathrm{node}} = \frac{(2k-1)\pi - \phi_{\mathrm{p}}}{\tau} + \omega_{\mathrm{p}}, \tag{4.3}$$

which gives the condition for the nodes seen in Figs. 4.3(a), (b), (d), and (e). This interference condition is symmetric about the central peak when $\phi = 0$ and the pump is on resonance which is seen in the nodes of the red and blue sidebands of the observed spectrum in Figs. 4.3(a) and (b). In Figs. 4.3(g) and (h), we obtained excellent agreement between experiment and theory for specific pump powers of $P_{\mathrm{p}} = -105.4$ dBm and $P_{\mathrm{p}} = -108.4$ dBm.

Next, we tuned $\widetilde{\omega}_0/2\pi = 4.806$ GHz and $\phi = -0.632\pi$ in Figs. 4.3(d) and (e). We excite the qubit at the effective resonance, $\Delta = 0$, with $\phi_{\mathrm{p}} = -3/4\pi$, due to the difference of 16 MHz between the bare and effective resonance frequency. In this case, $\widetilde{\Gamma}$ is suppressed and the width of the central peak becomes narrower. Moreover, the node structure of the sideband transitions remains when the destructive interference condition is met. However, the red and blue shifted sidebands are suppressed asymmetrically due to the non-zero ϕ. Again we show spectra at specific pump powers, $P_{\mathrm{p}} = -102.3$ dBm in Fig. 4.3(i) and $P_{\mathrm{p}} = -112.3$ dBm in Fig. 4.3(j).

Additionally, due to the longer qubit lifetime when $\phi = -0.632\pi$ we can see higher order non-linear dynamics beginning to appear in the spectra. When the feedback is macroscopic, the dressed states of the qubit in the presence of the pumping field are further dressed by the Fabry-Pérot resonances set up by the feedback loop. These Fabry-Pérot resonances, which coincide with the antinode frequencies, occur when the round trip phase change at that frequency results in constructive interference; $\phi_{\mathrm{antinode}} = 2\pi k$ [190] for $k \in \mathbb{Z}$. Similar to the nodes, the antinode frequencies can be written as

$$\omega_{\mathrm{antinode}} = \frac{2\pi k - \phi_{\mathrm{p}}}{\tau} + \omega_{\mathrm{p}}. \tag{4.4}$$

This results in multiple new resonances appearing in the spectrum for any $\omega_{\mathrm{antinode}}$ between the Mollow sidebands. These are seen in the simulated spectrum of Fig. 4.3(e) and we can begin to see these appearing in the experimental spectrum shown in Fig. 4.3(i) at a pump power of $P_{\mathrm{p}} = -102.3$ dBm. These results are intrinsic to the feedback system and independent of the specific pumping scheme employed [190].

4.4 Conclusions

We have characterized the superconducting qubit and feedback loop with the waveguide QED system in the linear regime by measuring the reflection coefficient in the presence of a weak pump field. The change in the qubit's frequency and radiative linewidth, as well as the tilt of the reflection coefficient response in the complex plane, are non-Markovian signatures caused by interference with the qubit's own radiation. We then demonstrated the spectrum in the non-linear regime, revealing the Mollow triplet under time-delayed coherent feedback. The distinctive disappearance of the side peaks in resonance fluorescence shows excellent agreement with our QTDW model, suggesting that their formation results from the constructive and destructive interference of emissions with the time-delayed coherent feedback.

Our work indicates that the atom-mirror system of a superconducting qubit could serve as the simplest platform for engineering a non-Markovian reservoir. Our results offer a direct approach to accessing the strong coupling regime for the exploration of exotic physics, including long distance collective dipole coupling [59, 218], photon correlations [190] and excitation trapping [46]. Additionally there are promising applications for quantum technologies such as improving on-demand single photon sources [271], long distance quantum processing [280] and generating two-dimensional photonic cluster states [17].

4.5 Acknowledgements

I.-C. H. acknowledges financial support from City University of Hong Kong through the start-up project 9610569, from the Research Grants Council of Hong Kong (Grant number 11312322), and from the Guangdong Provincial Quantum Science Strategic Initiative (Grant No. GDZX2203001, GDZX2303005, GDZX2403001). This work is supported by the Natural Sciences and Engineering Research of Canada, the National Research Council of Canada, the Canadian Foundation for Innovation, and Queen's University, Canada. S.H. and G.C. acknowledge RIKEN for support. F.N. is supported in part by the Japan Science and Technology Agency (JST) [via the CREST Quantum Frontiers program Grant No. JPMJCR24I2, the Quantum Leap Flagship Program (Q-LEAP), and the Moonshot R&D Grant Number JPMJMS2061].

4.6 Supplementary Material for "Resonance fluorescence of an artificial atom with a time-delayed coherent feedback"

4.6.1 Full Hamiltonian and Quantum Trajectory Discretized Waveguide (QTDW) Model

The total Hamiltonian (in natural units, $\hbar = 1$) is split into four terms $H = H_0 + H_{\text{pump}} + H_{\text{W}} + H_{\text{I}}$: the qubit, pump, waveguide, and interaction Hamiltonians respectively. Using the rotating wave approximation, these Hamiltonians, in the continuous frequency domain for the waveguide modes and in the interaction picture at ω_{p}, are given by

$$\begin{aligned} H_0 + H_{\text{pump}} &= \delta\sigma^+\sigma^- + \frac{\Omega_{\text{eff}}}{2}(\sigma^+ + \sigma^-), \\ H_{\text{W}} &= \int_{-\infty}^{\infty} d\omega\,(\omega - \omega_{\text{p}})\, b^\dagger(\omega) b(\omega), \\ H_{\text{I}} &= \int_{-\infty}^{\infty} d\omega \left[\left(\sqrt{\frac{\Gamma}{4\pi}}\sigma^+ b(\omega) + \sqrt{\frac{\Gamma}{4\pi}} e^{i(\phi_M + \omega\tau)} \sigma^+ b(\omega) \right) + \text{H.c.} \right], \end{aligned} \tag{4.5}$$

where $\delta = \omega_0 - \omega_{\text{p}}$ is the detuning between qubit and pump, σ^+ (σ^-) is the raising (lowering) Pauli operator, and $b^\dagger(\omega)$ ($b(\omega)$) is the raising (lowering) operator for the modes in the waveguide. Pure dephasing and the additional phenomenological (radiative) loss are included as quantum jump operators, $C_0 = \sqrt{\gamma'}\sigma^+\sigma^-$ and $C_1 = \sqrt{\gamma_{\text{L}}}\sigma^-$, following standard quantum trajectory formalism [176–178, 281, 282].

This is simulated following a quantum trajectory discretized waveguide (QTDW) technique [173, 190, 271], which involves modeling the feedback loop spatial section at the system level (i.e. evolving the section coherently along with the qubit states in the system ket vector rather than as a Markovian bath) by transforming the $b(\omega)$ operators into the discrete time operators B_n. These operators represent a slice of the waveguide field in the feedback loop which begins and ends at the qubit. Each slice has a width of $\Delta t = \tau/N$ where N is the desired number of spatial increments to discretize the time domain waveguide fields. This transformation leaves H_0 and H_{pump} unchanged, while H_{I} becomes

$$H_{\text{I}} = \left(\sqrt{\frac{\Gamma}{2\Delta t}}\sigma^+ B_{N-1} + e^{i\phi}\sqrt{\frac{\Gamma}{2\Delta t}}\sigma^+ B_0 \right) + \text{H.c.}\ . \tag{4.6}$$

Additionally, the evolution of the B_n operators under the waveguide Hamiltonian is

$$U_{\mathrm{W}}^{\dagger}(\Delta t) B_n U_{\mathrm{W}}(\Delta t) = \exp\left[-i\delta\Delta t\right] B_{n-1}, \tag{4.7}$$

where $U_{\mathrm{W}}(\Delta t) = \exp\left[-iH_{\mathrm{W}}\Delta t\right]$ and we assume linear dispersion. This represents the waveguide bin moving forward around the feedback loop every time step. This is schematically shown in Fig. 4.4. Before the final bin 0 leaves the feedback section of the waveguide we perform a simulated measurement of the field in the bin. For the system at time t, the ket vector can be represented as

$$|\psi(t)\rangle = |\psi_0(t)\rangle\,|0\rangle_0 + |\psi_1(t)\rangle\,|1\rangle_0\,, \tag{4.8}$$

where $|1\rangle_0$ ($|0\rangle_0$) represents a photon (vacuum) in the final waveguide bin. Then through the simulated measurement, we project the system into the state $|\psi_0(t)\rangle$ or $|\psi_1(t)\rangle$ with respective probabilities $\langle\psi_0(t)|\psi_0(t)\rangle$ and $\langle\psi_1(t)|\psi_1(t)\rangle$. This allows the information from the bin to be discarded as it leaves the system, and avoids a continuously growing Hilbert space. Note that this process is not norm conserving and the ket vector must be renormalized each step.

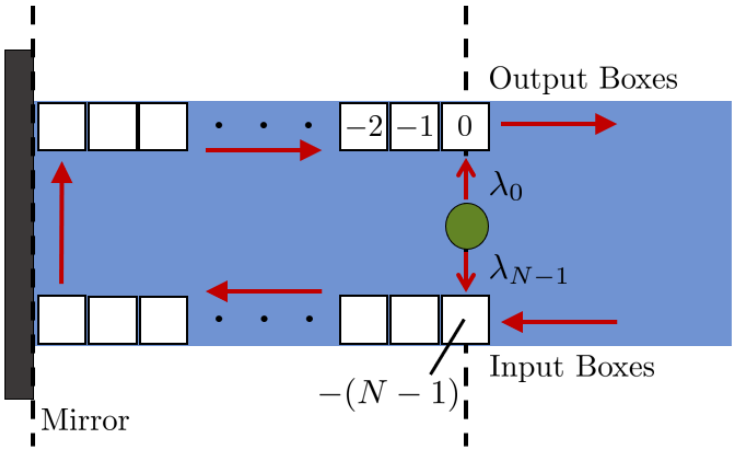

Figure 4.4: Schematic of the quantum trajectory discretized waveguide model with the waveguide field represented by discrete spatial bins. In this setup, the qubit couples to the incoming bin $N-1$, represented by operator B_{N-1}, with coupling constant $\lambda_{N-1} = \sqrt{\Gamma/2\Delta t}$ and it couples to the outgoing bin 0, represented by operator B_0, with coupling constant $\lambda_0 = e^{i\phi}\sqrt{\Gamma/2\Delta t}$.

Extending the QTDW model, we can also calculate the complex reflection coefficient,

$$r = \langle V_{\mathrm{out}}\rangle \,/\, \langle V_{\mathrm{in}}\rangle\,, \tag{4.9}$$

for the system where V_{out} is the outgoing electric field and V_{in} is the incoming driving electric field. To do this, we must send in a waveguide field which is not the vacuum. For an incoming field with Rabi frequency Ω_0, the photon flux in the waveguide is $\Omega_0 dt$ and the incoming waveguide bin is treated as a superposition of the vacuum state and a single photon state

$$|\psi'\rangle = \sqrt{1-\Omega_0 dt}\,|0\rangle_{N-1} + \sqrt{\Omega_0 dt}\,|1\rangle_{N-1}\,, \tag{4.10}$$

where $|1\rangle_{N-1}$ ($|0\rangle_{N-1}$) represents a photon (vacuum) in the first waveguide bin. This is expected to be valid when (i) there is a negligible probability for two photons to enter the waveguide section at the same time, $\Omega_0 dt \ll 1$, and, more stringently, (ii) the total flux present in the loop is less than the truncation of the number of photons in the feedback loop, $\Omega_0 \tau < 2$, for a maximum of two photons in the feedback loop.

The incoming bin is entangled with the current state of the system before beginning the next time step. Then the reflection coefficient is given by

$$r = \frac{e^{i\delta\tau}\,\langle B_0\rangle_{\text{ss}}}{\Omega_0 dt}, \tag{4.11}$$

where $\langle B_0\rangle_{\text{ss}}$ is the expectation of the final waveguide bin in the steady state.

The incoherent spectra presented in Fig. 4.3 are calculated from

$$S^{\text{out}}_{\text{incoh}}(\omega) = \int_0^\infty dt_2 e^{i(\omega-\omega_{\text{p}})t_2}\left[\langle B_0^\dagger(t_2)B_0(0)\rangle_{\text{ss}} - \langle B_0^\dagger(0)\rangle_{\text{ss}}\langle B_0(0)\rangle_{\text{ss}}\right]. \tag{4.12}$$

The two quantities $\langle B_0^\dagger(0)\rangle_{\text{ss}}$ and $\langle B_0(0)\rangle_{\text{ss}}$ are steady-state expectation values which are readily calculated following standard quantum trajectory techniques. On the other hand, $\langle B_0^\dagger(t_2)B_0(0)\rangle_{\text{ss}}$ is the unnormalized first-order auto-correlation function, which is not a standard calculation in quantum trajectory theory. We follow the technique described in [190] to calculate this observable using a "leader" and "follower" trajectory, which are simulated after the steady state has been reached in a standard trajectory simulation.

4.6.2 Experimental Setup

The schematics of the experimental setup is shown in Fig. 4.5 (a), the input coaxial line contains the attenuators (depicted as red rectangles), which are strategically thermalized along the input coaxial lines at each fridge stage to reduce Johnson thermal noise from the room temperature environment. The output reflected signal from the device is passed

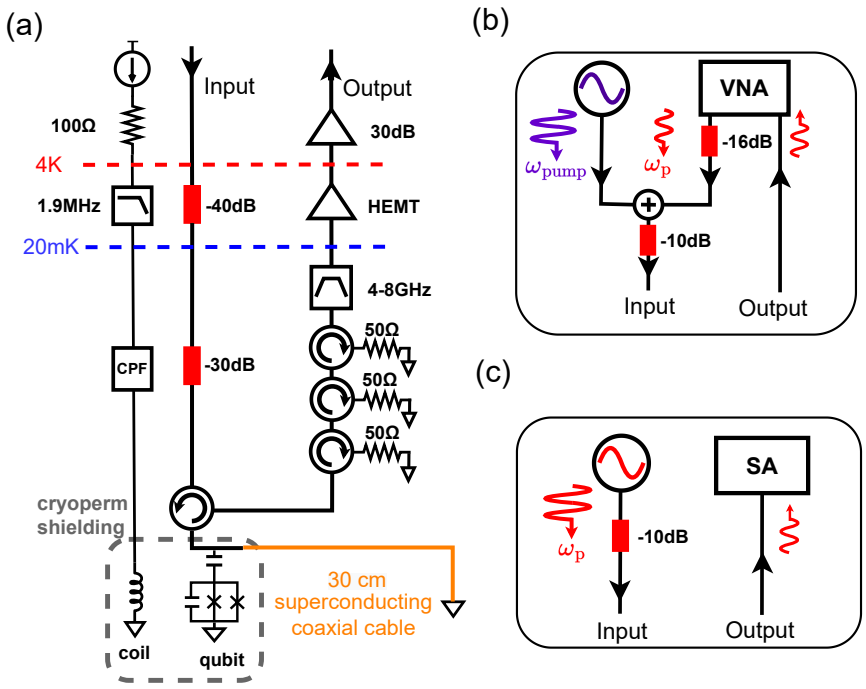

Figure 4.5: Schematics of the full experimental measurement setup (a) The device and the superconducting coaxial cable are placed at the bottom of the dilution refrigerator operating at the base temperature 20 mK (below the blue dashed line). (b) and (c) are the measurement setups at room temperature. (b) to measure the elastic emission, we measured the two-tone spectroscopy to extract E_C [262, 274], when the pump is on, and (c) for measuring the inelastic emission.

through several cryogenic circulators in series, a band-pass filter (BPF), a high-electron-mobility transistor (HEMT) at the 4 K stage, and amplifiers at room temperature. We send a current, I, with the direct-current (DC) source from room temperature to a small superconducting magnet close to the device for flux controlling the transition frequency of the transmon qubit. The "30 cm superconducting coaxial cable" and the device were thermalized at the 20 mK stage. The device was inside a single layer of a cylindrical Cryoperm magnetic shield.

Figures 4.5 (b) and (c) show the measurement setup at room temperature. We measure the elastic scattering with the setup in Figure 4.5 (b). We send in the weak pump signal $\omega_{\rm p}$ with a vector network analyzer (VNA) and the strong pump signal $\omega_{\rm pump}$ from the radio-frequency (RF) source through the power combiner. We detect the output signal for measuring the reflection coefficient r. We measured the inelastic scattering with the setup

in Figure 4.5(c): a spectrum analyzer (SA) measured the absolute power emission from the device by strongly pumping it with the RF source.

4.6.3 Spectroscopy of the transmon qubit

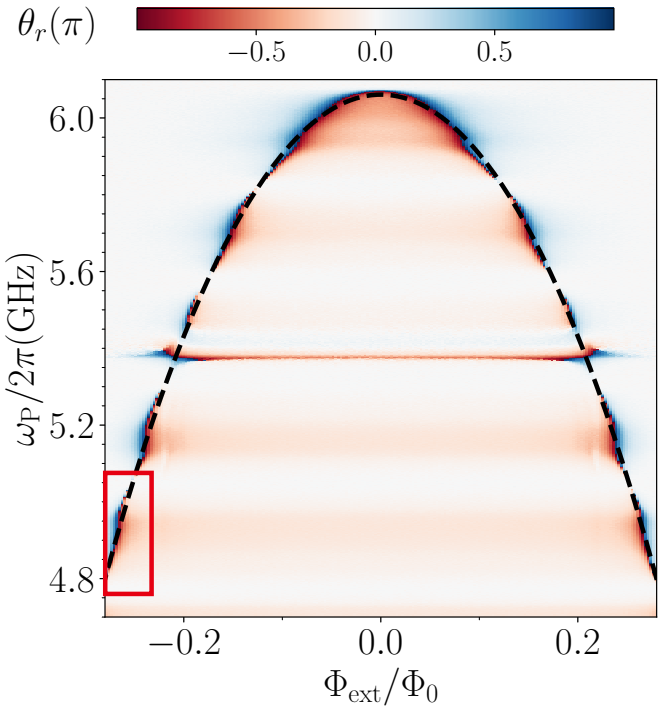

Figure 4.6: Single-tone spectroscopy of the transmon qubit. The phase of the reflection coefficient θ_r as a function of the pumping frequency ω_p and external flux Φ_{ext} for a weak pump ($\Omega_p \ll \gamma_d$). The black dashed curve is a fitted curve for ω_0 using Eq. (4.1) in the main text. Figure 4.2(c) is a zoom-in of the region highlighted by the red rectangle.

In Fig. 4.6, we show the single-tone spectroscopy to characterize the parameters of the transmon qubit, the reflection coefficient $|r|$ as a function of ω_p and external flux Φ_{ext}, showing the cosine pattern with the qubit's response as the external flux Φ_{ext} by applying a current, I. Given the long distance between the qubit and mirror, we can periodically tune the relaxation rate $\widetilde{\Gamma}$, as the qubit resonance frequency ω_0 is changing between the standing wave voltage of the antinode and node.

$\omega_{0,\max}/2\pi$	$E_{J,0}/h$	E_C/h	$\Gamma/2\pi$	τ	$\Gamma\tau$	$c(\omega_0)$
GHz	GHz	MHz	MHz	ns	-	m/s
6.06	24.5	200	48.1	3.63	1.097	1.81×10^8

Table 4.1: The extracted parameters of our qubit-mirror system. The qubit directly couples to the coplanar waveguide (CPW), with the maximum qubit frequency $\omega_{0,\max}$. $E_{J,0}$ and E_C are estimated by a fit of Eq. (4.1) in the main text and results are shown in Figure 4.6. With the superconducting cable connected, we extracted the relaxation rate, Γ in the open transmission line (without feedback) with the qubit at the antinode case and the delay time τ, as discussed in the delay time section from Fig. 4.2(a).

ϕ	$\omega_0/2\pi$	$\widetilde{\omega}_0/2\pi$	$\widetilde{\Gamma}/2\pi$	$\gamma_\mathrm{d}/2\pi$	A	G
π	GHz	GHz	MHz	MHz	dB	dB
0	4.9	4.9	96.2	50.08	-116.4	64.46

Table 4.2: Extracted parameters of the transmon qubit at the phase change $\phi = 0$. The nearest node frequency $\omega_\mathrm{node}/2\pi = 5.047$ GHz (4.772 GHz) has the effective round trip phase change $\phi = \pi$ $(-\pi)$. We extract the relaxation rate, $\widetilde{\omega}_0/2$, and the decoherence rate, γ_d, from the fitting results of the spectroscopy in Figs. 4.2(e) and (f). The extracted effective attenuation A (Fig 4.5(b) VNA setup) and the gain G, and the details of the technique is shown in [264].

4.6.4 Delay time

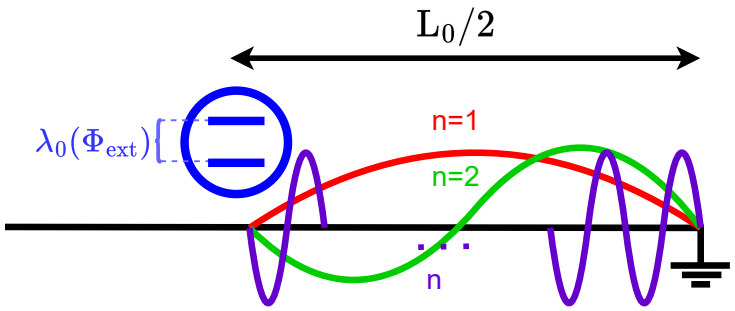

Figure 4.7: Schematic diagram of the node frequency condition. The red, green and purple curves show the mode structure of the voltage along the transmission line at the qubit frequency for $L_0/2 = \lambda_1/2$, $L_0/2 = \lambda_2$, and $L_0/2 = n\lambda_n/2$, where $n \in \mathbb{Z}$. We can apply Φ_ext to tune the qubit frequency ω_0, which makes the λ_n of the qubit sit on the different mode of the voltage node.

In this section, we discuss the method to extract the delay time, τ, with the node frequency, $\omega_n/2\pi$, of the standing wave between the qubit and the mirror, where $n \in \mathbb{Z}$, as shown in Fig. 4.7. The node frequency we observed is the result of the interference between the incoming wave and the wave reflected by the mirror. The condition to match the node structure is

$$\frac{n}{2}\lambda_n = \frac{v\tau}{2}, \tag{4.13}$$

where v is the group velocity and λ_n is the wavelength for node n. In the experiment, we effectively changed the λ_n of the qubit by controlling the qubit frequency, $\omega_0/2\pi$, through the external flux Φ_{ext}, as shown in Fig. 4.6.

Using the wave equation for node n, $2\pi v = \omega_n\lambda_n$, and combining it with Eq. (4.13) we obtain

$$n\lambda_n = \omega_n\lambda_n\tau/2\pi. \tag{4.14}$$

To remove the integer n, we can take the difference between the frequency at nodes n and $n+1$ to obtain

$$(\omega_{n+1} - \omega_n)\tau/2\pi = 1. \tag{4.15}$$

Thus, we can obtain the delay time in terms of the frequencies that we detect the nodes in the experiment,

$$\tau = \frac{2\pi}{\omega_{n+1} - \omega_n}. \tag{4.16}$$

Chapter 5

Improving On-Demand Single Photon Source Coherence and Indistinguishability Through a Time-Delayed Coherent Feedback

This work is published as: G. Crowder, L. Ramunno, and S. Hughes, "Improving on-demand single-photon-source coherence and indistinguishability through a time-delayed coherent feedback", Phys. Rev. A **110**, L031703 (2024) [271] and is reproduced here, in a consistent style for the thesis. Here, we use the quantum trajectory discretized waveguide (QTDW) model to investigate how coherent feedback can be used to improve the performance of a single photon source. The source is modelled as a two level system coupled to a coherent feedback loop with two additional dissipation channels, out of plane emission and pure dephasing, to simulate a realistic source. To generate on-demand photons, the two level system is driven by a pulsed laser source, which means to calculate the coherence and indistinguishability, full two-time correlation functions must be calculated. These are numerically very slow to calculate, so to improve the numerical performance, we take inspiration from the natural quantum trajectory link to experiment and calculate these values by simulating a Hanbury Brown and Twiss (HBT) interferometer (to get the coherence) and a Hong-Ou-Mandel (HOM) interferometer (to get the indistinguishability). We show that the natural delay time of coherent feedback allows for simultaneous minimization of two photon emission and pure dephasing/out of plane emission, giving improvements beyond that of a simple increase in spontaneous emission rate. All of the calculations, simulations and writing was done by myself. Feedback and editing were provided by Lora

Ramunno and Stephen Hughes and all authors revised the work following comments made by reviewers in the submission process. Note that we have added section titles to the manuscript in this thesis which are not in the published Letter for ease of reading.

Abstract

Single photon sources (SPSs) are an essential resource for many quantum information technologies. We demonstrate how the inclusion of time-delayed coherent feedback in a scalable waveguide system, can significantly improve the two key SPS figures of merit: coherence and indistinguishability. Our feedback protocol is simulated using a quantum trajectory discretized waveguide model which can be used to directly model Hanbury Brown and Twiss (HBT) and Hong-Ou-Mandel (HOM) interferometers. With the proper choice of the round trip phase, the non-Markovian dynamics from the time-delayed feedback improves the indistinguishability of the SPS by up to 57%. We also show how this mechanism suppresses the detrimental effects of off-chip decay and pure dephasing.

5.1 Introduction

The reliable generation of single photons is important for the implementation of quantum information systems such as quantum cryptography and quantum computing [33]. Semiconductor quantum dots are an excellent source for generating quantum light in the form of single photons or photon pairs [16, 29, 83–87, 110, 111, 142, 145, 283]. In particular, it has been shown that upon excitation by an appropriate laser pulse, preparing the quantum dot in the excited state, the dot can emit a single photon into a desired output mode, e.g., a cavity or waveguide. This generation process is termed as "on-demand" due to the production of a photon number state after each single laser pulse [143].

The key figures of merit for on-demand single photon sources (SPSs) are the brightness, η (the average number of photons per laser pulse), the second order coherence, $g^{(2)}(0)$ (related to the single photon purity), and the indistinguishability, $\mathcal{I}$ (a measure of the coherence of the emitted photon state) [87, 284]. Significant research efforts have been developed to improve the efficiency, purity, and coherence of SPS generation. State of the art systems have achieved $g^{(2)}(0) = 0.012$ and an indistinguishability of $\mathcal{I} = 0.962$ [142],

though often these numbers are after filtering. Unwanted photon pair generation, out of plane emission, and dephasing events (such as through phonon absorption/emission [141, 285]) are all key challenges to overcome for continued improvement of these SPSs.

Feedback, where the output from a system is used as a stabilizing or control mechanism, has been well used across various platforms [36, 39, 43, 146, 147, 152, 161, 167, 191–193]. This is most often implemented through measurement-based feedback, where the output is measured to inform an external control which acts on the system [152, 192–198]. However, this approach is problematic for quantum information systems that rely on maintaining system coherence. Instead, feedback can be included at the system level and act back on the system itself to avoid measurement: *coherent feedback*. Recently, coherent feedback in waveguide quantum electrodynamic systems was shown to significantly alter the photon output statistics with continuous-wave pumping [35–43, 45–48, 161, 167–170, 173, 185, 190, 191, 199–204]. Coherent delay loops have been used in previous experiments for generating quantum states of light such as cluster states [286, 287] or graph states [288], by manipulating the output field of a SPS.

Here, we show how coherent feedback can be used in the pulsed laser regime to improve the figures of merit for a practical SPS. Accurate simulation of coherent feedback is a difficult challenge in quantum circuits, since it introduces a non-Markovian dynamic. To calculate $g^{(2)}(0)$ and $\mathcal{I}$ requires knowledge of the two-time correlation functions, which typically use the quantum regression theorem (QRT) (although other specialized approaches have been developed which avoid the QRT, but they have their own practical limits [289, 290]). The QRT relies on a Markov approximation which fails in the presence of coherent feedback and other specialized techniques must be used [32, 272, 291]. To avoid the non-Markovian dynamic, collisional models can be used which include the waveguide at the system level, rather than treating it as a reservoir. We will use and extend a recently developed quantum trajectory discretized waveguide (QTDW) model [46, 190] that combines a collisional model for the feedback section of the waveguide with the quantum trajectory formalism [176, 177]. Simulating individual realizations of the system gives insights into the underlying stochastic system dynamics and can be averaged to obtain the ensemble dynamics. Our model can also incorporate additional dephasing needed for simulating realistic quantum dots, a limitation of matrix product states, the other main technique for simulating feedback dynamics. Moreover, the QTDW model scales linearly with the number of photon states and is parallelizable.

In this Letter, we connect the QTDW model to photon correlation experiments, to compute $g^{(2)}(0)$ and $\mathcal{I}$ for waveguide quantum electrodynamic systems with coherent feedback, yielding direct simulations of Hanbury Brown and Twiss (HBT) or Hong-Ou-Mandel (HOM) interferometers. We summarize the key features of the QTDW model and outline

its extension to simulate the HBT and HOM measurements. We then show how a coherent feedback can significantly improve the η, $g^{(2)}(0)$, and $\mathcal{I}$ figures of merit for a quantum dot SPS by up to 57%, and explain this improvement in the context of the feedback dynamics.

5.2 Theory and Methods

The system of interest, as shown in Fig. 5.1(a), is a single two-level system (TLS) coupled to a *truncated* waveguide which acts as a feedback loop, returning the output from the TLS to itself. An input laser pulse excites the TLS for SPS emission. The total Hamiltonian in natural units ($\hbar = 1$) for the system, waveguide, and pump (in the interaction picture of the laser and with a rotating wave approximation) is $H = H_{\mathrm{W}} + H_{\mathrm{TLS}} + H_{\mathrm{I}} + H_{\mathrm{pump}}$. The TLS Hamiltonian is $H_{\mathrm{TLS}} = \delta\sigma^{+}\sigma^{-}$ where σ^{+} (σ^{-}) is the Pauli raising (lowering) operator and $\delta = \omega_0 - \omega_{\mathrm{L}}$ is the detuning between the TLS, with frequency ω_0, and the laser, with frequency ω_L. The pump Hamiltonian is $H_{\mathrm{pump}} = \Omega(t)/2(\sigma^{+} + \sigma^{-})$ with the laser pulse shape given by $\Omega(t)$ which drives the quantum dot with a field orthogonal to the waveguide mode polarization [292–294].

In the continuous frequency domain, and in the same interaction picture, the raising (lowering) operator for the photon modes in the waveguide are $b^{\dagger}(\omega)$ ($b(\omega)$) with Hamiltonian $H_{\mathrm{W}} = \int_{-\infty}^{\infty} d\omega\,(\omega - \omega_{\mathrm{L}})\, b^{\dagger}(\omega)b(\omega)$, with $[b(\omega), b^{\dagger}(\omega')] = \delta(\omega - \omega')$. The interaction between the waveguide and TLS, with total radiative rate γ (and symmetric left and right coupling), is described by the Hamiltonian $H_{\mathrm{I}} = \int_{-\infty}^{\infty} d\omega \left[\left(\sqrt{\frac{\gamma}{4\pi}}\sigma^{+}b(\omega) + \sqrt{\frac{\gamma}{4\pi}}e^{i(\phi_M + \omega\tau)}\sigma^{+}b(\omega)\right) + \mathrm{H.c.}\right]$, which incorporates the influence of the feedback loop, including the round trip delay time, τ, and a mirror phase change, ϕ_{M}.

To model the feedback loop, we use a QTDW technique [46, 190], where the field operators, $b(\omega)$, for the waveguide section of interest ($-L < x < 0$) are transformed into the discrete time domain with operators B_n with commutation relation $[B_n, B_{n'}^{\dagger}] = \delta_{n,n'}$. These operators describe a unidirectional slice of the waveguide field which travels around the feedback loop, interacting twice with the TLS, located at the beginning and end of the loop. Additional details on these time domain operators are given in the Supplementary Material.[1] In this transformation, H_{TLS} and H_{pump} are unchanged and the interaction Hamiltonian becomes

$$H_{\mathrm{I}} = \left(\sqrt{\frac{\gamma}{2\Delta t}}\sigma^{+}B_{N-1} + e^{i\phi}\sqrt{\frac{\gamma}{2\Delta t}}\sigma^{+}B_0\right) + \mathrm{H.c.}, \tag{5.1}$$

[1] See Supplemental Material at http://link.aps.org/supplemental/10.1103/PhysRevA.110.L031703 for a discussion on the B_n operators and a comparison of Markovian and non-Markovian feedback.

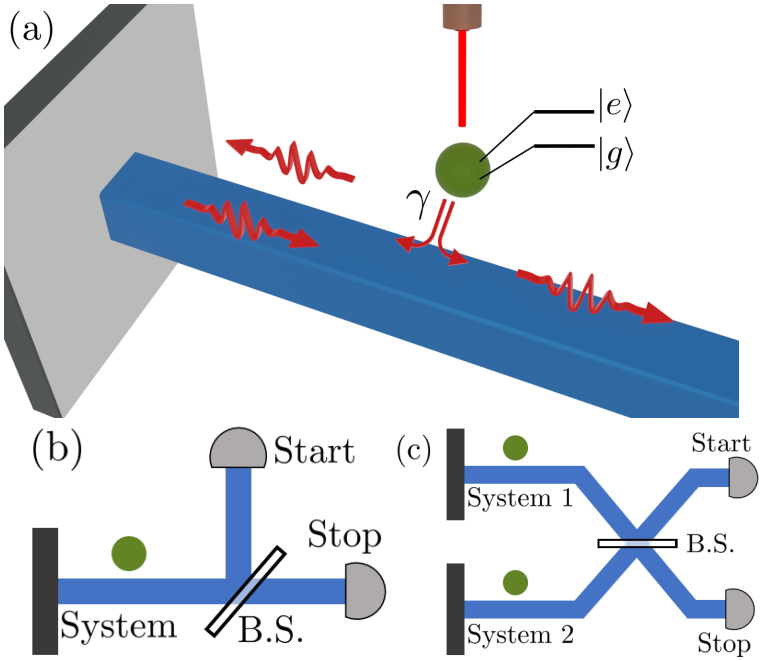

Figure 5.1: Schematics of (a) the driven TLS setup with a coupled coherent feedback loop, (b) the HBT interferometer, and (c) the HOM interferometer; 'B.S.' represents a beam splitter.

where $\phi = \phi_{\mathrm{M}} + \omega_0 \tau$ is the round trip phase change and $\Delta t = \tau/N$ is the time discretization of the feedback loop; now the TLS interacts with the incoming $(N-1)^{\mathrm{th}}$ bin (B_{N-1}) and the outgoing zeroth bin (B_0) which picks up the phase change ϕ. The key advantage of this approach appears in the evolution of the B_n operators under the waveguide Hamiltonian, which is $U_{\mathrm{W}}^{\dagger}(\Delta t) B_n U_{\mathrm{W}}(\Delta t) = e^{-i\delta\Delta t} B_{n-1}$, where $U_{\mathrm{W}}(\Delta t) = e^{-iH_{\mathrm{W}}\Delta t}$. This evolution acts to *pass* the waveguide field forward one bin each time step, where we assume linear dispersion.

A limitation of this approach is that the total number of waveguide photons at any instant must be truncated. Typically, this is chosen to be two to capture the interference between multiple photons in the feedback loop and is a good approximation for most waveguide QED systems [46]. For our system, where the ideal generation is a single photon per pulse, this truncation has no effect on the results. The waveguide field outside of the loop, i.e., for $x > 0$, is modeled through the incoming and outgoing feedback loop bins, and the incoming bins are vacuum fields. During the quantum trajectory step, we take a simulated measurement of the outgoing bin (B_0) and project the full ket vector accordingly. After projection, there is no information in the outgoing bin and it can be dropped to retain

a tractable Hilbert space (absorbing boundary condition). This is a stochastic process, but an average over many individual trajectories yields the ensemble average behavior of the system.

Importantly (and a major advantage over matrix product states) we also include two important dissipation channels in our model of the TLS: (i) off chip decay from the TLS, $C_0 = \sqrt{\gamma_0}\sigma^-$, with rate γ_0, and (ii) pure dephasing in the TLS, $C_1 = \sqrt{\gamma'}\sigma^+\sigma^-$, with rate γ'. These are included as quantum jump operators following standard quantum trajectory theory [176, 177].

Conventionally, the brightness, η, is calculated as the total field emitted from the qubit into the waveguide from a single laser pulse. In the ensemble average picture this is calculated as $\eta = \int_0^\infty dt'\gamma \langle\sigma^+(t')\sigma^-(t')\rangle$. In the quantum trajectory picture, the above expression can also be calculated using the average expectation of $\langle\sigma^+\sigma^-\rangle$ across all trajectories. Equivalently since each trajectory contains a detection record of emitted photons from the waveguide, η can be calculated by taking the average number of photons emitted in a trajectory.

Using the QTDW model, we take advantage of the natural link between the individual trajectories and experiments to calculate $g^{(2)}(0)$ and $\mathcal{I}$ through simulated HBT and HOM interferometers. While our technique can tractably calculate the two-time correlation functions, the HBT and HOM approaches are more intuitive and numerically much faster. In the HBT interferometer [295], see Fig. 5.1(b), the output field is sent to a 50:50 beam-splitter and entangled with the vacuum field. The two new fields are then measured by two detectors, a *start* detector and a *stop* detector, with operators $B^{\text{HBT}}_{\text{start}} = B_0/\sqrt{2}$ and $B^{\text{HBT}}_{\text{stop}} = B_0/\sqrt{2}$ (with vacuum contributions not included as they do not play a role in the measurements). The detection times between the two detectors are correlated by taking the difference between the detection time on the *start* detector and all *stop* detection events, yielding a histogram of time-correlated detection records, $h_{\text{HBT}}(t')$. The system is driven by consecutive pulses to build up a sufficient detection record, each separated by a delay time, T, long enough for the system to completely relax into the ground state before sending in the next pulse.

To simulate the HBT detection, we run each trajectory independently with a single pulse to drive the system and then allowing it to relax for a total run time of T. Next, we place these trajectories in sequential order so that each pulse is separated by T and treat it as one long single quantum trajectory. Since the beam-splitter equally splits the output field, to get the time-correlated detection records we stochastically assign each output jump event in the trajectory to either the start or stop detector and then correlate the two detection records to build the histogram, $h_{\text{HBT}}(t')$, where t' is the time difference

between start and stop events. Assuming no correlations between pulses, when T is chosen sufficiently large, then

$$g^{(2)}(0) = \frac{A_{\mathrm{HBT}}(0)}{A_{\mathrm{HBT}}(T)} \left(1 \pm \sqrt{\frac{1}{A_{\mathrm{HBT}}(0)} + \frac{1}{A_{\mathrm{HBT}}(T)}}\right), \tag{5.2}$$

with $A_{\mathrm{HBT}}(0)$ the area of the peak centered at 0 and $A_{\mathrm{HBT}}(T)$ the area of the next peak, centered at T [284]. The central peak, $A_{\mathrm{HBT}}(0)$, represents the number of pairs of photons being emitted from the system and this is normalized by $A_{\mathrm{HBT}}(T)$, the photon count rate. Since each peak area is calculated as a count of events they carry an uncertainty of $\sqrt{N}$ where N is the number of events. In these results a sufficiently large number of trajectories is carried out to approach an accurate average.

In the HOM simulation [296], see Fig. 5.1(c), we take the interference between the output of two independent copies ('1' or '2') of our system incident on a 50:50 beam splitter (which can easily be extended to an unequal beam splitter). The output bin operator from system 1 (2) is $B_0^{(1)}$ ($B_0^{(2)}$). These are entangled on the beam splitter and sent on to the *start* and *stop* detectors, now with operators $B_{\mathrm{start}}^{\mathrm{HOM}} = (B_0^{(1)} + B_0^{(2)})/\sqrt{2}$ and $B_{\mathrm{stop}}^{\mathrm{HOM}} = (B_0^{(1)} - B_0^{(2)})/\sqrt{2}$. We again drive both copies using consecutive pulses with delay time, T, and time-correlate the detection records of the two detectors. Similar to the HBT interferometer, the correlated detection record can be used to yield a histogram, $h_{\mathrm{HOM}}(t')$.

This HOM setup is more difficult to simulate with the quantum trajectory technique compared to the HBT interferometer, as the detection records are no longer accessible through our jump record of B_0. Instead we entangle two copies of our system using a tensor product, so that the total Hamiltonian is $H_{\mathrm{HOM}} = H^{(1)} \otimes H^{(2)}$, since the two systems are completely independent to begin with. Then, rather than taking our output operators to be $B_0^{(1)}$ and $B_0^{(2)}$, we use the entangled fields after the beam-splitter $B_{\mathrm{start}}^{\mathrm{HOM}}$ and $B_{\mathrm{stop}}^{\mathrm{HOM}}$. Next, when we detect a photon in the *start* (*stop*) detector, we apply the operator $B_{\mathrm{start}}^{\mathrm{HOM}}$ ($B_{\mathrm{stop}}^{\mathrm{HOM}}$) to the combined system. Detection times are recorded to build up detection records for the two detectors which we can time-correlate. Similarly to the HBT interferometer, from $h_{\mathrm{HOM}}(t')$ one can calculate,

$$g_{\mathrm{HOM}}^{(2)}(0) = \frac{A_{\mathrm{HOM}}(0)}{A_{\mathrm{HOM}}(T)} \left(1 \pm \sqrt{\frac{1}{A_{\mathrm{HOM}}(0)} + \frac{1}{A_{\mathrm{HOM}}(T)}}\right), \tag{5.3}$$

which is related to the indistinguishability through [87, 284]

$$\mathcal{I} = 1 - g_{\mathrm{HOM}}^{(2)}(0). \tag{5.4}$$

Without feedback, i.e., for a TLS coupled to an open waveguide [87, 110, 293, 297], to generate a SPS we pump the system with a π-pulse to excite the TLS and decay back to the ground state, emitting a single photon. Note that we correct for the bi-directional output in the results without feedback so both output fields are accounted for. In the limit of an infinitely short pulse width, and neglecting other decoherence effects such as phonon interactions [87], this TLS is a perfect SPS with $g^{(2)}(0) = 0$ and $\mathcal{I} = 1$. The perfection of these sources fail when a finite pulse width is taken to account (as this introduces a chance of two photon emission) and sources of detuning and off-chip decay are included (which spoils coherence) [239]. The TLS is driven by a Gaussian π-pulse, defined by $\Omega(t) = \left(\pi/\sigma\sqrt{2\pi}\right) \exp\left[-t^2/2\sigma^2\right]$, where $\sigma = t_p/2\sqrt{2\ln 2}$ and t_p is the FWHM pulse width.

5.3 Results

To include feedback, the delay time, τ, and the phase change, ϕ, must be strategically chosen to yield the best results. We found this occurs when the non-Markovian feedback returns just after the pulse has finished driving the system, $\tau = 3t_p$, and with a constructive interference, $\phi = 0$. The choice of delay time is discussed in the Supplementary Material.[2] This works to limit both of the primary drawbacks to a perfect SPS: pair emission and additional loss channels. Pair emission occurs when the TLS emits a photon during the pulse and is re-excited, emitting a second photon. Thus, to minimize pair emission, a weak decay rate from the system during the pulse is best. However, in realistic systems, the TLS is limited by off-chip decay and pure dephasing. To minimize these, the TLS should decay as quickly as possible. Hence, a time-delayed coherent feedback works optimally to improve the SPS by not increasing the decay rate until after the pulse has finished interacting with the TLS. In Fig. 5.2(a), the TLS population dynamics ($\langle\sigma^+\sigma^-\rangle(t)$) show how the delay in the non-Markovian feedback begins after the pulse has fully passed and the TLS decays much faster than the dynamics without feedback. This also yields the proper choice of T to ensure the TLS has completely decayed into the ground state, which is taken to be $\gamma T = 20$ (well after the decay in Fig. 5.2(a)) in the HBT and HOM simulations. For the pulse widths in these results, $0.05 \leq \gamma t_p \leq 0.25$, this gives a range of delay times between $0.15 \leq \gamma\tau \leq 0.75$. This range is equivalent to a delay line with length 4.5 mm to 22.5 mm in a photonic crystal waveguide with $n_g = 10$ for a quantum dot system such as in [27] with a decay rate of $\gamma \approx 1\text{ns}^{-1}$.

[2] See Supplemental Material at http://link.aps.org/supplemental/10.1103/PhysRevA.110.L031703 for a discussion on the B_n operators and a comparison of Markovian and non-Markovian feedback.

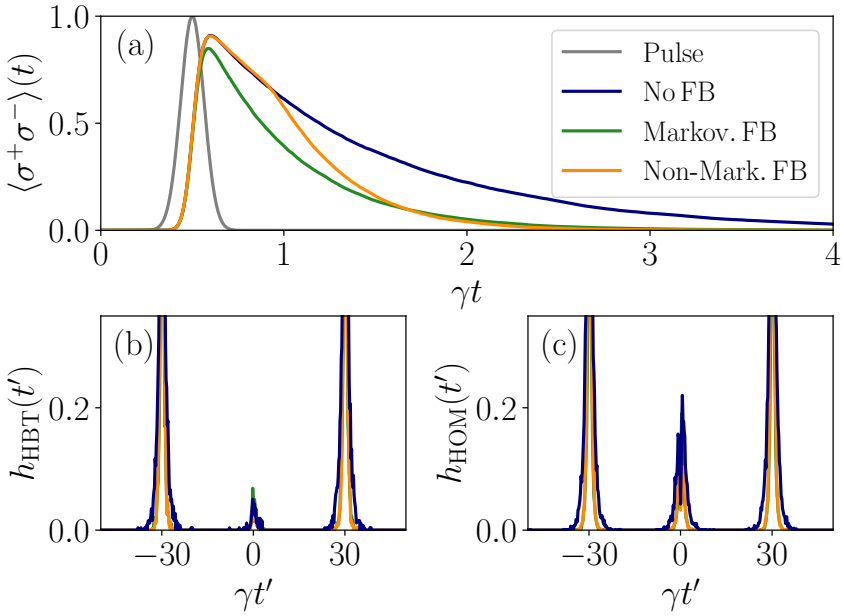

Figure 5.2: (a) The TLS population dynamics without feedback, with Markovian feedback, and with non-Markovian feedback for a pulse with width $\gamma t_p = 0.15$. For this pulse width, the delay time used is $\gamma\tau = 3\gamma t_p = 0.45$ so the non-Markovian feedback returns after the pulse. No additional loss channels are included. In (b) and (c), the center peaks of the resulting HBT and HOM histograms for this feedback and pulse setup respectively, with pure dephasing (using $\gamma' = \gamma$).

Figure 5.3 shows improvements in the brightness, second order coherence, and indistinguishability when non-Markovian coherent feedback is included. We display results with and without feedback as a function of changing pulse width, off chip decay rate, and pure dephasing rate. In Figs. 5.3(a), (e), and (i) no additional loss channels are included so the only factor resulting in an imperfect SPS is pair emission. As shown in Fig. 5.2(a), the dynamics without and with a non-Markovian feedback have the same decay rate while the pulse drives the TLS so they undergo the same rate of pair emission. Thus, the SPS acts equally well with and without feedback.

When a realistic SPS is considered, i.e., with additional loss channels, the improvement with feedback is clearly seen. In Figs. 5.3(b), (f), and (j) we vary the pulse width but now have off-chip decay with rate $\gamma_0 = 0.1\gamma$ and pure dephasing with rate $\gamma' = 0.5\gamma$. The brightness is primarily affected by the off-chip loss as it introduces a new channel for the TLS to decay into, rather than the waveguide; thus, for some pulses, no corresponding

photon detection is found. Across all pulse widths we find an average relative improvement of 39% in the brightness. The second order coherence is primarily affected by the pair emission from the system and so there is minimal relative improvement of 3.5% with feedback as the rates of pair emission are identical. Pure dephasing events spoil the coherence of the emitted photons and so have the largest effect on the indistinguishability. With feedback, the SPS has an average relative improvement of 35% in the indistinguishability.

A Markovian feedback, $\tau \to 0^+$, will also increase the spontaneous emission rate at all times when $\phi = 0$ [167] as shown in Fig. 5.2(a). This will also improve the SPS performance in the presence of off-chip decay and pure dephasing, in an identical way as including a Purcell factor of 2. Crucially though, this also increases the pair emission rate which detrimentally affects the SPS. See the Supplementary Material[3] for a comparison between the improvements with Markovian and non-Markovian feedback where Markovian feedback produces a worse coherence and indistinguishability in all cases. A similar effect in a coupled cavity-TLS setup has been shown in [141] where a non-Markovian Purcell factor can arise in the bad cavity regime with pulsed excitation.

We also compare η, $g^{(2)}(0)$ and $\mathcal{I}$ with and without feedback as a function of the off-chip decay rate in Figs. 5.3 (c), (g), and (k), and as a function of the pure dephasing rate in Figs. 5.3(d), (h), and (l), with a fixed pulse width of $\gamma t_p = 0.15$. We find that for off-chip decay (Figs. 5.3 (c), (g), and (k)), feedback does an excellent job of suppressing the effects of the additional output channel, decreasing the impact on brightness by 26%, coherence by 39% and on indistinguishability by 57%. For the pure dephasing rate (Figs. 5.3(d), (h), and (l),), η and $g^{(2)}(0)$ are minimally affected by the increase in pure dephasing events so there is little difference between the results with and without feedback. Pure dephasing has its greatest affect on the indistinguishability, and feedback does a good job of reducing its impact, suppressing its effects by 44%. Figure 5.2(c) shows an example HOM histogram when $\gamma' = \gamma$ highlighting the decreased area of the central peak in the case with non-Markovian feedback leading to the improvement in indistinguishability.

In summary, we have exploited a QTDW model to calculate the $g^{(2)}(0)$ and $\mathcal{I}$ figures of merit for a SPS by directly simulating an HBT or HOM interferometer. This approach allows one to bypass the quantum regression theorem in order to simulate the non-Markovian dynamics that arise when coherent feedback is included in a waveguide quantum electrodynamic system. Using this technique, we have shown that direct inclusion of a time-delayed coherent feedback can improve the brightness, coherence, and indistinguishability of a SPS, even when pure dephasing is a significant source of decoherence in the system. This work

[3]See Supplemental Material at http://link.aps.org/supplemental/10.1103/PhysRevA.110.L031703 for a discussion on the B_n operators and a comparison of Markovian and non-Markovian feedback.

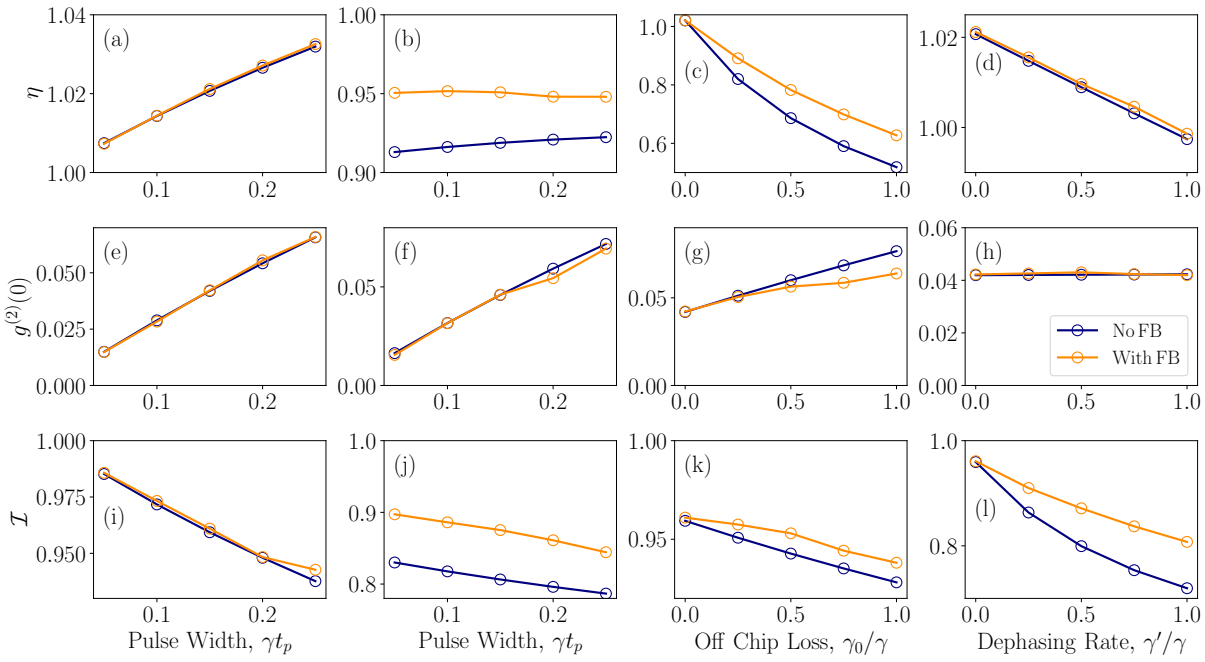

Figure 5.3: (a)-(d) The brightness, (e)-(h) the second order coherence, and (i)-(l) the indistinguishability of the output single photons. The width of the incoming pulse is varied without additional dissipation channels C_0 and C_1 in (a), (e), and (i), while these channels are included ($\gamma_0 = 0.1\gamma$ and $\gamma' = 0.5\gamma$) in (b), (f), and (j). The pulse width is then set at $\gamma t_p = 0.15$ and the off chip decay rate is varied in (c), (g), and (k) with $\gamma' = 0$, while the pure dephasing rate is varied in (d), (h), and (l) with $\gamma_0 = 0$. Each data point with feedback is an average of 100,000 trajectories for η and $g^{(2)}(0)$, and 20,000 trajectories for $\mathcal{I}$.

harnesses a single characteristic of feedback, namely its ability to enhance spontaneous emission, in order to achieve these improvements. In future work, other aspects of feedback such as excitation trapping and additional nonlinear behavior are also expected to be useful for photon pair emission and other quantum information system objectives.

5.4 Acknowledgements

This work was supported by the Natural Sciences and Engineering Research Council of Canada (NSERC), the National Research Council of Canada (NRC) through the Small Teams Ideation Program QPIC, Queen's University, and the University of Ottawa. We thank Dan Dalacu and Robin Williams for support and useful discussions.

5.5 Supplementary Material for "Improving On-Demand Single Photon Source Coherence and Indistinguishability Through a Time-Delayed Coherent Feedback"

5.5.1 Finding the Discrete Time Domain Operators, B_n

The Hamiltonian for the waveguide in the continuous frequency domain and in the interaction picture with respect to the laser frequency is

$$H_{\mathrm{W}} = \int_{-\infty}^{\infty} d\omega \, (\omega - \omega_{\mathrm{L}}) \, b^{\dagger}(\omega) b(\omega), \tag{5.5}$$

where $b(\omega)$ ($b^{\dagger}(\omega)$) is the lowering (raising) operator for the propagating photon modes in the waveguide, with the usual commutator $[b(\omega), b^{\dagger}(\omega')] = \delta(\omega - \omega')$. In the SDW model, the waveguide is represented through individual slices of the waveguide field so the continuous frequency domain needs to be transformed into the discrete time domain. First, the discrete frequency picture is given by using the transformation $b(\omega) = \sqrt{L/\pi} b_k$ where L is the length of the feedback loop (i.e. from the qubit to the mirror) [190], and b_k is the operator for the discrete frequency ω_k. Then a discrete Fourier transform can be used to get the relationship between discrete time and frequency domains

$$\begin{aligned} B_n &= \frac{1}{\sqrt{N}} \sum_{k=0}^{N-1} b_k e^{i(\omega_k - \omega_0) n \Delta t}, \\ b_k &= \frac{1}{\sqrt{N}} \sum_{n=0}^{N-1} B_n e^{-i(\omega_k - \omega_0) n \Delta t}, \end{aligned} \tag{5.6}$$

where N is the total number of discrete operators used to describe the waveguide and $\omega_k = \pi k / L$ assumes linear dispersion for the waveguide mode. Note, B and $B^{\dagger}$ have dimensionless units and the commutator for the operators is $[B_n, B_{n'}^{\dagger}] = \delta_{n,n'}$.

These operators evolve under the waveguide Hamiltonian through $U_{\mathrm{W}}^{\dagger}(\Delta t) B_n U_{\mathrm{W}}(\Delta t)$ where $U_{\mathrm{W}}(\Delta t) = e^{-i H_{\mathrm{W}} \Delta t}$. To compute this, the waveguide Hamiltonian is first transformed to the discrete frequency picture to be

$$H_{\mathrm{W}} = \sum_{k=0}^{N-1} \omega_k b_k^{\dagger} b_k. \tag{5.7}$$

Then, by using the expansion for B_n in terms of b_k in Eqn. (5.6), the evolution of the waveguide Hamiltonian is

$$\begin{aligned} U_{\mathrm{W}}^{\dagger}(\Delta t) B_n U_{\mathrm{W}}(\Delta t) &= \frac{1}{\sqrt{N}} e^{-i\delta\Delta t} \sum_{k=0}^{N-1} b_k e^{i\omega_k (n-1)\Delta t} \\ &= e^{-i\delta\Delta t} B_{n-1}. \end{aligned} \tag{5.8}$$

As discussed in the Letter, this shows how the evolution acts to pass the waveguide field forward from one time bin operator to the next.

5.5.2 Comparison between Markovian and Non-Markovian Feedback Effects

It is not immediately obvious that the time delay in the coherent feedback is required to achieve an improvement in the single photon source (SPS) figures of merit. The returning feedback, with $\phi = 0$, relies on constructively interfering with the output from the two level system (TLS) to enhance the rate of spontaneous emission [36, 185]. In the Markovian limit, $\tau \to 0^+$, this acts as a twofold Purcell enhancement of the spontaneous emission rate $\gamma \to 2\gamma$. This seems to be the best case because a higher spontaneous emission rate will decrease the number of off-chip decay and pure dephasing events that occur, so a negligible delay time allows the higher emission rate to immediately begin. However, as discussed in the Letter, this also increases the rate of pair emission from the system and so there is a trade-off in the improvements that can be made with Markovian feedback.

Figure 5.4 shows the same results as in Fig. 3 of the Letter with the performance of a TLS with Markovian feedback also included. We now term the time-delayed coherent feedback as non-Markovian feedback since but note that we are changing the time-delay depending on the pulse width, with $\tau = 3t_p$. We also include a dashed red line representing the value for an ideal SPS.

In Figs. 5.4(a)-(d) we find that the Markovian feedback is always brighter than the other two cases. When off-chip decay is not present, $\gamma_0 = 0$, in Figs. 5.4(a) and (d), $\eta > 1$ and the Markovian feedback is actually worse since the additional brightness is coming from unwanted photon pair emission. When $\gamma_0 \neq 0$ in Figs. 5.4(b) and (c), the Markovian feedback is best at mitigating this loss channel and thus has the best brightness. However, this comes at the cost of a worse second order coherence in Figs. 5.4(e)-(h). Since $g^{(2)}(0)$ is mostly sensitive to pair emission, we find that the Markovian feedback performs much

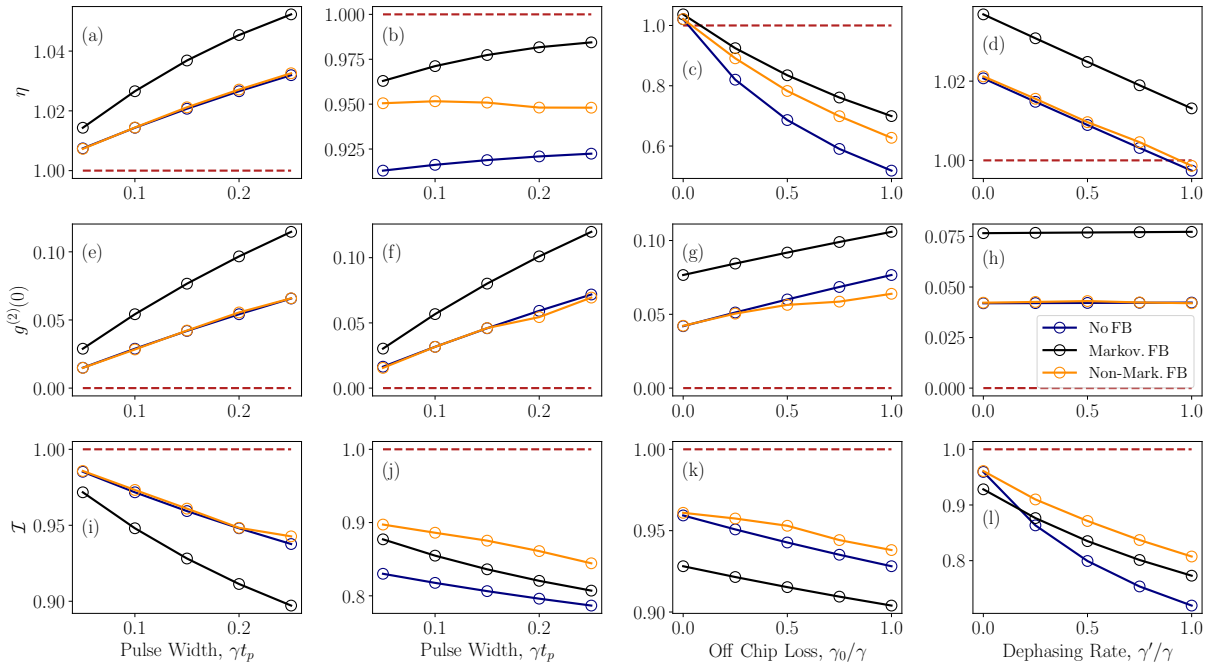

Figure 5.4: (a)-(d) The brightness, (e)-(h) the second order coherence, and (i)-(l) the indistinguishability of the output single photons. The width pulse width is varied without additional dissipation channels C_0 and C_1 in (a), (e), and (i) while these channels are included ($\gamma_0 = 0.1\gamma$ and $\gamma' = 0.5\gamma$) in (b), (f), and (j). The pulse width is then set at $\gamma t_p = 0.15$ and the off chip decay rate is varied in (c), (g), and (k) with $\gamma' = 0$, while the pure dephasing rate is varied in (d), (h), and (k) with $\gamma_0 = 0$. Each data point with feedback in (a)-(l) is an average of 100,000 trajectories and in (i)-(l) an average of 20,000 trajectories.

worse than the case without feedback or with a time-delayed feedback, in some cases with nearly double the $g^{(2)}(0)$.

Since a time-delay feedback mitigates both pair emission and pure dephasing events, it performs best in the indistinguishability which is very sensitive to both. Of these, Markovian feedback only mitigates pure dephasing so it performs better than the no feedback case in Fig. 5.4(j) and (l), but is still worse than non-Markovian feedback. Essentially, non-Markovian feedback is able to gain the benefits of a slower emission rate during the pulse (mitigating pair emission) and a faster emission rate overall (mitigating additional loss channels). Thus, aside from the brightness, non-Markovian feedback tends to perform better than either without feedback or Markovian feedback. At worse it performs nearly equal to the better of the two.

In Fig. 5.5, the second order coherence and indistinguishability are shown as a function of delay time with the pulse width set at $\gamma t_p = 0.15$ and dissipation rates $\gamma_0 = 0.1\gamma$ and $\gamma' = 0.5\gamma$. Markovian feedback is equivalent to a delay time of $\tau = 0$ in these figures and there is a clear improvement by increasing the delay time to be non-negligible, and enter the non-Markovian regime. This improvement peaks at $\tau = 3t_p$, indicated by the red line, which informs our choice of this delay time for the non-Markovian feedback case.

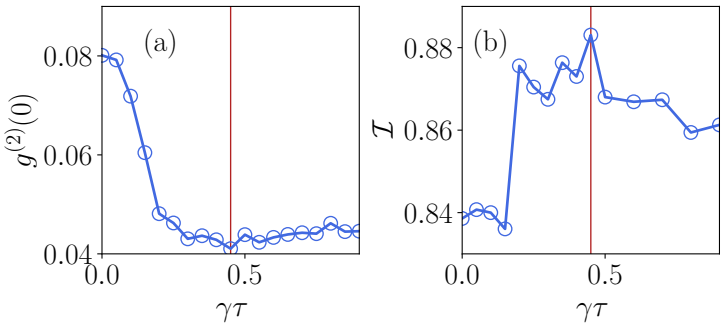

Figure 5.5: (a) The second order coherence and (b) the indistinguishability as a function of delay time. The pulse width is set at $\gamma t_p = 0.15$ and additional dissipation channels have rates $\gamma_0 = 0.1\gamma$ and $\gamma' = 0.5\gamma$. The red line indicates the chosen non-Markovian delay time used in Fig. 5.4 and in the Letter. Each point in (a) is an average of 100,000 trajectories and each point in (b) is an average of 10,000 trajectories.

Chapter 6

Quantum-dot single photon source performance with quasi-coherent excited state preparation schemes

This work is a submitted manuscript to Physical Review A. I am the first author on the work along with co-authors Lora Ramunno and Stephen Hughes. Three recent off-resonant pulse preparation schemes have been proposed which drive a quantum dot to the excited state without using a resonant pulse for single photon emission. These are a symmetrically detuned dichromatic dichromatic pulse, a notch-filtered adiabatic rapid passage (NARP) pulse, and a swing up of the quantum emitter population (SUPER) technique. These all claim excellent performance, but following discussions with experimental colleagues, it would be useful to make a comparison of all three using the same model system. Two of these techniques require very short time steps for accurate simulation, and so master equation solutions of the full two time correlation functions with `QuTiP` were unable to converge. We used the quantum trajectory techniques developed in Ch. 5, without the coherent feedback, to simulate these systems. Due to the very high instantaneous Rabi frequencies employed by these techniques, we include a weak phonon coupling model to account for the influence of longitudinal acoustic phonons in the quantum dot. The results here identify the NARP scheme as the most robust of the three, while the SUPER scheme can get slightly better overall performance. We hope this paper is useful for experimental groups weighing the pros and cons of these techniques. All of the calculations, simulations and writing was done by myself. Feedback and editing were provided by Lora Ramunno and Stephen Hughes.

Abstract

The preparation of photonic qubits in the excited state is an integral part of the performance of an on-demand single photon source (SPS). Conventional resonant excitation, an excellent approach to maximize the coherence and indistinguishability of the SPS, often requires polarization filtering to remove the pump signal and isolate the qubit emission, but this results in an inherent 50% hit to the efficiency. Recent excitation schemes strategically try to exploit pulses that excite the qubit while avoiding spectral overlap to bypass this required filtering. In this work, we compare three such pumping schemes to quantify the important SPS figures-of-merit for off-resonant quantum dot schemes, using: (i) a symmetrically detuned dichromatic pulse, (ii) a notch-filtered adiabatic rapid passage (NARP) pulse, and (iii) a swing up of the quantum emitter population (SUPER) pulse. Due to large instantaneous pulse strengths, the dichromatic pulse suffers from phonon-induced dephasing which can lower the SPS performance by up to 50%. In contrast, the NARP and SUPER pulses are shielded from phonon coupling to differing degrees but both maintain excellent SPS performance. The SUPER pulse can lose significant efficiency if there is variance in its constituent pulses' amplitude, pulse width, or frequency, while the NARP pulse, though potentially more difficult to realize in experiments, is robust against variance in the pulse preparation.

6.1 Introduction

A high performance on-demand single photon source (SPS) is an invaluable resource for fundamental quantum optics experiments and quantum technologies [33]. An ideal deterministic source (i.e., on-demand) would be perfectly efficient ($\eta = 1$), meaning it emits every time it is pumped and the emitted photons would be coherent ($g^{(2)}(0) = 0$) and indistinguishable ($\mathcal{I} = 1$). The efficient generation of pure quantum light is an ongoing technical problem being worked on in many different platforms, for example superconducting transmon qubits [119, 131, 298], trapped ions [22, 23], spin-centres in solid state sources such as diamond [90, 93, 134], and quantum dot (QD) sources [84, 86, 88, 103, 110, 135, 136, 297] to list a few, each with their own approaches to performance improvement.

Current state of the art QD SPSs have achieved coherences as low as $g^{(2)}(0) = 7.5 \times$

10^{-5} [103] and indistinguishabilities as high as $\mathcal{I} = 0.995$ [135]. Simultaneously maximizing these figures of merit, while keeping a high efficiency is a difficult problem with a recent paper showing an overall best performance (to our knowledge) of $g^{(2)}(0) = 0.0205$, $\mathcal{I} = 0.9856$, and $\eta = 0.712$ [136]. These near pure SPSs are typically driven by resonant π-pulses that coherently drive inversion of the qubit [299, 300]. The potential problem with this scheme in a waveguide-QED system is that the weak qubit emission and driving pulse both travel through the same waveguide channel causing the emission to be overshadowed by the much stronger driving pulse. To overcome this, techniques such as polarization filtering are used [61, 108, 300–302] where the light with polarization parallel to the driving pulse polarization is filtered to isolate the qubit emission. This inherently removes half of the qubit emission events, capping η at 0.5 which does not meet the requirement of an on-demand source.

To avoid this required filtering, it would be useful to have a driving scheme which avoids using a laser on resonant with the qubit. There have been many such driving protocols such as off-resonant phonon-assisted inversion [303–308], two photon excitation of the biexciton [100, 102, 103, 309], and p-shell excitation [29, 310, 311]. Such schemes have shown excellent results, with a CW-dressing scheme utilizing the biexciton-exciton cascade yielding $g^{(2)}(0) = 0.028$, $\mathcal{I} = 0.905$, and $\eta > 0.95$ [294, 312]. This technique avoids polarization filtering but introduces timing jitter (decoherence due to the finite spontaneous emission time of the biexciton-exciton decay) which must be overcome [313, 314]. Recently, three such schemes have been proposed and experimentally demonstrated, showing only a small effect on the SPS performance by preparing the qubit with these protocols. These are a symmetrically detuned dichromatic pulse protocol [142, 315], the notch filtered adiabatic rapid passage (NARP) protocol [144], and the swing up of the quantum emitter population (SUPER) protocol [143, 316–319].

These three schemes have been presented with a variety of simulated and experimental results on different platforms to show their performance as a SPS. However, these various studies all make different underlying assumptions for their systems (such as different dissipation modeling and qubit decay rates) which makes a direct comparison between these works difficult. It is useful for the scientific community to compare the performance of these schemes in a realistic system while removing as many differences in the implementation as possible. Indeed in [320], a comparison between the dichromatic and SUPER schemes is done for a qubit coupled to a cavity which drives emission into the zero phonon line. In addition, we are not aware of any works that have computed $\mathcal{I}$ for the NARP schemes.

In this paper, we present a theoretical study of a SPS platform, where we consider a QD (treated as the qubit) generating single photons in a waveguide quantum electrodynamic (QED) system shown schematically in Fig. 6.1. Our model also accounts for phonon-

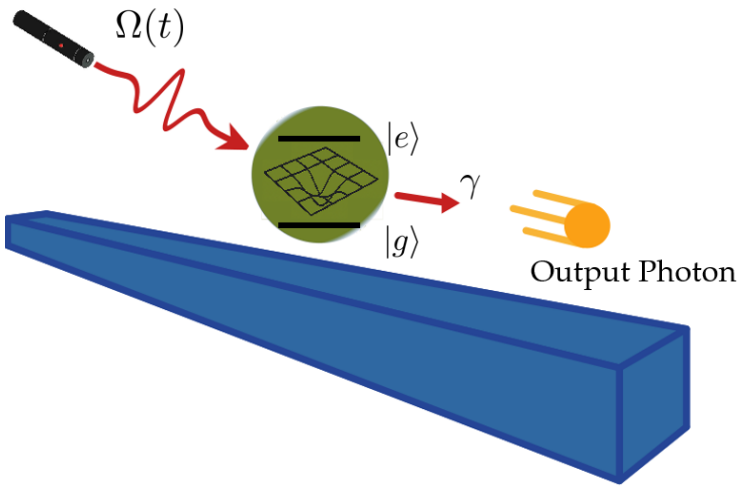

Figure 6.1: Schematic of the single photon emission process. The qubit (with LA acoustic phonons and coupled to the waveguide with rate γ) is driven by one of the three pulse schemes and (ideally) emits a single photon in the waveguide.

induced processes, in the calculations of the key SPS parameters.

Specifically, we make a detailed comparison of the SPS performance of a bare qubit coupled to a waveguide under the dichromatic, NARP, and SUPER schemes. To incorporate dissipation from a realistic system, we also employ a weak phonon coupling model (appropriate for low temperatures) [313] and plot the resulting phonon-induced dissipation rates which arise from the drive strength and detuning of each of the three schemes. Using parameters from the original publications for each driving scheme, we compare the SPS performance in η, $g^{(2)}(0)$, and $\mathcal{I}$. These are the first calculations of indistinguishability for the NARP protocol that compare its performance against other driving schemes. Additionally, the robustness of each scheme is considered, that is if the incoming laser pulse (or constituent pulses) are imperfect, how much does that impact the performance of the SPS under each driving scheme.

Our key findings show that the dichromatic scheme suffers from the influence of phonons, which significantly lowers its performance as a single photon source. The NARP scheme has limited effects from phonon coupling while the SUPER scheme completely avoids the problem with its far detuned pulses. We also find that both NARP and SUPER both have excellent coherence and indistinguishability in the resulting single photons. While the SUPER scheme has slightly better overall performance, it is highly sensitive to changes in the composite laser parameters, while the NARP scheme is quite robust against variation in

the filtering width or laser amplitude.

6.2 Theory and Methods

6.2.1 System Hamiltonian

To investigate the performance of each of the driving schemes, the SPS is modeled as a QD exciton (single electron-hole pair) including its coupling to longitudinal acoustic (LA) phonons. Specifically, the QD is treated as a two level system (TLS), which we refer to as a qubit, with ground state $|g\rangle$, excited state $|e\rangle$, and resonance frequency ω_0. Neglecting electron-phonon coupling and dissipation processes for now, the system Hamiltonian for an optically excited quantum dot is

$$H_{\mathrm{S}} = \hbar\omega_0\sigma^+\sigma^- + \frac{\hbar\Omega(t)}{2}(\sigma^+ + \sigma^-), \tag{6.1}$$

where σ^+ (σ^-) is the Pauli raising (lowering) operator. The time-dependent Rabi field $\Omega(t)$ is defined by the driving field of interest, before we have moved into an interaction picture and without any rotating wave approximations.

The qubit is coupled to a waveguide with radiative rate γ, proportional to the dipole strength and the local density of states in the waveguide. This is included with the quantum jump channel $C_0 = \sqrt{\gamma}\sigma^-$ in a quantum trajectory picture [176–178], equivalent to a Lindblad dissipation operator in a master equation approach.

6.2.2 Optical Pulsed Pumping Schemes

We now present the specific form for the system Hamiltonian in Eq. (6.1), in the rotation wave approximation, for the three pumping schemes we consider here: the dichromatic, NARP, and SUPER pulses, along with a mathematical description of each scheme.

The first of the three pulsed driving schemes we compare, is a symmetrically detuned dichromatic pulse proposed in [142] that consists of two pulses, each symmetrically detuned from the TLS by δ. The two pulses have identical envelopes, $\varepsilon(t)$, are coincident in time, but can have a fixed phase difference φ. The total Rabi frequency for these two pulses is

$$\begin{aligned}\Omega(t) &= \frac{\hbar\varepsilon(t)}{2}\cos\left((\omega_{\mathrm{L}}+\delta)t+\varphi\right) + \frac{\hbar\varepsilon(t)}{2}\cos\left((\omega_{\mathrm{L}}-\delta)t\right) \\ &= \hbar\varepsilon(t)\cos\left(\delta t+\frac{\varphi}{2}\right)\cos\left(\omega_{\mathrm{L}}t+\frac{\varphi}{2}\right).\end{aligned} \tag{6.2}$$

In the second line we can see that these two pulses act like a resonant pulse with a new envelope $\varepsilon'(t) = \varepsilon(t)\cos\left(\delta t + \frac{\varphi}{2}\right)$. There is a small difference from the resonant case introduced by φ in the $\cos\left(\omega_{\mathrm{L}} t + \frac{\varphi}{2}\right)$ term. When moving into the interaction picture at the laser frequency with a rotating wave approximation (RWA), this introduces a phase on the TLS operators

$$H_{\mathrm{S}}^{\mathrm{Di}} = \frac{\hbar\varepsilon'(t)}{2}\left(e^{-i\varphi/2}\sigma^{+} + e^{i\varphi/2}\sigma^{-}\right). \tag{6.3}$$

To yield population inversion, as predicted by the Area Theorem (and neglecting dissipation processes), the time integrated pump area must be an odd multiple of π, i.e. $\int dt\varepsilon'(t) = (2n+1)\pi$ where $n \in \mathcal{Z}$. If we take the original pulse envelopes to be Gaussian,

$$\varepsilon(t) = \Omega_0 e^{-t^2/2t_{\mathrm{p}}^2}, \tag{6.4}$$

then we need to choose

$$\Omega_0 = \frac{\pi}{\sqrt{2\pi t_{\mathrm{p}}^2}\cos(\varphi/2)e^{-\delta^2 t_{\mathrm{p}}^2/2}}, \tag{6.5}$$

for the pulse area to be π. As a consequence, δt_{p} is the quantity of interest to avoid overlap with the spectrum of the qubit emission. Ideally, one would want a narrow spectral pulse width (large t_{p}) and a large separation (large δ). But by increasing both of these quantities, Ω_0 will correspondingly increase exponentially.

The second pumping scheme is a NARP pulse, proposed in [144], which improves upon the original ARP technique [321, 322]. The original technique uses a chirped pulse to drive the system, which has a frequency which varies linearly with time. For a Gaussian envelope, the chirped pulse takes the form

$$\Omega(t) = \Omega_0 e^{-t^2/2t_{\mathrm{p}}^2} e^{-i(\omega_{\mathrm{L}} + \alpha t/2)t}, \tag{6.6}$$

where Ω_0 is chosen to achieve the desired pulse area, t_{p} is the pulse duration, ω_{L} is the center frequency of the pulse, and α is the linear temporal chirp.

The interaction Hamiltonian with the RWA is

$$H_{\mathrm{S}}^{\mathrm{NARP}} = \hbar\Delta(t)\sigma^{+}\sigma^{-} + \frac{\hbar\varepsilon(t)}{2}\left(\sigma^{+} + \sigma^{-}\right), \tag{6.7}$$

where we now have a time-dependent detuning between the pulse and TLS given by $\Delta(t) = \omega_0 - \omega_{\mathrm{L}} - \alpha t$, composed of a constant detuning, $\omega_0 - \omega_{\mathrm{L}}$, and α the rate of change of the detuning. Note we choose a positive chirp here to use the lower dressed state in the ARP method, avoiding phonon induced dephasing that occurs when going through the upper dressed state.

For ARP to work, the following conditions are required,

$$|\alpha| t_{\mathrm{p}}^2 \gg 1, \tag{6.8}$$

to ensure the change in frequency from the chirp is significant enough over the pulse duration of the Gaussian envelope, and

$$|\alpha| t_{\mathrm{p}}^2 \ll \Omega_0^2 t_{\mathrm{p}}^2, \tag{6.9}$$

which is the adiabatic condition for the changing dressed state energy splitting as $\Delta(t)$ varies. Notably, this means that NARP works for any pulse as long as Eq. (6.9) is satisfied.

The NARP scheme modifies the ARP pulse with an amplitude mask, $A(\omega)$, on top of the chirped pulse. The full mask (including the chirp) can be defined as $M(\omega) = A(\omega)e^{i\Phi(\omega)}$ and this gives the NARP pulse envelope to be

$$\varepsilon'(t) = \mathcal{F}^{-1}[\mathcal{F}[\varepsilon(t)] \cdot M(\omega)], \tag{6.10}$$

where $\mathcal{F}$ denotes the Fourier transform. The two masks take the form

$$\begin{aligned} A(\omega) &= 1 - e^{-\ln(2)(\omega-\omega_{\mathrm{L}})^2/\delta^2}, \\ \Phi(\omega) &= \frac{\alpha'}{2}(\omega - \omega_{\mathrm{L}})^2, \end{aligned} \tag{6.11}$$

where 2δ is the FWHM of the spectral hole and α' is the spectral chirp (equivalent to the temporal chirp α but applied to the pulse in the frequency domain)

$$\alpha' = \alpha \frac{t_{\mathrm{p}}^4}{1 + \alpha^2 t_{\mathrm{p}}^4}. \tag{6.12}$$

The final driving scheme of interest is the SUPER scheme proposed by [143] which uses two pulses far detuned from the qubit frequency to drive the qubit using the beating between the two pulses. The time dependent drive is

$$\Omega(t) = \varepsilon_1'(t)e^{-i\omega_1 t} + \varepsilon_2'(t-\tau)e^{-i(\omega_2 t+\varphi)}, \tag{6.13}$$

with ω_1 and ω_2 the two frequencies of the input pulses and φ a possible phase difference between them. The two pulse envelopes, ε_1' and ε_2', are both Gaussians with a possible time delay, τ, between the two:

$$\varepsilon_1'(t) = \Omega_1 e^{-t^2/2t_{\mathrm{p},1}^2}, \tag{6.14}$$

$$\varepsilon_2'(t) = \Omega_2 e^{-(t-\tau)^2/2t_{\mathrm{p},2}^2}. \tag{6.15}$$

Transforming the system Hamiltonian with this drive into the interaction picture at the first laser frequency, ω_1, (with the RWA) yields

$$H_{\mathrm{S}}^{\mathrm{SUPER}} = \hbar\Delta_1\sigma^+\sigma^- + \frac{\hbar\varepsilon_1'(t)}{2}\left(\sigma^+ + \sigma^-\right) + \frac{\hbar\varepsilon_2'(t)}{2}\left(e^{-i(\Delta_1-\Delta_2)t}\sigma^+ + e^{i(\Delta_1-\Delta_2)t}\sigma^-\right), \tag{6.16}$$

where $\Delta_i = \omega_0 - \omega_i$. This creates a dynamic where the qubit is pumped far off resonance by the first drive, while also being driven by the second laser with a fast oscillation at a frequency equal to the beating between the lasers. To ensure population inversion, the pulse detunings must be chosen such that

$$\Delta_2 = \Delta_1 - \sqrt{\varepsilon_1^2(t=0) + \Delta_1^2}. \tag{6.17}$$

This coordinates the beating between the lasers to be equal to the effective Rabi frequency at the peak of the first pulse to follow the required frequency switching in the detuned drive to complete inversion.

6.2.3 Electron-Phonon Scattering Model

To take into account qubit dissipation and dephasing, we include a model for the QD-phonon reservoir coupling through a weak phonon coupling model [313]. This model treats the exciton-phonon interaction, perturbatively, neglecting the non-Markovian parts of the scattering. The weak phonon model works quantitatively well at low temperatures [313][1], and for this work, we consider $T = 4$ K. This approach is especially effective here where the instantaneous pulse strengths can be very large causing a polaron transform approach (which includes phonons, non-perturbatively) to fail [323, 324].

The (weak) phonon master equation is

$$\frac{d\rho}{dt} = \frac{-i}{\hbar}\left[H_{\mathrm{S}}^x, \rho\right] + \mathbb{L}_{\mathrm{W}}\rho, \tag{6.18}$$

where ρ is the density matrix, x denotes one of the three schemes, and

$$\mathbb{L}_{\mathrm{W}}\rho = \int_0^\infty d\tau\Gamma_{\mathrm{W}}(\tau)\left(\tilde{N}(t-\tau,t)\rho N - N\tilde{N}(t-\tau,t)\rho\right) + \mathrm{H.c.} \tag{6.19}$$

[1] Apart from a polaronic effect that can also easily by accounted for, caused by emission into the phonon sidebands, which is discussed later.

is the phonon coupling term corresponding to exciton-phonon scattering, with $N = \sigma^+\sigma^-$ and

$$\tilde{N}(t-\tau,t) = U^\dagger(t-\tau,t)NU(t-\tau,t), \tag{6.20}$$

where $U(t,t_0)$ evolves the system from t_0 to t.

Making a Markov approximation, the coupling term is

$$\mathbb{L}_{\mathrm{W}}\rho = \int_0^\infty d\tau\Gamma_{\mathrm{W}}(\tau)\left(\tilde{N}(-\tau)\rho N - N\tilde{N}(-\tau)\rho\right) + \mathrm{H.c.} \tag{6.21}$$

with

$$\tilde{N}(-\tau) = e^{-iH_{\mathrm{S}}^x(t)\tau/\hbar}Ne^{iH_{\mathrm{S}}^x(t)\tau/\hbar}, \tag{6.22}$$

and

$$\Gamma_{\mathrm{W}}(\tau) = \int_0^\infty d\omega J_P(\omega)\left[\coth\left(\frac{\hbar\omega}{2k_BT}\right)\cos(\omega\tau) - i\sin(\omega\tau)\right], \tag{6.23}$$

where T is the temperature and

$$J_P(\omega) = \alpha_{\mathrm{ph}}\omega^3\exp\left[-\frac{\omega^2}{2\omega_b^2}\right], \tag{6.24}$$

is the phonon spectral function. The parameters α_{ph} and ω_b are the exciton-phonon coupling strength and the cutoff frequency, respectively, which depend on the physical properties of the qubit. For an InGaAs/GaAs QD, such as those in [304], these parameters are $\alpha_{\mathrm{ph}} = 0.03\mathrm{ps}^2$ and $\hbar\omega_b = 0.9\mathrm{meV}$. This form of the spectral function represents bulk LA phonons in the continuum limit of the phonon spectral modes for a deformational potential in the QD lattice material [325]. This spectral form has been well used to explain phonon effects in various QD experiments [144, 294, 317, 326–328].

Following the methods of [313], this electron-phonon coupling can be mapped onto a polaron shift of the qubit frequency $\Delta_P = \alpha_{\mathrm{ph}}\omega_b^3\sqrt{\pi/2}$ and two phonon-mediated Lindblad operators, one equivalent to pure dephasing with rate $\gamma'_{\mathrm{eff}}(t)/2$ and operator $\sigma^+\sigma^-$ and another *incoherent* excitation process which acts as phonon mediated excitation with rate $\Gamma^+(t)$ and operator σ^+. Importantly, both of these rates are a function of temperature. Specifically, these phonon-induced rates are given by

$$\gamma'_{\mathrm{eff}}(t) = \pi\left(\frac{\varepsilon'(t)}{\varepsilon'_R(t)}\right)^2 J_P(\varepsilon'_R(t))\coth\left(\frac{\hbar\varepsilon'_R(t)}{2k_BT}\right), \tag{6.25}$$

$$\Gamma^+(t) = \frac{\pi}{4}\frac{|\varepsilon'(t)|}{\varepsilon'_R(t)}J_P(\varepsilon'_R(t)), \tag{6.26}$$

where $\varepsilon'_R(t) = \sqrt{\varepsilon'(t)^2 + \Delta^2}$ ($\Delta = \omega_0 - \omega_L$). Note the absolute value in Eq. (6.26) is included to ensure a positive rate at all times as some of the driving schemes have negative (and real) instantaneous Rabi frequencies. These phonon rates are time-dependent and their value depends on the strength and profile of the pump fields.

By including the pump-induced phonon coupling, this introduces an inherent maximum to the indistinguishability that can be achieved. This maximum is due to the photon emission into the phonon sideband rather than the sharp zero phonon line and is determined by $\langle B \rangle^4$ [285], where $\langle B \rangle$ is the Franck-Condon factor:

$$\langle B \rangle = \exp\left[-0.5 \int_0^\infty d\omega \frac{J_P(\omega)}{\omega^2} \coth\left(\frac{\hbar\omega}{2k_B T}\right)\right]. \tag{6.27}$$

For the parameter choices above, this gives $\langle B \rangle = 0.96$ and a resulting cap on the indistinguishability of 0.849. This can be improved through spectral filtering of the qubit emission but can result in a decrease of the efficiency of the SPS [285]. To get the clearest comparison between excitation schemes, we do not account for any specific filtering (which is typically used in experiments) and the indistinguishability limit dictated by $\langle B \rangle$, but highlight that any realization of these schemes will be limited by this effect.

6.2.4 Simulation Model

To simulate these systems and calculate their performance as a single photon source we use quantum trajectory theory [176–178], a stochastic method which evolves the system ket vector with a non-Hermitian Hamiltonian augmented by quantum jumps. Using quantum trajectories has some significant numerical advantages when calculating the single photon source figures of merit as we now describe.

Conventionally, open system quantum optics simulations are done using a master equation approach. For a pulsed system, calculating $g^{(2)}(0)$ and $\mathcal{I}$ with the master equation requires simulating the full two time correlation functions $g^{(1)}(t, t')$ and $g^{(2)}(t, t')$. These simulations scale as $D^2 \cdot T^2$ where D is the Hilbert space dimension and T is the required number of time steps for the system to complete relaxation after the pulse.

In the quantum trajectory picture, we use the natural link between the trajectories and experimental realizations of the system to simulate Hanbury Brown and Twiss (HBT) and Hong-Ou-Mandel (HOM) interferometers [271]. In contrast, the HBT simulations scale as $N \cdot D \cdot T$ and the HOM simulations scale as $N \cdot D^2 \cdot T$ where N is the number of trajectories required to converge to the ensemble average. Typically this is on the

order of a few thousand trajectories, while the required time steps can be on the order of thousands to hundreds of thousands depending on the time dynamics that must be resolved. Furthermore, each simulation is independent and so parallel computing can be used to further reduce the computation time by up to a factor of N (depending on the number of computing nodes available).

6.3 Numerical Results

To compare the performance of the three driving schemes, we simulate the common QD system driven by each scheme for single photon emission. We quantify the SPS performance of the system through three figures of merit; the efficiency, η, of single photon emission, the coherence, $g^{(2)}(0)$, of the emitted photons, and the indistinguishability, $\mathcal{I}$, of the emitted photons.

In this section, we use $\gamma/2\pi = 1$ GHz ($\hbar\gamma \approx 4.1$ μeV) similar to the QD emission rate in [235], but note that all of the results are sensitive to the pulse parameters relative to γ. For example, the rate of two photon emission, a detriment to perfect single photon generation, is dependent on the effective pulse width of the pumping scheme relative to γ. Further, the full width half maximum of the qubit emission spectrum (shown in red in Fig. 6.2) is γ and thus the overlap between the qubit emission and the laser spectrum also depends on this value. An important feature of each of these off-resonant pumping schemes is that they avoid spectral overlap with the qubit emission spectrum. To quantify this, we define an overlap measure,

$$\mathcal{O} = \frac{\int |\varepsilon'_{\text{norm}}(\omega)|^2 S(\omega) d\omega}{\int S(\omega) d\omega}, \tag{6.28}$$

which describes the overlap between the spectral function of the (normalized) input driving spectrum, $|\varepsilon'_{\text{norm}}(\omega)|^2$, and the qubit emission spectrum, $S(\omega)$.

The parameters for each pulse that we choose are intended to most fairly compare the schemes using parameters proposed in the original papers, with similar pulse durations for each scheme. The parameters chosen are listed in Table 6.1. Two parameters sets are shown for the dichromatic pumping scheme because the first set of parameters taken from the original paper [142] proposes a much larger pulse width than in either the NARP or SUPER schemes.

We first compare the drive profiles in time and frequency for the four driving setups in Fig. 6.2(a)-(h). In the time domain (a - d), the SUPER scheme (d) and the short

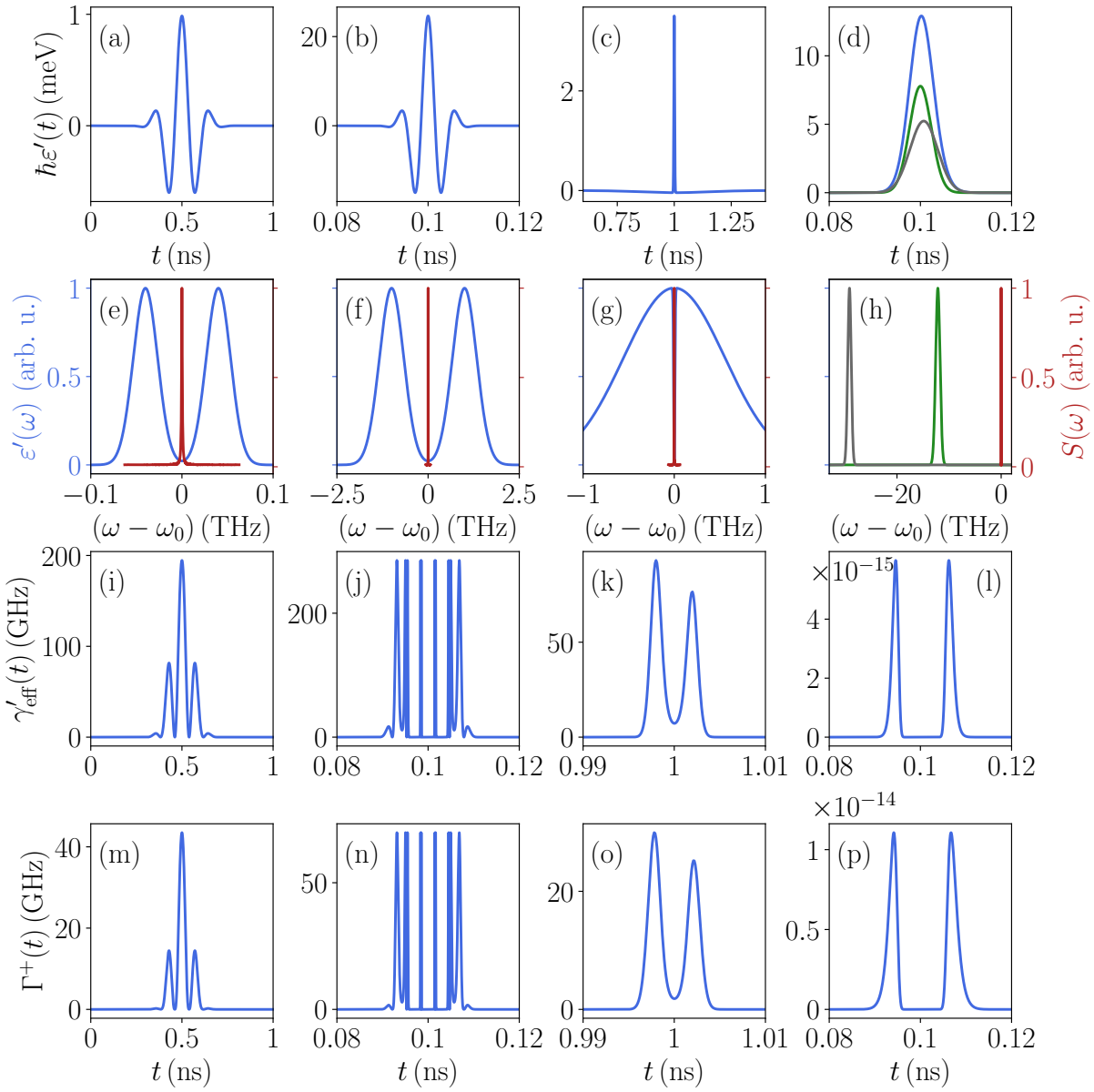

Figure 6.2: The laser profiles and resulting phonon rates for the four driving schemes in each column, left to right: long dichromatic pulse, short dichromatic pulse, NARP, and SUPER. By row, (a)-(d) the time domain profile of the pulse, (e)-(h) the spectral profile (in blue) with the qubit emission spectrum (in red), (i)-(l) the phonon-induced dephasing rate, and (m)-(p) the phonon-induced excitation rate.

Scheme	$\hbar\Omega_0$ (meV)	t_p (ps)	φ	$\hbar\Delta(t=0)$ (meV)	$\hbar\delta$ (μeV)	Other Parameters
Long Dichromatic	0.314	74.96	0	N/A	26.3	N/A
Short Dichromatic	7.842	3.00	0	N/A	658.2	N/A
NARP	3.547	1.80	N/A	0	5.3	$\alpha = -1.111\,\mathrm{ps}^{-2}$
SUPER	$\Omega_1 : 7.785$ $\Omega_2 : 5.235$	$t_{\mathrm{p},1} : 2.40$ $t_{\mathrm{p},2} : 3.04$	0	$\Delta_1 : 8.00$ $\Delta_2 : 19.163$	N/A	$\tau = -0.73$ ps

Table 6.1: Pulse profile parameters for the four driving setups.

dichromatic pulse (b) both have very high instantaneous Rabi frequencies during the pulse. This yields very fast time dynamics in the qubit evolution, while the NARP (c) and long dichromatic pulse (a) have instantaneous Rabi frequencies about an order of magnitude lower. In the frequency domain (e - h), all of the pulses avoid significant overlap with the qubit emission spectrum, however some achieve this better than others. The SUPER scheme (h) is best for reducing spectral overlap, as the detuning of the two composite pulses results in no overlap between the spectra, $\mathcal{O} = 0$. The dichromatic scheme pulse spectra in (e) and (f) may look identical, but the shorter pulse width in (b) causes the two pulses in (f) to be an order of magnitude wider than in (e). This results in an overlap of $\mathcal{O} = 0.0049$ for the longer pulse in (e) and an overlap of $\mathcal{O} = 0.0005$ for the shorter pulse in (f). This is non-zero because the tails of the detuned Gaussians still cover the frequency of the qubit. Lastly the NARP pulse (g) has a very broad spectrum so it looks like it overlaps with the qubit emission, but the sharp magnitude filter, $A(\omega)$, cuts out the portion of the spectra about the qubit emission and has an overlap of $\mathcal{O} = 0.0263$.

For the qubit model considered in this work, there are three mechanisms which lead to imperfect single photon source emission. The first is multiphoton emission that occurs during the excitation process, i.e., the qubit emits before the laser has finished driving it to the excited state. This is primarily mitigated through a shorter pulse duration and is why we included a shorter version of the dichromatic pulse to have comparable rates of multiphoton emission for the three schemes.

The second and third are phonon-induced pure dephasing and excitation, with rates given in Eqs. (6.25) and (6.26), which (with respect to the driving pulse) are determined by the strength and detuning of the pulse; they are calculated in the time domain for each of the four pulses in Figs. 6.2(i)-(p). High instantaneous rates are seen for the short dichromatic pulse, but they are interspersed with very low rates. This happens because the high Rabi frequency surpasses the cutoff frequency of the phonon spectrum and where this is true the $\exp[-(\varepsilon_\mathrm{R}')^2/2\omega_\mathrm{b}^2]$ term suppresses the influence of phonons. This also occurs for the SUPER scheme, but the extremely detuned pulses cause the phonon rates to be essentially zero ($\propto 10^{-14}$ GHz) and phonons have very little effect on this driving scheme.

The longer dichromatic pulse also has phonon rates > 100 GHz and because of the longer interaction time this can completely spoil the excited state preparation as we will show. By using a positive chirp, the higher side of the phonon rates for the NARP scheme are before excitation has begun to occur in the excitation scheme which improves the SPS performance. Further, as it passes through the peak of the pulse, the phonon rates drop off significantly, avoiding dissipation during the most sensitive part of the excitation process.

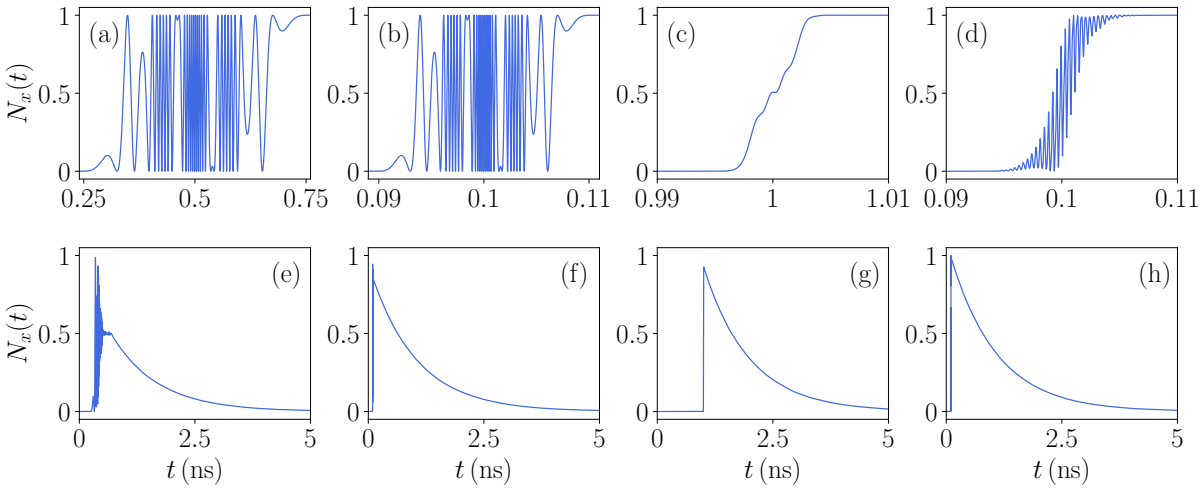

Figure 6.3: The population dynamics ($N_x(t) = \langle \sigma^+ \sigma^-(t) \rangle$) without dissipation in the first row, and with waveguide output and phonon coupling in the second row. Each column is a particular driving scheme: (a)-(b) long dichromatic pulse, (c)-(d) short dichromatic pulse, (e)-(f) NARP, and (g)-(h) SUPER.

Next in Fig. 6.3, we show how the population for each scheme evolves without dissipation and with phonon coupling. In the first row, without dissipation, all schemes successfully reach $> 99.96\%$ population inversion. Notably, only the dichromatic scheme does this to exactly 100% because it analytically satisfies the area theorem. Both the NARP and SUPER schemes are threshold approaches and only achieve near perfect inversion but do not exactly reach the excited state. In the second row, the population dynamics including both decay into the waveguide and phonon coupling are shown for each scheme. The SPS figures of merit for each pumping scheme are given in Table 6.2. As expected from the analysis of the phonon rates, the long dichromatic pulse loses coherence due to the high rate of pure dephasing and results in a maximum population of 0.5 before the pulse has completed. This severely limits its usefulness as a single photon source as the efficiency of the source is capped at 0.5, with associated hits to its coherence and indistinguishability. In contrast, the short dichromatic pulse avoids this large phonon influence and the dynam-

Scheme	η	$g^{(2)}(0)$	$\mathcal{I}$
Long Dichromatic	0.4948	0.4619	0.5850
Short Dichromatic	0.8519	0.0074	0.9889
NARP	0.9302	0.0036	0.9929
SUPER	0.9890	0.0012	0.9987

Table 6.2: SPS figures of merit for the four population dynamics with phonon coupling ($\alpha_{\text{ph}} = 0.03$ ps^2 and $\hbar\omega_b = 0.9$ meV) in the second row of Fig. 6.3.

ics show a promising single photon source. It does take a hit to its efficiency ($\eta = 0.8519$) but has very good coherence ($g^{(2)}(0) = 0.0074$) and indistinguishability ($\mathcal{I} = 0.9889$).

Both the NARP and SUPER schemes result in near perfect single photons with $g^{(2)}(0) = 0.0036$ and $\mathcal{I} = 0.9929$ for the NARP scheme and $g^{(2)}(0) = 0.0012$ and $\mathcal{I} = 0.9987$ for the SUPER scheme. The main differentiator between the two is their efficiency which are both high but is better for the SUPER scheme ($\eta = 0.9890$) than the NARP scheme ($\eta = 0.9302$). For near perfect single photons, it is surprising that the efficiency takes such a hit in the NARP case. The phonon-induced excitation events are the culprit for this behaviour (and also for the outsize hit to the efficiency in the short dichromatic pulse as well). Before the driving pulse begins to coherently excite the dot, there is a peak in the phonon-induced excitation rate. If such an excitation event occurs, the qubit begins in the excited state as the driving pulse arrives and the pulse acts to de-excite the qubit from the excited state to the ground state, resulting in no emission. This gives a pulse for which no photon is emitted (decreasing the efficiency) but does not appear in the HBT or HOM interferometric histograms which are used to calculate coherence and indistinguishability.

It is also interesting to compare the SPS performance of the dichromatic and NARP schemes as their spectral gap increases (which decreases the overlap function). For the dichromatic pulses the spectral gap is determined by the value of δt_{p}, and for the NARP pulse it is determined by δ. The SPS performance vs. the spectral gap size is shown for the long dichromatic pulse in Fig. 6.4 and for the short dichromatic pulse in Fig. 6.5. Similar changes in the performance are seen in both cases, with a larger hit to performance being seen in the case of the longer dichromatic pulses. All three figures of merit; efficiency, coherence, and indistinguishability decrease as the detuning between the two pulses increases both with and without phonon coupling. As the detuning increases, the duration of the total pulse duration also increases, in turn causing an increase in multiphoton emission. This is the cause of the performance decrease without phonons. Additionally, as the detuning increases, the amplitude of the laser pulse also increases, leading to larger rates of phonon dephasing and excitation which cause the additional impact in performance.

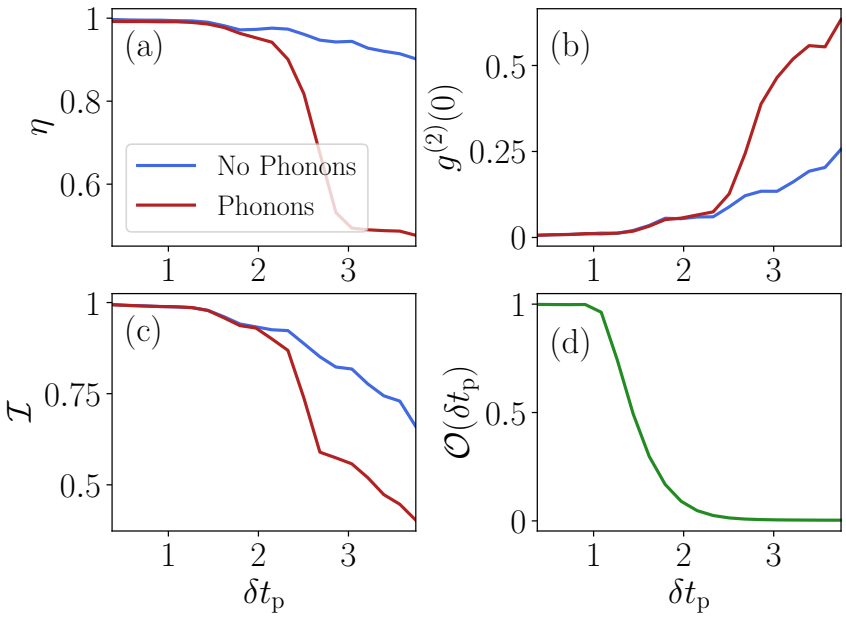

Figure 6.4: (a)-(c) SPS performance (through the (a) efficiency, (b) coherence, and (c) indistinguishability) as a function of the spectral separation of the two pulses for the long dichromatic pulse. The overlap function for each separation is in (d). Note that the overlap results in (d) are only dependent on the pulse form.

Figure 6.6 shows the SPS performance as the amplitude mask of the NARP pulse widens. The most important feature here is that as the mask widens, there is no significant impact on the performance in either of the three figures of merit. Aside from the hit to efficiency from phonon-induced excitation, one can use an amplitude mask as wide as desired to avoid spectral overlap with no resulting loss in performance. This can be experimentally useful as the pulse scheme will continue to work within a large margin of error on the laser parameters. Also, by allowing for very wide filters, one can avoid driving any additional resonances that may be present in the qubit.

It is important to note that the laser parameters for the SUPER scheme are not analytically derived. Rather the parameters of the first laser are fixed and then a scan of the second laser parameters are used to find parameter sets which satisfy inversion. Here, we compare the SPS performance for the parameter space around the SUPER laser parameters for the second pulse used in the previous analysis. In Fig. 6.7(a)-(c), we scan the parameter space of the second laser's envelope by varying by 30% in the amplitude and pulse width up to 30% (so the shown parameter space is $[0.7\Omega_2, 1.3\Omega_2]$ and $[0.7t_{p,2}, 1.3t_{p,2}]$).

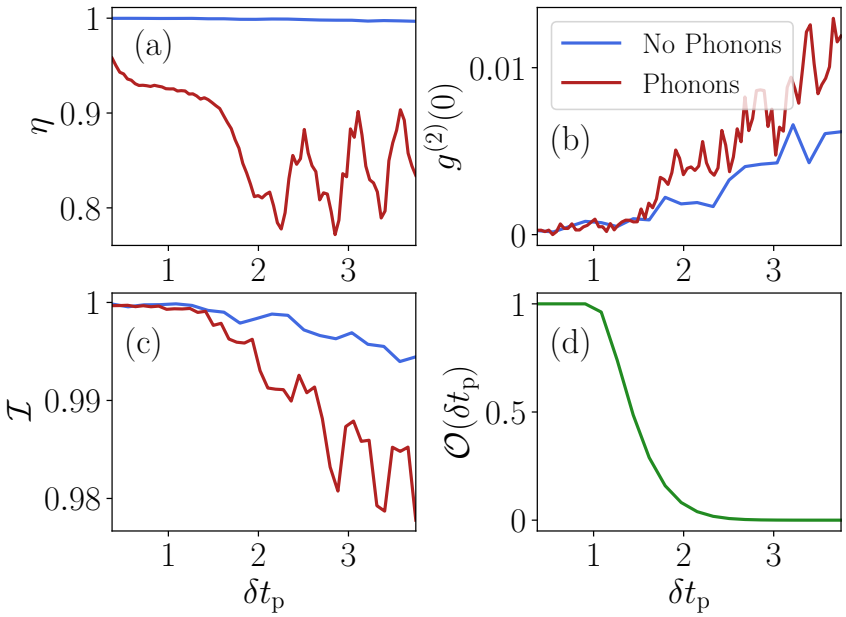

Figure 6.5: (a)-(c) SPS performance (through the (a) efficiency, (b) coherence, and (c) indistinguishability) as a function of the spectral separation of the two pulses for the short dichromatic pulse. The overlap function for each separation is in (d). Each data point in (a)-(c) is an average of 50,000 stochastic trajectories with very low event rates which leads to the noise in the data.

In (b) and (c), the coherence and indistinguishability show no underlying pattern as either parameter changes showing no significant impact on the performance. However, in the efficiency, there is a hit as the second laser varies its envelope. There is a small change as $t_{p,2}$ increases or decreases, with the efficiency only dropping to $\eta = 0.973$ after 30% decrease in $t_{p,2}$. A much larger effect appears as Ω_2 changes with a 5% increase in amplitude results in an efficiency of $\eta = 0.96$ and a 20% increase results in an efficiency of $\eta = 0.718$.

In Fig. 6.7(d)-(f), the detuning of the second pulse, Δ_2, is varied up to 2%, a shift of 0.38 meV. When the detuning is shifted, the efficiency quickly falls off to <0.9 after a shift of only 0.19 meV, while the coherence and indistinguishability still remain largely unaffected. This is because if the detuning is incorrect, the fast oscillations will no longer result in the beating driving the TLS to the excited state, but rather it is out of rhythm with the Rabi oscillations of the first laser and inversion fails. This however, does not impact the coherence and indistinguishability as no additional multiphoton or dephasing events are occurring to spoil these figures of merit.

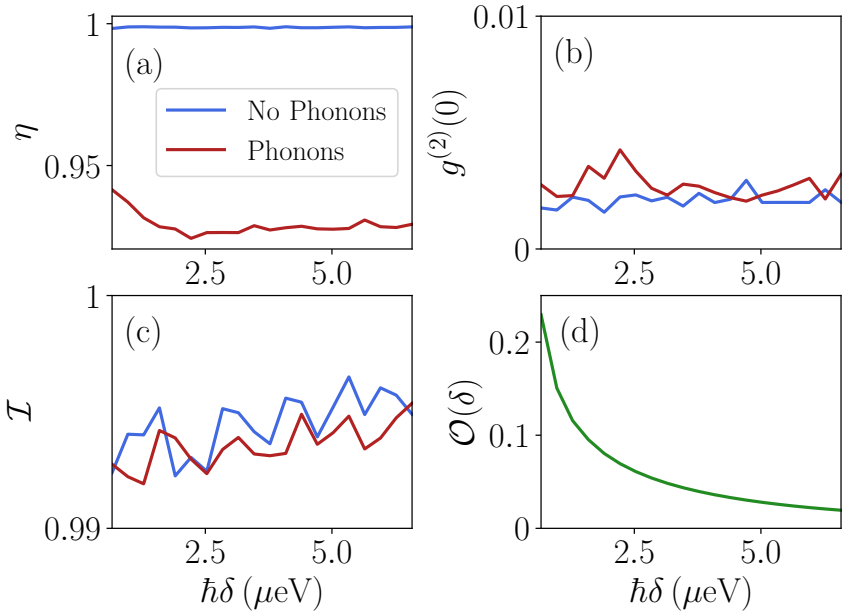

Figure 6.6: (a)-(c) SPS performance (through the (a) efficiency, (b) coherence, and (c) indistinguishability) as a function of the spectral filter width in NARP. The overlap function for each separation is in (d). Each data point in (a)-(c) is an average of 50,000 stochastic trajectories with very low event rates which leads to the noise in the data.

6.4 Conclusions

In summary, we have compared the SPS performance through the efficiency, coherence, and indistinguishability of the emitted photons from three different off resonant excitation schemes driving a realistic waveguide QED qubit model. While the dichromatic scheme can achieve reasonable success as a single photon source, its performance falls as the spectral spacing between the pulses widens (reducing the spectral overlap between qubit and laser) and phonon dissipation begins to negatively impact the SPS performance.

Both the NARP and SUPER schemes achieve near perfect coherence and indistinguishability. While both achieve excellent efficiency, the SUPER scheme is slightly ahead of the NARP scheme in this figure of merit. The NARP scheme is also quite robust against any variance in the driving parameters and can have the spectral filter broadened to any needed width with little to no impact of the SPS performance. The SUPER scheme is quite sensitive to the parameters of its constituent lasers, with a 2% change in the detuning of the second laser resulting in a hit of over 50% to the efficiency and changes of up to 5% in

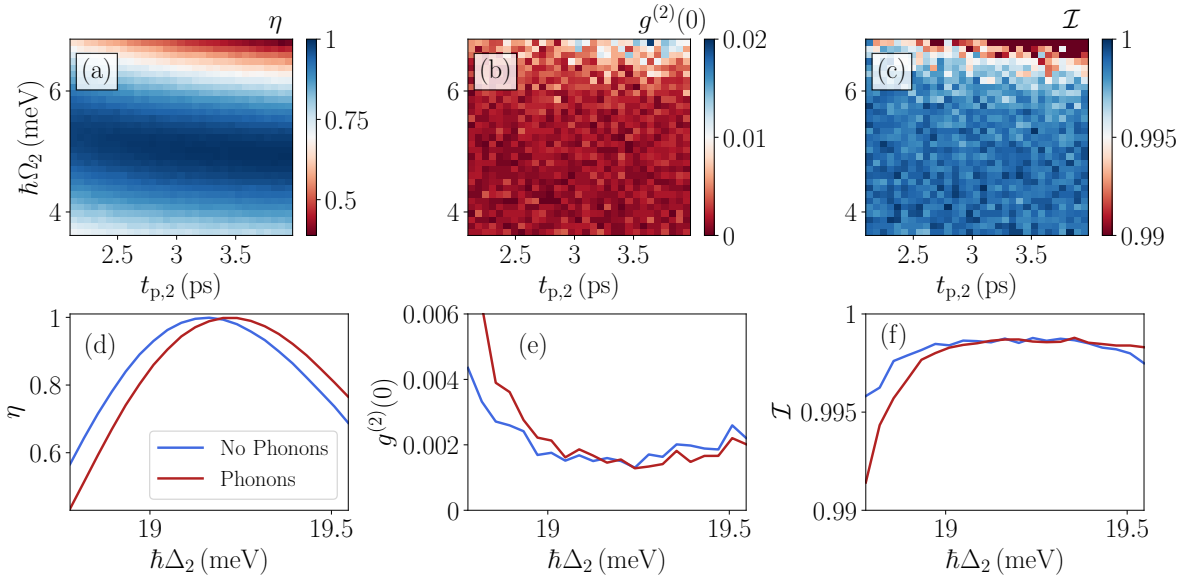

Figure 6.7: (a)-(c) SPS performance as a function of the amplitude (Ω_2) and the pulse width ($t_{p,2}$) of the second laser in the SUPER scheme. Each parameter is varied to a maximum of 30%. (d)-(f) SPS performance as a function of the second laser detuning.

the amplitude and width causing a 3% decrease in efficiency.

These pulse schemes allow efficient SPS preparation without the need for polarization filtering allowing for the complete single photon pulse to be used rather than a single polarization. Further work can be done to optimize these schemes within the free parameters of each scheme, or beyond that, inverse design techniques can be used that could create a pulse with better and more robust SPS performance while avoiding overlap with the qubit emission spectrum.

6.5 Acknowledgements

This work was supported by the Natural Sciences and Engineering Research Council of Canada (NSERC), the Canadian Foundation for Innovation (CFI), the National Research Council of Canada (NRC), Queen's University, Canada, and the University of Ottawa.

Chapter 7

Conclusions

In this thesis, we have presented four manuscripts, two published and two submitted, on quantum light emission in waveguide-QED systems. We have developed the quantum trajectory discretized waveguide (QTDW) model to calculate two-time correlation functions and simulate two interferometers for calculation of output spectrum, photon statistics, and single photon source figures of merit. To our knowledge, the QTDW model is the best for practical simulations including dissipation from the waveguide-QED system, as other approaches such as matrix product states require complex adjustments to simulate these systems. In particular, we have shown how time-delayed coherent feedback introduces new physics in resonance fluorescence systems. This includes using the phase change from the feedback round trip to tune the emission from bunched to antibunched light and to add new resonances to the Mollow triplet spectrum characteristic of resonance fluorescence. This is supported by experimental results confirming the non-Markovian nature of these simulations and additionally showing how non-Markovian effects are present even in the linear regime. We also show how coherent feedback can be used to improve single photon performance. The time delay of the feedback is crucial to simultaneously lowering the multiphoton emission events and the impact of the additional dissipation channels (out of plane emission and pure dephasing) that are present in a realistic two level system model. Lastly, we evaluate the performance of three different off-resonant pulse preparation schemes used in a common single photon source model. This includes a weak coupling phonon model to compare the three schemes in a realistic model system.

7.1 Suggestions for Future Work

Our work in this thesis has focused on using the QTDW model for a single two level system with a time-delayed coherent feedback. There are many avenues for further research through continued development and refinement of this technique and model system. First, as mentioned in the computational methods section, a numerical paper which explains our computational approach along with open source publication of the code could be useful to the broader quantum optics community. To our knowledge, we are one of the only groups calculating two-time correlation functions with the waveguide included at the non-bath level in a quantum trajectory framework which can be a key observable in some theoretical problems. Also, the intuitive nature of the QTDW model leads it to be much more approachable than techniques such as matrix product states for simulating coherent feedback, so open source code of the QTDW model may be appreciated by the community for quick simulation of coherent feedback problems.

Continued collaboration between our theoretical group and experimental groups interested in coherent feedback is also an excellent opportunity for future work. Of course, this is most natural with our superconducting circuit partners that did the experiments in Ch. 4. Through discussions with them, they hope to continue running coherent feedback experiments particularly looking at more applications of resonance fluorescence with coherent feedback including using detuned driving pumps or switching to pulsed excitation. It would also be interesting to collaborate with an experimental group working in the optical regime with waveguide-QED systems and emitters such as quantum dots. In this regime the wavelengths are much shorter so feedback loops can be very small compared to the superconducting circuits, but the location of the emitter must be finely manipulated to achieve the desired round trip phase change.

Beyond the two previous directions for future work, we can also look towards expanding the system we model to be more complex, particularly in three key areas. In this thesis we restricted the coupled quantum emitter to be a single two level system. This could be expanded to include additional energy levels to model a more specific emitter, such as including the biexcition levels in a quantum dot, or the many additional energy transitions in a coupled trapped atom. Typically when working with these more complex emitters, there is an associated scheme for generating quantum light beyond single photon emission. This could be using the energy levels to trap a photon in a dark state for quantum memory applications, or using a pulse preparation scheme to generate cluster states. These states of quantum light could also be investigated to see how coherent feedback could improve their generation. Lastly, the QTDW model assumes linear dispersion in the waveguide for the bins to all move forward one time step. This could be expanded to include some

nonlinear dispersion effects to see how coherent feedback changes in this regime. This would involve additional coupling between bins in the waveguide and could be an interesting computational and theoretical problem to take on.

The input excitation and photon detection could also be areas for further work with the QTDW model. With the expansion of the QTDW model to include waveguide inputs in Ch. 4, this could be further developed to include non-classical light excitation into the system, for example a one or two photon Fock state excitation. This has already been done in the waveguide-QED regime [55], but does not include additional dissipation channels or coherent feedback. The detection of photons leaving waveguide is also treated as a strong measurement (known as heterodyne detection), if there is a photon leaving the waveguide it is always detected. Quantum trajectory theory has also been developed using weak measurements (known as homodyne detection) for the quantum jump channels. Weak measurements could also be implemented in the QTDW model during the photon detection steps. When photons are detected in a weak measurement scheme, the discontinuous jump in observables is not as abrupt. This could give numerical advantages by lowering the required number of trajectories for convergence by avoiding the large discontinuities of an individual trajectory in the current heterodyne detection of the QTDW model.

The final area of suggested future work (though this is certainly not a comprehensive list) is to use inverse design techniques with the QTDW model to maximize the performance of the pulsed sources in Chs. 5 and 6. In Ch. 5 a coherent π-pulse was used for the state preparation, and in Ch. 6 we followed the off-resonant schemes as outlined in the papers that presented them. It would be interesting to see how (or if) inverse design techniques could further improve upon these pulse shapes for better single photon source performance. Beyond this, if we look toward simulation of other types of quantum light sources, inverse design could also help us there to better produce the states of light.

References

[1]J. P. Dowling and G. J. Milburn, "Quantum technology: the second quantum revolution", Philosophical Transactions of the Royal Society of London. Series A: Mathematical, Physical and Engineering Sciences **361**, 1655–1674 (2003).

[2]N. Bohr, "I. On the constitution of atoms and molecules", The London, Edinburgh, and Dublin Philosophical Magazine and Journal of Science **26**, 1–25 (1913).

[3]A. Einstein, "The Quantum Theory of Radiation", Physikalische Zeitschrift **18** (1917).

[4]E. Schrödinger, "An Undulatory Theory of the Mechanics of Atoms and Molecules", The Physical Review **28**, 1049–1070 (1926).

[5]W. Heisenberg, "(Translated from German): The Actual Content of Quantum Theoretical Kinematics and Mechanics", Zeitschrift für Physik **43**, 172–198 (1927).

[6]H.-S. Zhong et al., "Quantum computational advantage using photons", Science **370**, 1460–1463 (2020).

[7]L. S. Madsen et al., "Quantum computational advantage with a programmable photonic processor", Nature **606**, 75–81 (2022).

[8]Y. Li et al., "Microsatellite-based real-time quantum key distribution", Nature **640**, 47–54 (2025).

[9]J. Aasi et al., "Enhanced sensitivity of the LIGO gravitational wave detector by using squeezed states of light", Nature Photonics **7**, 613–619 (2013).

[10]M. Tse et al., "Quantum-Enhanced Advanced LIGO Detectors in the Era of Gravitational-Wave Astronomy", Physical Review Letters **123**, 231107 (2019).

[11]A. D. Ludlow, M. M. Boyd, J. Ye, E. Peik, and P. Schmidt, "Optical atomic clocks", Reviews of Modern Physics **87**, 637–701 (2015).

[12]D. Subhi and R. Thabit, "Review of recent challenges and solutions in quantum internet", AIP Conference Proceedings **2804**, 020033 (2023).

[13]S. Innovation and E. D. Canada, *Canada's National Quantum Strategy*, Cat. No. Iu4-414/2022E-PDF, Ottawa, Canada, 2020.

[14]S. on Quantum Information Science, *National Quantum Initiative Supplement to the President's FY 2025 Budget*, Washington, DC, USA, 2024.

[15]X.-C. Yao, T.-X. Wang, P. Xu, H. Lu, G.-S. Pan, X.-H. Bao, C.-Z. Peng, C.-Y. Lu, Y.-A. Chen, and J.-W. Pan, "Observation of eight-photon entanglement", Nature Photonics **6**, 225–228 (2012).

[16]M. H. Appel et al., "Entangling a Hole Spin with a Time-Bin Photon: A Waveguide Approach for Quantum Dot Sources of Multiphoton Entanglement", Physical Review Letters **128**, 233602 (2022).

[17]V. S. Ferreira, G. Kim, A. Butler, H. Pichler, and O. Painter, "Deterministic generation of multidimensional photonic cluster states with a single quantum emitter", Nature Physics **20**, 865–870 (2024).

[18]R. Dahan, G. Baranes, A. Gorlach, R. Ruimy, N. Rivera, and I. Kaminer, "Creation of Optical Cat and GKP States Using Shaped Free Electrons", Physical Review X **13**, 031001 (2023).

[19]R. Ruimy, A. Karnieli, and I. Kaminer, "Free-electron quantum optics", Nature Physics **21**, 193–200 (2025).

[20]T. Wilk, A. Gaëtan, C. Evellin, J. Wolters, Y. Miroshnychenko, P. Grangier, and A. Browaeys, "Entanglement of Two Individual Neutral Atoms Using Rydberg Blockade", Physical Review Letters **104**, 010502 (2010).

[21]C. S. Adams, J. D. Pritchard, and J. P. Shaffer, "Rydberg atom quantum technologies", Journal of Physics B: Atomic, Molecular and Optical Physics **53**, 012002 (2019).

[22]D. B. Higginbottom, L. Slodička, G. Araneda, L. Lachman, R. Filip, M. Hennrich, and R. Blatt, "Pure single photons from a trapped atom source", New Journal of Physics **18**, 093038 (2016).

[23]C. Crocker, M. Lichtman, K. Sosnova, A. Carter, S. Scarano, and C. Monroe, "High purity single photons entangled with an atomic qubit", Optics Express **27**, 28143–28149 (2019).

[24]W. Wu, T. Zhang, and P.-X. Chen, "Quantum computing and simulation with trapped ions: On the path to the future", Fundamental Research **1**, 213–216 (2021).

[25]P. Kok and B. W. Lovett, "Qubits in the pink", Nature **444**, 49–49 (2006).

[26]H. Eisele, A. Lenz, R. Heitz, R. Timm, M. Dähne, Y. Temko, T. Suzuki, and K. Jacobi, "Change of InAs/GaAs quantum dot shape and composition during capping", Journal of Applied Physics **104**, 124301 (2008).

[27]K. Mnaymneh, D. Dalacu, J. McKee, J. Lapointe, S. Haffouz, J. F. Weber, D. B. Northeast, P. J. Poole, G. C. Aers, and R. L. Williams, "On-chip integration of single photon sources via evanescent coupling of tapered nanowires to SiN waveguides", Advanced Quantum Technologies **3**, 1900021 (2019).

[28]M. Gimeno-Segovia, T. Rudolph, and S. E. Economou, "Deterministic Generation of Large-Scale Entangled Photonic Cluster State from Interacting Solid State Emitters", Physical Review Letters **123**, 070501 (2019).

[29]P. Laferrière, E. Yeung, I. Miron, D. B. Northeast, S. Haffouz, J. Lapointe, M. Korkusinski, P. J. Poole, R. L. Williams, and D. Dalacu, "Unity yield of deterministically positioned quantum dot single photon sources", Scientific Reports **12**, 6376 (2022).

[30]A. D. White, R. Trivedi, K. Narayanan, and J. Vučković, "Enhancing Superradiance in Spectrally Inhomogeneous Cavity QED Systems with Dynamic Modulation", ACS Photonics **9**, 2467–2472 (2022).

[31]T. H. Maiman, "Stimulated Optical Radiation in Ruby", Nature **187**, 493–494 (1960).

[32]C. Gardiner and P. Zoller, *Quantum noise: a handbook of Markovian and non-Markovian quantum stochastic methods with applications to quantum optics* (Springer-Verlag, Berlin, 2000).

[33]A. Kiraz, M. Atatüre, and A. Imamoğlu, "Quantum-dot single-photon sources: Prospects for applications in linear optics quantum-information processing", Physical Review A **69**, 032305 (2004).

[34]S. Lloyd, "Coherent quantum feedback", Physical Review A **62**, 022108 (2000).

[35]K. Koshino and Y. Nakamura, "Control of the radiative level shift and linewidth of a superconducting artificial atom through a variable boundary condition", New Journal of Physics **14**, 043005 (2012).

[36]A. Carmele, J. Kabuss, F. Schulze, S. Reitzenstein, and A. Knorr, "Single Photon Delayed Feedback: A Way to Stabilize Intrinsic Quantum Cavity Electrodynamics", Physical Review Letters **110**, 013601 (2013).

[37]I.-C. Hoi, A. F. Kockum, L. Tornberg, A. Pourkabirian, G. Johansson, P. Delsing, and C. M. Wilson, "Probing the quantum vacuum with an artificial atom in front of a mirror", Nature Physics **11**, 1045–1049 (2015).

[38]H. Pichler and P. Zoller, "Photonic Circuits with Time Delays and Quantum Feedback", Physical Review Letters **116**, 093601 (2016).

[39]N. L. Naumann, L. Droenner, S. M. Hein, A. Carmele, A. Knorr, and J. Kabuss, "Feedback control of optomechanical systems", in Physics and Simulation of Optoelectronic Devices XXIV, Vol. 9742 (Mar. 2016), p. 974216.

[40]S. M. Hein, A. Carmele, and A. Knorr, "Creation and control of entanglement by time-delayed quantum-coherent feedback", in Physics and Simulation of Optoelectronic Devices XXIV, Vol. 9742 (Mar. 2016), p. 97420X.

[41]N. Német and S. Parkins, "Enhanced optical squeezing from a degenerate parametric amplifier via time-delayed coherent feedback", Physical Review A **94**, 023809 (2016).

[42]S. J. Whalen, A. L. Grimsmo, and H. J. Carmichael, "Open quantum systems with delayed coherent feedback", Quantum Science and Technology **2**, 044008 (2017).

[43]Y. Lu, N. L. Naumann, J. Cerrillo, Q. Zhao, A. Knorr, and A. Carmele, "Intensified antibunching via feedback-induced quantum interference", Physical Review A **95**, 063840 (2017).

[44]L. Droenner, N. L. Naumann, E. Schöll, A. Knorr, and A. Carmele, "Quantum Pyragas control: Selective-control of individual photon probabilities", Physical Review A **99**, 023840 (2019).

[45]N. Német, S. Parkins, A. Knorr, and A. Carmele, "Stabilizing quantum coherence against pure dephasing in the presence of time-delayed coherent feedback at finite temperature", Physical Review A **99**, 053809 (2019).

[46]S. Arranz Regidor, G. Crowder, H. Carmichael, and S. Hughes, "Modeling quantum light-matter interactions in waveguide QED with retardation, nonlinear interactions, and a time-delayed feedback: Matrix product states versus a space-discretized waveguide model", Physical Review Research **3**, 023030 (2021).

[47]K. Barkemeyer, M. Hohn, S. Reitzenstein, and A. Carmele, "Boosting energy-time entanglement using coherent time-delayed feedback", Physical Review A **103**, 062423 (2021).

[48]K. Barkemeyer, A. Knorr, and A. Carmele, "Heisenberg treatment of multiphoton pulses in waveguide QED with time-delayed feedback", Physical Review A **106**, 023708 (2022).

[49]F. Ciccarello, S. Lorenzo, V. Giovannetti, and G. M. Palma, "Quantum collision models: Open system dynamics from repeated interactions", Physics Reports **954**, 1–70 (2022).

[50]C. Gonzalez-Ballestero, E. Moreno, and F. J. Garcia-Vidal, "Generation, manipulation, and detection of two-qubit entanglement in waveguide QED", Physical Review A **89**, 042328 (2014).

[51]J. D. Hood, A. Goban, A. Asenjo-Garcia, M. Lu, S.-P. Yu, D. E. Chang, and H. J. Kimble, "Atom–atom interactions around the band edge of a photonic crystal waveguide", Proceedings of the National Academy of Sciences **113**, 10507–10512 (2016).

[52]A. S. Sheremet, M. I. Petrov, I. V. Iorsh, A. V. Poshakinskiy, and A. N. Poddubny, "Waveguide quantum electrodynamics: Collective radiance and photon-photon correlations", Reviews of Modern Physics **95**, 015002 (2023).

[53]S. Hughes, "Enhanced single-photon emission from quantum dots in photonic crystal waveguides and nanocavities", Optics Letters **29**, 2659 (2004).

[54]E. Rephaeli and S. Fan, "Stimulated Emission from a Single Excited Atom in a Waveguide", Physical Review Letters **108**, 143602 (2012).

[55]S. Arranz Regidor, A. Knorr, and S. Hughes, "Theory and simulations of few-photon Fock state pulses strongly interacting with a single qubit in a waveguide: Exact population dynamics and time-dependent spectra", Physical Review Research **7**, 023295 (2025).

[56]J.-T. Shen and S. Fan, "Strongly Correlated Two-Photon Transport in a One-Dimensional Waveguide Coupled to a Two-Level System", Physical Review Letters **98**, 153003 (2007).

[57]H. Zheng, D. J. Gauthier, and H. U. Baranger, "Waveguide QED: Many-body bound-state effects in coherent and Fock-state scattering from a two-level system", Physical Review A **82**, 063816 (2010).

[58]J. Román-Roche, E. Sánchez-Burillo, and D. Zueco, "Bound states in ultrastrong waveguide QED", Physical Review A **102**, 023702 (2020).

[59]K. Sinha, P. Meystre, E. A. Goldschmidt, F. K. Fatemi, S. Rolston, and P. Solano, "Non-Markovian Collective Emission from Macroscopically Separated Emitters", Physical Review Letters **124**, 043603 (2020).

[60]P. Solano, P. Barberis-Blostein, and K. Sinha, "Dissimilar collective decay and directional emission from two quantum emitters", Physical Review A **107**, 023723 (2023).

[61]J. Claudon, J. Bleuse, N. S. Malik, M. Bazin, P. Jaffrennou, N. Gregersen, C. Sauvan, P. Lalanne, and J.-M. Gérard, "A highly efficient single-photon source based on a quantum dot in a photonic nanowire", Nature Photonics **4**, 174–177 (2010).

[62]A. V. Akimov, A. Mukherjee, C. L. Yu, D. E. Chang, A. S. Zibrov, P. R. Hemmer, H. Park, and M. D. Lukin, "Generation of single optical plasmons in metallic nanowires coupled to quantum dots", Nature **450**, 402–406 (2007).

[63]N. V. Corzo, J. Raskop, A. Chandra, A. S. Sheremet, B. Gouraud, and J. Laurat, "Waveguide-coupled single collective excitation of atomic arrays", Nature **566**, 359–362 (2019).

[64]A. Blais, A. L. Grimsmo, S. Girvin, and A. Wallraff, "Circuit quantum electrodynamics", Reviews of Modern Physics **93**, 025005 (2021).

[65]N. A. Masluk, I. M. Pop, A. Kamal, Z. K. Minev, and M. H. Devoret, "Microwave Characterization of Josephson Junction Arrays: Implementing a Low Loss Superinductance", Physical Review Letters **109**, 137002 (2012).

[66]R. Kuzmin, N. Mehta, N. Grabon, R. Mencia, and V. E. Manucharyan, "Superstrong coupling in circuit quantum electrodynamics", npj Quantum Information **5**, 20 (2019).

[67]T. Maka, D. N. Chigrin, S. G. Romanov, and C. M. Sotomayor Torres, "Three dimensional photonic crystals in the visible regime", Progress in Electromagnetics Research **41**, 307–335 (2003).

[68]S. Hughes, "Coupled-Cavity QED Using Planar Photonic Crystals", Physical Review Letters **98**, 083603 (2007).

[69]L. Sapienza, H. Thyrrestrup, S. Stobbe, P. D. Garcia, S. Smolka, and P. Lodahl, "Cavity Quantum Electrodynamics with Anderson-Localized Modes", Science **327**, 1352–1355 (2010).

[70]A. H. Safavi-Naeini, T. P. M. Alegre, J. Chan, M. Eichenfield, M. Winger, Q. Lin, J. T. Hill, D. E. Chang, and O. Painter, "Electromagnetically induced transparency and slow light with optomechanics", Nature **472**, 69–73 (2011).

[71]R. J. Coles, D. M. Price, J. E. Dixon, B. Royall, E. Clarke, P. Kok, M. S. Skolnick, A. M. Fox, and M. N. Makhonin, "Chirality of nanophotonic waveguide with embedded quantum emitter for unidirectional spin transfer", Nature Communications **7**, 11183 (2016).

[72]P. Lodahl, S. Mahmoodian, S. Stobbe, A. Rauschenbeutel, P. Schneeweiss, J. Volz, H. Pichler, and P. Zoller, "Chiral quantum optics", Nature **541**, 473–480 (2017).

[73]S. Barik, A. Karasahin, C. Flower, T. Cai, H. Miyake, W. DeGottardi, M. Hafezi, and E. Waks, "A topological quantum optics interface", Science **359**, 666–668 (2018).

[74]D. Bose, M. W. Harrington, A. Isichenko, K. Liu, J. Wang, N. Chauhan, Z. L. Newman, and D. J. Blumenthal, "Anneal-free ultra-low loss silicon nitride integrated photonics", Light: Science & Applications **13**, 156 (2024).

[75]R. H. Dicke, "Coherence in Spontaneous Radiation Processes", Physical Review **93**, 99–110 (1954).

[76]D. Martin-Cano, H. R. Haakh, and N. Rotenberg, "Chiral Emission into Nanophotonic Resonators", ACS Photonics **6**, 961–966 (2019).

[77]M. J. Mehrabad, A. P. Foster, R. Dost, E. Clarke, P. K. Patil, A. M. Fox, M. S. Skolnick, and L. R. Wilson, "Chiral topological photonics with an embedded quantum emitter", Optica **7**, 1690–1696 (2020).

[78]N. V. Hauff, H. Le Jeannic, P. Lodahl, S. Hughes, and N. Rotenberg, "Chiral quantum optics in broken-symmetry and topological photonic crystal waveguides", Physical Review Research **4**, 023082 (2022).

[79]D. Roy, "Correlated few-photon transport in one-dimensional waveguides: Linear and nonlinear dispersions", Physical Review A **83**, 043823 (2011).

[80]E. Vetsch, D. Reitz, G. Sagué, R. Schmidt, S. T. Dawkins, and A. Rauschenbeutel, "Optical Interface Created by Laser-Cooled Atoms Trapped in the Evanescent Field Surrounding an Optical Nanofiber", Physical Review Letters **104**, 203603 (2010).

[81]A. Goban et al., "Atom–light interactions in photonic crystals", Nature Communications **5**, 3808 (2014).

[82]A. Bouscal et al., "Systematic design of a robust half-W1 photonic crystal waveguide for interfacing slow light and trapped cold atoms", New Journal of Physics **26**, 023026 (2024).

[83]C. Santori, D. Fattal, J. Vučković, G. S. Solomon, E. Waks, and Y. Yamamoto, "Submicrosecond correlations in photoluminescence from InAs quantum dots", Physical Review B **69**, 205324 (2004).

[84]K. Takemoto, Y. Sakuma, S. Hirose, T. Usuki, N. Yokoyama, T. Miyazawa, M. Takatsu, and Y. Arakawa, "Non-classical Photon Emission from a Single InAs/InP Quantum Dot in the 1.3-μm Optical-Fiber Band", Japanese Journal of Applied Physics **43**, L993 (2004).

[85]G. Cui and M. G. Raymer, "Emission spectra and quantum efficiency of single-photon sources in the cavity-QED strong-coupling regime", Physical Review A **73**, 053807 (2006).

[86]Y.-M. He, Y. He, Y.-J. Wei, D. Wu, M. Atatüre, C. Schneider, S. Höfling, M. Kamp, C.-Y. Lu, and J.-W. Pan, "On-demand semiconductor single-photon source with near-unity indistinguishability", Nature Nanotechnology **8**, 213–217 (2013).

[87]S. Hughes, S. Franke, C. Gustin, M. Kamandar Dezfouli, A. Knorr, and M. Richter, "Theory and Limits of On-Demand Single-Photon Sources Using Plasmonic Resonators: A Quantized Quasinormal Mode Approach", ACS Photonics **6**, 2168–2180 (2019).

[88]D. B. Northeast, D. Dalacu, J. F. Weber, J. Phoenix, J. Lapointe, G. C. Aers, P. J. Poole, and R. L. Williams, "Optical fibre-based single photon source using InAsP quantum dot nanowires and gradient-index lens collection", Scientific Reports **11**, 22878 (2021).

[89]P. Krantz, M. Kjaergaard, F. Yan, T. P. Orlando, S. Gustavsson, and W. D. Oliver, "A quantum engineer's guide to superconducting qubits", Applied Physics Reviews **6**, 021318 (2019).

[90]D. Englund, B. Shields, K. Rivoire, F. Hatami, J. Vučković, H. Park, and M. D. Lukin, "Deterministic Coupling of a Single Nitrogen Vacancy Center to a Photonic Crystal Cavity", Nano Letters **10**, 3922–3926 (2010).

[91]A. Sipahigil et al., "An integrated diamond nanophotonics platform for quantum-optical networks", Science **354**, 847–850 (2016).

[92]C. Bradac, W. Gao, J. Forneris, M. E. Trusheim, and I. Aharonovich, "Quantum nanophotonics with group IV defects in diamond", Nature Communications **10**, 5625 (2019).

[93]P. P. J. Schrinner, J. Olthaus, D. E. Reiter, and C. Schuck, "Integration of Diamond-Based Quantum Emitters with Nanophotonic Circuits", Nano Letters **20**, 8170–8177 (2020).

[94]S. Faez, P. Türschmann, H. R. Haakh, S. Götzinger, and V. Sandoghdar, "Coherent Interaction of Light and Single Molecules in a Dielectric Nanoguide", Physical Review Letters **113**, 213601 (2014).

[95]C. Toninelli et al., "Single organic molecules for photonic quantum technologies", Nature Materials **20**, 1615–1628 (2021).

[96]J. McFarlane, P. A. Dalgarno, B. D. Gerardot, R. H. Hadfield, R. J. Warburton, K. Karrai, A. Badolato, and P. M. Petroff, "Gigahertz bandwidth electrical control over a dark exciton-based memory bit in a single quantum dot", Applied Physics Letters **94**, 093113 (2009).

[97]J. Johansen, B. Julsgaard, S. Stobbe, J. M. Hvam, and P. Lodahl, "Probing long-lived dark excitons in self-assembled quantum dots", Physical Review B **81**, 081304 (2010).

[98]T. Heindel et al., "Accessing the dark exciton spin in deterministic quantum-dot microlenses", APL Photonics **2**, 121303 (2017).

[99]M. Holtkemper, G. F. Quinteiro, D. E. Reiter, and T. Kuhn, "Dark exciton preparation in a quantum dot by a longitudinal light field tuned to higher exciton states", Physical Review Research **3**, 013024 (2021).

[100]K. Brunner, "Sharp-Line Photoluminescence and Two-Photon Absorption of Zero-Dimensional Biexcitons in a GaAs/AlGaAs Structure", Physical Review Letters **73**, 1138–1141 (1994).

[101]M. E. Reimer, D. Dalacu, P. J. Poole, and R. L. Williams, "Biexciton binding energy control in site-selected quantum dots", Journal of Physics: Conference Series **210**, 012019 (2010).

[102]M. Müller, S. Bounouar, K. D. Jöns, M. Glässl, and P. Michler, "On-demand generation of indistinguishable polarization-entangled photon pairs", Nature Photonics **8**, 224–228 (2014).

[103]L. Schweickert et al., "On-demand generation of background-free single photons from a solid-state source", Applied Physics Letters **112**, 093106 (2018).

[104]W. Heitler, *The Quantum Theory of Radiation* (Clarendon Press, Oxford, 1954).

[105]C. Matthiesen, A. N. Vamivakas, and M. Atatüre, "Subnatural Linewidth Single Photons from a Quantum Dot", Physical Review Letters **108**, 093602 (2012).

[106]B. R. Mollow, "Power Spectrum of Light Scattered by Two-Level Systems", Physical Review **188**, 1969–1975 (1969).

[107]H. J. Kimble and L. Mandel, "Theory of resonance fluorescence", Physical Review A **13**, 2123–2144 (1976).

[108]A. Nick Vamivakas, Y. Zhao, C.-Y. Lu, and M. Atatüre, "Spin-resolved quantum-dot resonance fluorescence", Nature Physics **5**, 198–202 (2009).

[109]A. Ulhaq, S. Weiler, C. Roy, S. M. Ulrich, M. Jetter, S. Hughes, and P. Michler, "Detuning-dependent Mollow triplet of a coherently-driven single quantum dot", Optics Express **21**, 4382–4395 (2013).

[110]S. Kalliakos et al., "In-plane emission of indistinguishable photons generated by an integrated quantum emitter", Applied Physics Letters **104**, 221109 (2014).

[111]B. Da Lio et al., "A Pure and Indistinguishable Single-Photon Source at Telecommunication Wavelength", Advanced Quantum Technologies **5**, 2200006 (2022).

[112]S. Liu, C. Gustin, H. Liu, X. Li, Y. Yu, H. Ni, Z. Niu, S. Hughes, X. Wang, and J. Liu, "Dynamic resonance fluorescence in solid-state cavity quantum electrodynamics", Nature Photonics, 1–7 (2024).

[113]M. Gross, C. Fabre, P. Pillet, and S. Haroche, "Observation of Near-Infrared Dicke Superradiance on Cascading Transitions in Atomic Sodium", Physical Review Letters **36**, 1035–1038 (1976).

[114]A. Goban, C.-L. Hung, J. Hood, S.-P. Yu, J. Muniz, O. Painter, and H. Kimble, "Superradiance for Atoms Trapped along a Photonic Crystal Waveguide", Physical Review Letters **115**, 063601 (2015).

[115]F. Dinc and A. M. Brańczyk, "Non-Markovian super-superradiance in a linear chain of up to 100 qubits", Physical Review Research **1**, 032042 (2019).

[116]C. R. H. McRae, H. Wang, J. Gao, M. R. Vissers, T. Brecht, A. Dunsworth, D. P. Pappas, and J. Mutus, "Materials loss measurements using superconducting microwave resonators", Review of Scientific Instruments **91**, 091101 (2020).

[117]O. Astafiev, A. M. Zagoskin, A. A. Abdumalikov, Y. A. Pashkin, T. Yamamoto, K. Inomata, Y. Nakamura, and J. S. Tsai, "Resonance Fluorescence of a Single Artificial Atom", Science **327**, 840–843 (2010).

[118]S. Gasparinetti, J.-C. Besse, M. Pechal, R. D. Buijs, C. Eichler, H. J. Carmichael, and A. Wallraff, "Two-photon resonance fluorescence of a ladder-type atomic system", Physical Review A **100**, 033802 (2019).

[119]Y. Lu et al., "Characterizing decoherence rates of a superconducting qubit by direct microwave scattering", npj Quantum Information **7**, 35 (2021).

[120]A. F. van Loo, A. Fedorov, K. Lalumière, B. C. Sanders, A. Blais, and A. Wallraff, "Photon-Mediated Interactions Between Distant Artificial Atoms", Science **342**, 1494–1496 (2013).

[121]P. Wen et al., "Large Collective Lamb Shift of Two Distant Superconducting Artificial Atoms", Physical Review Letters **123**, 233602 (2019).

[122]B. Kannan et al., "On-demand directional microwave photon emission using waveguide quantum electrodynamics", Nature Physics **19**, 394–400 (2023).

[123]D. Magde and H. Mahr, "Study in Ammonium Dihydrogen Phosphate of Spontaneous Parametric Interaction Tunable from 4400 to 16 000 Å", Physical Review Letters **18**, Publisher: American Physical Society, 905–907 (1967).

[124]A. Eckstein, A. Christ, P. J. Mosley, and C. Silberhorn, "Highly Efficient Single-Pass Source of Pulsed Single-Mode Twin Beams of Light", Physical Review Letters **106**, 013603 (2011).

[125]E. Pomarico, B. Sanguinetti, T. Guerreiro, R. Thew, and H. Zbinden, "MHz rate and efficient synchronous heralding of single photons at telecom wavelengths", Optics Express **20**, 23846–23855 (2012).

[126]S. Sempere-Llagostera, G. S. Thekkadath, R. B. Patel, W. S. Kolthammer, and I. A. Walmsley, "Reducing $g^{(2)}(0)$ of a parametric down-conversion source via photon-number resolution with superconducting nanowire detectors", Optics Express **30**, 3138–3147 (2022).

[127]S. I. Davis et al., "Improved Heralded Single-Photon Source with a Photon-Number-Resolving Superconducting Nanowire Detector", Physical Review Applied **18**, 064007 (2022).

[128]A. Chopin, A. Barone, I. Ghorbel, S. Combrié, D. Bajoni, F. Raineri, M. Galli, and A. De Rossi, "Ultra-efficient generation of time-energy entangled photon pairs in an InGaP photonic crystal cavity", Communications Physics **6**, 77 (2023).

[129]A. Christ and C. Silberhorn, "Limits on the deterministic creation of pure single-photon states using parametric down-conversion", Physical Review A **85**, 023829 (2012).

[130]C. Eichler, D. Bozyigit, C. Lang, L. Steffen, J. Fink, and A. Wallraff, "Experimental State Tomography of Itinerant Single Microwave Photons", Physical Review Letters **106**, 220503 (2011).

[131]Y. Zhou, Z. Peng, Y. Horiuchi, O. Astafiev, and J. Tsai, "Tunable Microwave Single-Photon Source Based on Transmon Qubit with High Efficiency", Physical Review Applied **13**, 034007 (2020).

[132]D. Petrosyan and K. Mølmer, "Deterministic Free-Space Source of Single Photons Using Rydberg Atoms", Physical Review Letters **121**, 123605 (2018).

[133]S. Shi, B. Xu, K. Zhang, G.-S. Ye, D.-S. Xiang, Y. Liu, J. Wang, D. Su, and L. Li, "High-fidelity photonic quantum logic gate based on near-optimal Rydberg single-photon source", Nature Communications **13**, 4454 (2022).

[134]G. Grosso, H. Moon, B. Lienhard, S. Ali, D. K. Efetov, M. M. Furchi, P. Jarillo-Herrero, M. J. Ford, I. Aharonovich, and D. Englund, "Tunable and high-purity room temperature single-photon emission from atomic defects in hexagonal boron nitride", Nature Communications **8**, 705 (2017).

[135]Y.-J. Wei et al., "Deterministic and Robust Generation of Single Photons from a Single Quantum Dot with 99.5% Indistinguishability Using Adiabatic Rapid Passage", Nano Letters **14**, 6515–6519 (2014).

[136]X. Ding et al., "High-efficiency single-photon source above the loss-tolerant threshold for efficient linear optical quantum computing", Nature Photonics **19**, 387–391 (2025).

[137]Thorlabs Inc, *Correlated Photon-Pair Sources*, https://www.thorlabs.com/newgrouppage9.cfm?objectgroup_id=13675, Accessed: 2025-06-15.

[138]Quantum Computing Inc, *Entanglement Source*, https://quantumcomputinginc.com/products/commercial-products/entanglement-source, Accessed: 2025-06-15.

[139]Quandela, *The Power of Single Photons*, https://www.quandela.com/technology/the-power-of-single-photon-sources, Accessed: 2025-06-15.

[140]IonQ, *IonQ Forte*, https://ionq.com/quantum-systems/forte, Accessed: 2025-06-15.

[141]C. Gustin and S. Hughes, "Pulsed excitation dynamics in quantum-dot–cavity systems: limits to optimizing the fidelity of on-demand single-photon sources", Phys. Rev. B **98**, 045309 (2018).

[142]Y.-M. He et al., "Coherently driving a single quantum two-level system with dichromatic laser pulses", Nature Physics **15**, 941–946 (2019).

[143]T. K. Bracht, M. Cosacchi, T. Seidelmann, M. Cygorek, A. Vagov, V. M. Axt, T. Heindel, and D. E. Reiter, "Swing-Up of Quantum Emitter Population Using Detuned Pulses", PRX Quantum **2**, 040354 (2021).

[144]G. R. Wilbur, A. Binai-Motlagh, A. Clarke, A. Ramachandran, N. Milson, J. P. Healey, S. O'Neal, D. G. Deppe, and K. C. Hall, "Notch-filtered adiabatic rapid passage for optically driven quantum light sources", APL Photonics **7**, 111302 (2022).

[145]L. Ginés et al., "High Extraction Efficiency Source of Photon Pairs Based on a Quantum Dot Embedded in a Broadband Micropillar Cavity", Physical Review Letters **129**, 033601 (2022).

[146]D. R. Hjelme, A. R. Mickelson, and R. G. Beausoleil, "Semiconductor laser stabilization by external optical feedback", IEEE Journal of Quantum Electronics **27**, 352–372 (1991).

[147]G. F. Franklin, J. D. Powell, and A. Emami-Naeini, *Feedback control of dynamic systems* (Pearson, 2014).

[148]C. Cosentino and D. Bates, *Feedback control in systems biology* (CRC Press, 2011).

[149]A. Di Giovanni, M. Brunelli, and M. G. Genoni, "Unconditional mechanical squeezing via backaction-evading measurements and nonoptimal feedback control", Physical Review A **103**, 022614 (2021).

[150]J. Saiphet, S. Suwanna, A. R. R. Carvalho, and A. Chantasri, "Time-delayed quantum feedback and incomplete decoherence suppression with a no-knowledge measurement", Physical Review A **103**, 022208 (2021).

[151]A. Vepsäläinen et al., "Improving qubit coherence using closed-loop feedback", Nature Communications **13**, 1932 (2022).

[152]T. Grigoletto and F. Ticozzi, "Stabilization Via Feedback Switching for Quantum Stochastic Dynamics", IEEE Control Systems Letters **6**, 235–240 (2021).

[153]D. Ivanov, T. Ivanova, S. Caballero-Benitez, and I. Mekhov, "Feedback-Induced Quantum Phase Transitions Using Weak Measurements", Physical Review Letters **124**, 010603 (2020).

[154]G. Buonaiuto, F. Carollo, B. Olmos, and I. Lesanovsky, "Dynamical Phases and Quantum Correlations in an Emitter-Waveguide System with Feedback", Physical Review Letters **127**, 133601 (2021).

[155]S. Borah, B. Sarma, M. Kewming, G. J. Milburn, and J. Twamley, "Measurement-Based Feedback Quantum Control with Deep Reinforcement Learning for a Double-Well Nonlinear Potential", Physical Review Letters **127**, 190403 (2021).

[156]B. Annby-Andersson, F. Bakhshinezhad, D. Bhattacharyya, G. De Sousa, C. Jarzynski, P. Samuelsson, and P. P. Potts, "Quantum Fokker-Planck Master Equation for Continuous Feedback Control", Physical Review Letters **129**, 050401 (2022).

[157]N. Német, A. Carmele, S. Parkins, and A. Knorr, "Comparison between continuous- and discrete-mode coherent feedback for the Jaynes-Cummings model", Physical Review A **100**, 023805 (2019).

[158]H. J. Carmichael, *Statistical Methods in Quantum Optics 1: Master Equations and Fokker-Planck Equations* (Springer-Verlag Berlin Heidelberg, 1999).

[159]H. J. Carmichael, *Statistical Methods in Quantum Optics 2: Non-Classical Fields* (Springer-Verlag Berlin Heidelberg, 2008).

[160]P. W. Milonni and P. L. Knight, "Retardation in the resonant interaction of two identical atoms", Physical Review A **10**, 1096–1108 (1974).

[161]T. Tufarelli, F. Ciccarello, and M. S. Kim, "Dynamics of spontaneous emission in a single-end photonic waveguide", Physical Review A **87**, 013820 (2013).

[162]S. M. Hein, F. Schulze, A. Carmele, and A. Knorr, "Optical Feedback-Enhanced Photon Entanglement from a Biexciton Cascade", Physical Review Letters **113**, 027401 (2014).

[163]J. Kabuss, D. O. Krimer, S. Rotter, K. Stannigel, A. Knorr, and A. Carmele, "Analytical study of quantum-feedback-enhanced Rabi oscillations", Physical Review A **92**, 053801 (2015).

[164]M. Kraft, S. M. Hein, J. Lehnert, E. Schöll, S. Hughes, and A. Knorr, "Time-delayed quantum coherent Pyragas feedback control of photon squeezing in a degenerate parametric oscillator", Physical Review A **94**, 023806 (2016).

[165]K. Sinha, A. González-Tudela, Y. Lu, and P. Solano, "Collective radiation from distant emitters", Physical Review A **102**, 043718 (2020).

[166]A. Das, P. Solano, and K. Sinha, "Non-Markovian spontaneous emission in a tunable cavity formed by atomic mirrors", Physical Review A **112**, 043723 (2025).

[167]U. Dorner and P. Zoller, "Laser-driven atoms in half-cavities", Physical Review A **66**, 023816 (2002).

[168]A. L. Grimsmo, "Time-Delayed Quantum Feedback Control", Physical Review Letters **115**, 060402 (2015).

[169]P.-O. Guimond, M. Pletyukhov, H. Pichler, and P. Zoller, "Delayed coherent quantum feedback from a scattering theory and a matrix product state perspective", Quantum Science and Technology **2**, 044012 (2017).

[170]Y. Shi and E. Waks, "Deterministic generation of multidimensional photonic cluster states using time-delay feedback", Physical Review A **104**, 013703 (2021).

[171]O. Kaestle, R. Finsterhölzl, A. Knorr, and A. Carmele, "Continuous and time-discrete non-Markovian system-reservoir interactions: Dissipative coherent quantum feedback in Liouville space", Physical Review Research **3**, 023168 (2021).

[172]K. Vodenkova and H. Pichler, "Continuous Coherent Quantum Feedback with Time Delays: Tensor Network Solution", Physical Review X **14**, 031043 (2024).

[173]S. J. Whalen, "Collision model for non-Markovian quantum trajectories", Physical Review A **100**, 052113 (2019).

[174]D. A. B. Miller, "Quantum mechanics for scientists and engineers", in (Cambridge University Press, 2008) Chap. 14.

[175]M. Lax, "Formal Theory of Quantum Fluctuations from a Driven State", Physical Review **129**, 2342–2348 (1963).

[176]J. Dalibard, Y. Castin, and K. Mølmer, "Wave-function approach to dissipative processes in quantum optics", Physical Review Letters **68**, 580–583 (1992).

[177]L. Tian and H. J. Carmichael, "Quantum trajectory simulations of two-state behavior in an optical cavity containing one atom", Physical Review A **46**, R6801–R6804 (1992).

[178]R. Dum, A. S. Parkins, P. Zoller, and C. W. Gardiner, "Monte Carlo simulation of master equations in quantum optics for vacuum, thermal, and squeezed reservoirs", Physical Review A **46**, 4382–4396 (1992).

[179]A. Beige and G. C. Hegerfeldt, "Transition from antibunching to bunching for two dipole-interacting atoms", Physical Review A **58**, 4133–4139 (1998).

[180]S. Hughes and H. J. Carmichael, "Stationary inversion of a two level system coupled to an off-resonant cavity with strong dissipation", Phys. Rev. Lett. **107**, 193601 (2011).

[181]T. Vovk and H. Pichler, "Entanglement-Optimal Trajectories of Many-Body Quantum Markov Processes", Physical Review Letters **128**, 243601 (2022).

[182]W. Chen, M. Abbasi, Y. N. Joglekar, and K. W. Murch, "Quantum Jumps in the Non-Hermitian Dynamics of a Superconducting Qubit", Physical Review Letters **127**, 140504 (2021).

[183]T. Becker, C. Netzer, and A. Eckardt, "Quantum Trajectories for Time-Local Non-Lindblad Master Equations", Physical Review Letters **131**, 160401 (2023).

[184]X.-J. Yu, Z. Pan, L. Xu, and Z.-X. Li, "Non-Hermitian Strongly Interacting Dirac Fermions", Physical Review Letters **132**, 116503 (2024).

[185]G. Crowder, H. Carmichael, and S. Hughes, "Quantum trajectory theory of few-photon cavity-QED systems with a time-delayed coherent feedback", Physical Review A **101**, 023807 (2020).

[186]J. Butcher, "Numerical methods for ordinary differential equations in the 20th century", Journal of Computational and Applied Mathematics **125**, 1–29 (2000).

[187]N. Lambert et al., *QuTiP 5: The Quantum Toolbox in Python*, arXiv:2412.04705 [quant-ph], Dec. 2024.

[188]D. Cilluffo, A. Carollo, S. Lorenzo, J. A. Gross, G. M. Palma, and F. Ciccarello, "Collisional picture of quantum optics with giant emitters", Physical Review Research **2**, 043070 (2020).

[189]M. Bundgaard-Nielsen, D. Englund, M. Heuck, and S. Krastanov, "WaveguideQED.jl: An Efficient Framework for Simulating Non-Markovian Waveguide Quantum Electrodynamics", Quantum **9**, 1710 (2025).

[190]G. Crowder, L. Ramunno, and S. Hughes, "Quantum trajectory theory and simulations of nonlinear spectra and multiphoton effects in waveguide-QED systems with a time-delayed coherent feedback", Physical Review A **106**, 013714 (2022).

[191]H. Pichler, S. Choi, P. Zoller, and M. D. Lukin, "Universal photonic quantum computation via time-delayed feedback", Proceedings of the National Academy of Sciences **114**, 11362–11367 (2017).

[192]H. M. Wiseman and G. J. Milburn, *Quantum Measurement and Control* (Cambridge University Press, Oxford, 2002), p. 231.

[193]M. H. Muñoz-Arias, I. H. Deutsch, P. S. Jessen, and P. M. Poggi, "Simulation of complex dynamics of mean-field p-spin models using measurement-based quantum feedback control", Physical Review A **102**, 022610 (2020).

[194]A. Kubanek, M. Koch, C. Sames, A. Ourjoumtsev, P. W. H. Pinkse, K. Murr, and G. Rempe, "Photon-by-photon feedback control of a single-atom trajectory", Nature **462**, 898–901 (2009).

[195]G. G. Gillett, R. B. Dalton, B. P. Lanyon, M. P. Almeida, M. Barbieri, G. J. Pryde, J. L. O'Brien, K. J. Resch, S. D. Bartlett, and A. G. White, "Experimental feedback control of quantum systems using weak measurements", Phys. Rev. Lett. **104**, 080503 (2010).

[196]M. Rafiee, A. Nourmandipour, and S. Mancini, "Enforcing dissipative entanglement by feedback", Physics Letters A **384**, 126748 (2020).

[197]Z. Tan, P. A. Camati, G. C. Cauquil, A. Auffèves, and I. Dotsenko, "Alternative experimental ways to access entropy production", Phys. Rev. Research **3**, 043076 (2021).

[198]A. Di Giovanni, M. Brunelli, and M. G. Genoni, "Unconditional mechanical squeezing via backaction-evading measurements and nonoptimal feedback control", Physical Review A **103**, 022614 (2021).

[199]J. Kabuss, F. Katsch, A. Knorr, and A. Carmele, "Unraveling coherent quantum feedback for Pyragas control", Journal of the Optical Society of America B **33**, C10 (2016).

[200]P.-O. Guimond, H. Pichler, A. Rauschenbeutel, and P. Zoller, "Chiral quantum optics with V-level atoms and coherent quantum feedback", Physical Review A **94**, 033829 (2016).

[201]N. L. Naumann, S. M. Hein, M. Kraft, A. Knorr, and A. Carmele, "Feedback control of photon statistics", in Physics and Simulation of Optoelectronic Devices XXV, Vol. 10098 (Feb. 2017), 100980N.

[202]P. Forn-Díaz, C. Warren, C. Chang, A. Vadiraj, and C. Wilson, "On-Demand Microwave Generator of Shaped Single Photons", Physical Review Applied **8**, 054015 (2017).

[203]G. Calajó, Y.-L. L. Fang, H. U. Baranger, and F. Ciccarello, "Exciting a Bound State in the Continuum through Multiphoton Scattering Plus Delayed Quantum Feedback", Physical Review Letters **122**, 073601 (2019).

[204]A. Harwood, M. Brunelli, and A. Serafini, "Cavity optomechanics assisted by optical coherent feedback", Physical Review A **103**, 023509 (2021).

[205]J. T. Shen and S. Fan, "Coherent photon transport from spontaneous emission in one-dimensional waveguides", Optics Letters **30**, 2001 (2005).

[206]L. Zhou, Z. R. Gong, Y.-x. Liu, C. P. Sun, and F. Nori, "Controllable Scattering of a Single Photon inside a One-Dimensional Resonator Waveguide", Physical Review Letters **101**, 100501 (2008).

[207]P. Longo, P. Schmitteckert, and K. Busch, "Few-photon transport in low-dimensional systems", Physical Review A **83**, 063828 (2011).

[208]D. Roy, "Two-Photon Scattering by a Driven Three-Level Emitter in a One-Dimensional Waveguide and Electromagnetically Induced Transparency", Physical Review Letters **106**, 053601 (2011).

[209]W.-B. Yan and H. Fan, "Control of single-photon transport in a one-dimensional waveguide by a single photon", Physical Review A **90**, 053807 (2014).

[210]E. Sánchez-Burillo, D. Zueco, J. J. Garcia-Ripoll, and L. Martin-Moreno, "Scattering in the Ultrastrong Regime: Nonlinear Optics with One Photon", Physical Review Letters **113**, 263604 (2014).

[211]D. F. Kornovan, M. I. Petrov, and I. V. Iorsh, "Transport and collective radiance in a basic quantum chiral optical model", Physical Review B **96**, 115162 (2017).

[212]S. Mahmoodian, M. Cepulkovskis, S. Das, P. Lodahl, K. Hammerer, and A. S. Sørensen, "Strongly Correlated Photon Transport in Waveguide Quantum Electrodynamics with Weakly Coupled Emitters", Physical Review Letters **121**, 143601 (2018).

[213]A. P. Foster et al., "Tunable photon statistics exploiting the Fano effect in a waveguide", Physical Review Letters **122**, 173603 (2019).

[214]D. Mukhopadhyay and G. S. Agarwal, "Multiple Fano interferences due to waveguide-mediated phase coupling between atoms", Physical Review A **100**, 013812 (2019).

[215]D. Mukhopadhyay and G. S. Agarwal, "Transparency in a chain of disparate quantum emitters strongly coupled to a waveguide", Physical Review A **101**, 063814 (2020).

[216]S. Mahmoodian, G. Calajó, D. E. Chang, K. Hammerer, and A. S. Sørensen, "Dynamics of Many-Body Photon Bound States in Chiral Waveguide QED", Physical Review X **10**, 031011 (2020).

[217]H. Le Jeannic et al., "Experimental Reconstruction of the Few-Photon Nonlinear Scattering Matrix from a Single Quantum Dot in a Nanophotonic Waveguide", Physical Review Letters **126**, 023603 (2021).

[218]S. Arranz Regidor and S. Hughes, "Cavitylike strong coupling in macroscopic waveguide QED using three coupled qubits in the deep non-Markovian regime", Physical Review A **104**, L031701 (2021).

[219]A. Blais, J. Gambetta, A. Wallraff, D. I. Schuster, S. M. Girvin, M. H. Devoret, and R. J. Schoelkopf, "Quantum-information processing with circuit quantum electrodynamics", Physical Review A **75**, 032329 (2007).

[220]S. Kretschmer, K. Luoma, and W. T. Strunz, "Collision model for non-Markovian quantum dynamics", Physical Review A **94**, 012106 (2016).

[221]B. Zhang, S. You, and M. Lu, "Enhancement of spontaneous entanglement generation via coherent quantum feedback", Physical Review A **101**, 032335 (2020).

[222]C. Sommer, A. Ghosh, and C. Genes, "Multimode cold-damping optomechanics with delayed feedback", Physical Review Research **2**, 033299 (2020).

[223]U. Schollwoeck, "The density-matrix renormalization group in the age of matrix product states", Annals of Physics **326**, 96–192 (2011).

[224]R. Finsterhölzl, M. Katzer, A. Knorr, and A. Carmele, "Using Matrix-Product States for Open Quantum Many-Body Systems: Efficient Algorithms for Markovian and Non-Markovian Time-Evolution", Entropy **22**, 984 (2020).

[225]K. Mølmer, Y. Castin, and J. Dalibard, "Monte Carlo wave-function method in quantum optics", Journal of the Optical Society of America B **10**, 524 (1993).

[226]T. A. Brun, "A simple model of quantum trajectories", American Journal of Physics **70**, 719–737 (2002).

[227]P. Yao and S. Hughes, "Controlled cavity QED and single-photon emission using a photonic-crystal waveguide cavity system", Physical Review B **80**, 165128 (2009).

[228]C. Gonzalez-Ballestero, A. Gonzalez-Tudela, F. J. Garcia-Vidal, and E. Moreno, "Chiral route to spontaneous entanglement generation", Physical Review B **92**, 155304 (2015).

[229]B. le Feber, N. Rotenberg, and L. Kuipers, "Nanophotonic control of circular dipole emission", Nature Communications **6**, 6695 (2015).

[230]A. Young, A. Thijssen, D. Beggs, P. Androvitsaneas, L. Kuipers, J. Rarity, S. Hughes, and R. Oulton, "Polarization Engineering in Photonic Crystal Waveguides for Spin-Photon Entanglers", Physical Review Letters **115**, 153901 (2015).

[231]I. Söllner et al., "Deterministic photon–emitter coupling in chiral photonic circuits", Nature Nanotechnology **10**, 775–778 (2015).

[232]M. Scheucher, A. Hilico, E. Will, J. Volz, and A. Rauschenbeutel, "Quantum optical circulator controlled by a single chirally coupled atom", Science **354**, 1577–1580 (2016).

[233]J. Kabuss, A. Carmele, M. Richter, W. W. Chow, and A. Knorr, "Inductive equation of motion approach for a semiconductor QD-QED: Coherence induced control of photon statistics", Physica Status Solidi B **248**, 872–878 (2011).

[234]V. S. C. Manga Rao and S. Hughes, "Single quantum-dot Purcell factor and β factor in a photonic crystal waveguide", Physical Review B **75**, 205437 (2007).

[235]M. E. Reimer et al., "Overcoming power broadening of the quantum dot emission in a pure wurtzite nanowire", Physical Review B **93**, 195316 (2016).

[236]A. V. Kuhlmann, J. Houel, A. Ludwig, L. Greuter, D. Reuter, A. D. Wieck, M. Poggio, and R. J. Warburton, "Charge noise and spin noise in a semiconductor quantum device", Nature Phys **9**, 570–575 (2013).

[237]N. Somaschi et al., "Near-optimal single-photon sources in the solid state", Nature Photon **10**, 340–345 (2016).

[238]M. Edwards, "Effect of adiabatic and near-adiabatic field turn-on on the resonance fluorescence spectrum of a two-level atom", Journal of Physics B: Atomic and Molecular Physics **16**, 767–784 (1983).

[239]C. Gustin, R. Manson, and S. Hughes, "Spectral asymmetries in the resonance fluorescence of two-level systems under pulsed excitation", Optics Letters **43**, 779–782 (2018).

[240]B. Kannan et al., "Waveguide quantum electrodynamics with superconducting artificial giant atoms", Nature **583**, 775–779 (2020).

[241]A. Blais, S. M. Girvin, and W. D. Oliver, "Quantum information processing and quantum optics with circuit quantum electrodynamics", Nature Physics **16**, 247–256 (2020).

[242]M. Mirhosseini, E. Kim, X. Zhang, A. Sipahigil, P. B. Dieterle, A. J. Keller, A. Asenjo-Garcia, D. E. Chang, and O. Painter, "Cavity quantum electrodynamics with atom-like mirrors", Nature **569**, 692–697 (2019).

[243]H. J. Kimble, "The quantum internet", Nature **453**, 1023–1030 (2008).

[244]H. J. Kimble, M. Dagenais, and L. Mandel, "Photon antibunching in resonance fluorescence", Physical Review Letters **39**, 691 (1977).

[245]M. D. Eisaman, J. Fan, A. Migdall, and S. V. Polyakov, "Invited review article: single-photon sources and detectors", Review of Scientific Instruments **82** (2011).

[246]D. Toyli, A. Eddins, S. Boutin, S. Puri, D. Hover, V. Bolkhovsky, W. Oliver, A. Blais, and I. Siddiqi, "Resonance fluorescence from an artificial atom in squeezed vacuum", Physical Review X **6**, 031004 (2016).

[247]H. Kim, T. C. Shen, K. Roy-Choudhury, G. S. Solomon, and E. Waks, "Resonant interactions between a mollow triplet sideband and a strongly coupled cavity", Physical Review Letters **113**, 027403 (2014).

[248]J. R. Lakowicz, *Principles of fluorescence spectroscopy*, 3rd ed. (Springer, New York, NY, Aug. 2006).

[249]L. Masters, X.-X. Hu, M. Cordier, G. Maron, L. Pache, A. Rauschenbeutel, M. Schemmer, and J. Volz, "On the simultaneous scattering of two photons by a single two-level atom", Nature Photonics **17**, 972–976 (2023).

[250]F. Schuda, C. Stroud Jr, and M. Hercher, "Observation of the resonant stark effect at optical frequencies", Journal of Physics B: Atomic and Molecular Physics **7**, L198 (1974).

[251]C. Joshi, F. Yang, and M. Mirhosseini, "Resonance fluorescence of a chiral artificial atom", Physical Review X **13**, 021039 (2023).

[252]E. S. Redchenko, A. V. Poshakinskiy, R. Sett, M. Žemlička, A. N. Poddubny, and J. M. Fink, "Tunable directional photon scattering from a pair of superconducting qubits", Nature Communications **14**, 2998 (2023).

[253]X. Ruan, J.-H. Wang, D. He, P. Song, S. Li, Q. Zhao, L. Kuang, J.-S. Tsai, C.-L. Zou, J. Zhang, et al., "Dynamics and resonance fluorescence from a superconducting artificial atom doubly driven by quantized and classical fields", Physical Review Research **6**, 033064 (2024).

[254]K. Boos, S. K. Kim, T. Bracht, F. Sbresny, J. M. Kaspari, M. Cygorek, H. Riedl, F. W. Bopp, W. Rauhaus, C. Calcagno, et al., "Signatures of dynamically dressed states", Physical Review Letters **132**, 053602 (2024).

[255]J. C. López Carreño, S. Bermúdez Feijoo, and M. Stobińska, "Entanglement in resonance fluorescence", npj Nanophotonics **1**, 3 (2024).

[256]A. F. Kockum and F. Nori, "Quantum bits with Josephson junctions", in *Fundamentals and frontiers of the josephson effect* (Springer, 2019), pp. 703–741.

[257]X. Gu, A. F. Kockum, A. Miranowicz, Y.-x. Liu, and F. Nori, "Microwave photonics with superconducting quantum circuits", Physics Reports **718-719**, 1–102 (2017).

[258]P. Kurpiers, P. Magnard, T. Walter, B. Royer, M. Pechal, J. Heinsoo, Y. Salathé, A. Akin, S. Storz, J.-C. Besse, et al., "Deterministic quantum state transfer and remote entanglement using microwave photons", Nature **558**, 264–267 (2018).

[259]I.-C. Hoi, C. Wilson, G. Johansson, T. Palomaki, B. Peropadre, and P. Delsing, "Demonstration of a single-photon router in the microwave regime", Physical Review Letters **107**, 073601 (2011).

[260]I.-C. Hoi, T. Palomaki, J. Lindkvist, G. Johansson, P. Delsing, and C. Wilson, "Generation of nonclassical microwave states using an artificial atom in 1d open space", Physical Review Letters **108**, 263601 (2012).

[261]I.-C. Hoi, A. F. Kockum, T. Palomaki, T. M. Stace, B. Fan, L. Tornberg, S. R. Sathyamoorthy, G. Johansson, P. Delsing, and C. Wilson, "Giant cross–kerr effect for propagating microwaves induced by an artificial atom", Physical Review Letters **111**, 053601 (2013).

[262]P. Wen, A. Kockum, H. Ian, J. Chen, F. Nori, and I.-C. Hoi, "Reflective amplification without population inversion from a strongly driven superconducting qubit", Physical Review Letters **120**, 063603 (2018).

[263]W.-J. Lin, Y. Lu, P. Y. Wen, Y.-T. Cheng, C.-P. Lee, K. T. Lin, K. H. Chiang, M. C. Hsieh, C.-Y. Chen, C.-H. Chien, et al., "Deterministic loading of microwaves onto an artificial atom using a time-reversed waveform", Nano Letters **22**, 8137–8142 (2022).

[264]Y.-T. Cheng, C.-H. Chien, K.-M. Hsieh, Y.-H. Huang, P. Wen, W.-J. Lin, Y. Lu, F. Aziz, C.-P. Lee, K.-T. Lin, et al., "Tuning atom-field interaction via phase shaping", Physical Review A **109**, 023705 (2024).

[265]J. Zhang, Y.-x. Liu, R.-B. Wu, K. Jacobs, and F. Nori, "Quantum feedback: Theory, experiments, and applications", Physics Reports **679**, 1–60 (2017).

[266]M. H. Muñoz-Arias, P. M. Poggi, P. S. Jessen, and I. H. Deutsch, "Simulating Nonlinear Dynamics of Collective Spins via Quantum Measurement and Feedback", Physical Review Letters **124**, 110503 (2020).

[267]W.-M. Zhang, P.-Y. Lo, H.-N. Xiong, M. W.-Y. Tu, and F. Nori, "General Non-Markovian Dynamics of Open Quantum Systems", Physical Review Letters **109**, 170402 (2012).

[268]S.-L. Chen, N. Lambert, C.-M. Li, A. Miranowicz, Y.-N. Chen, and F. Nori, "Quantifying Non-Markovianity with Temporal Steering", Physical Review Letters **116**, 020503 (2016).

[269]G. Andersson, B. Suri, L. Guo, T. Aref, and P. Delsing, "Non-exponential decay of a giant artificial atom", Nature Physics **15**, 1123–1127 (2019).

[270]Y.-N. Lu, Y.-R. Zhang, G.-Q. Liu, F. Nori, H. Fan, and X.-Y. Pan, "Observing Information Backflow from Controllable Non-Markovian Multichannels in Diamond", Physical Review Letters **124**, 210502 (2020).

[271]G. Crowder, L. Ramunno, and S. Hughes, "Improving on-demand single-photon-source coherence and indistinguishability through a time-delayed coherent feedback", Physical Review A **110**, L031703 (2024).

[272]P. Stenius and A. Imamoglu, "Stochastic wavefunction methods beyond the Born - Markov and rotating-wave approximations", Quantum and Semiclassical Optics: Journal of the European Optical Society Part B **8**, 283–295 (1996).

[273]J. Koch, T. M. Yu, J. Gambetta, A. A. Houck, D. I. Schuster, J. Majer, A. Blais, M. H. Devoret, S. M. Girvin, and R. J. Schoelkopf, "Charge-insensitive qubit design derived from the Cooper pair box", Physical Review A **76**, 042319 (2007).

[274]F. Aziz, K.-T. Lin, P.-Y. Wen, Y.-C. Lin, E. Weigand, C.-P. Lee, Y.-T. Cheng, Y. Lu, C.-Y. Chen, C.-H. Chien, et al., "Nearly quantum-limited microwave amplification via interfering degenerate stimulated emission in a single artificial atom", npj Quantum Information **11**, 1–6 (2025).

[275]In the very strong coupling, any low-Q stray resonance mode along the waveguide will affect the data.

[276]B.-Y. Wu, Y.-T. Cheng, K.-T. Lin, F. Aziz, J.-C. Liu, K.-V. Rangdhol, Y.-Y. Yeung, S. Yang, Q. Shao, X. Wang, et al., "Microwave interference from a spin ensemble and its mirror image in waveguide magnonics", arXiv preprint arXiv:2409.17867 (2024).

[277]Y.-T. Cheng, K.-M. Hsieh, B.-Y. Wu, Z. Niu, F. Aziz, Y.-H. Huang, P. Wen, K.-T. Lin, Y.-H. Lin, J. Chen, et al., "Group delay controlled by the decoherence of a single artificial atom", arXiv preprint arXiv:2409.07731 (2024).

[278]S. Probst, F. Song, P. A. Bushev, A. V. Ustinov, and M. Weides, "Efficient and robust analysis of complex scattering data under noise in microwave resonators", Review of Scientific Instruments **86** (2015).

[279]The center peak in (a), (b), (h) and (d), (e) do not match because the excitation pump interfere with the emission.

[280]H.-P. Breuer, E.-M. Laine, J. Piilo, and B. Vacchini, "Colloquium: non-Markovian dynamics in open quantum systems", Reviews of Modern Physics **88**, 021002 (2016).

[281]F. Minganti, A. Miranowicz, R. W. Chhajlany, and F. Nori, "Quantum exceptional points of non-Hermitian Hamiltonians and Liouvillians: The effects of quantum jumps", Physical Review A **100**, 062131 (2019).

[282]C. Gneiting, A. V. Rozhkov, and F. Nori, "Jump-time unraveling of Markovian open quantum systems", Physical Review A **104**, 062212 (2021).

[283]M. Paul, J. Kettler, K. Zeuner, C. Clausen, M. Jetter, and P. Michler, "Metal-organic vapor-phase epitaxy-grown ultra-low density InGaAs/GaAs quantum dots exhibiting cascaded single-photon emission at 1.3 μm", Applied Physics Letters **106**, 122105 (2015).

[284]K. A. Fischer, K. Müller, K. G. Lagoudakis, and J. Vučković, "Dynamical modeling of pulsed two-photon interference", New Journal of Physics **18**, 113053 (2016).

[285]J. Iles-Smith, D. P. S. McCutcheon, A. Nazir, and J. Mørk, "Phonon scattering inhibits simultaneous near-unity efficiency and indistinguishability in semiconductor single-photon sources", Nature Photonics **11**, 521–526 (2017).

[286]D. Istrati et al., "Sequential generation of linear cluster states from a single photon emitter", Nature Communications **11**, 5501 (2020).

[287]P. Steindl et al., "Artificial Coherent States of Light by Multiphoton Interference in a Single-Photon Stream", Physical Review Letters **126**, 143601 (2021).

[288]J.-P. Li, J. Qin, A. Chen, Z.-C. Duan, Y. Yu, Y. Huo, S. Höfling, C.-Y. Lu, K. Chen, and J.-W. Pan, "Multiphoton Graph States from a Solid-State Single-Photon Source", ACS Photonics **7**, 1603–1610 (2020).

[289]M. Cosacchi, T. Seidelmann, M. Cygorek, A. Vagov, D. Reiter, and V. Axt, "Accuracy of the Quantum Regression Theorem for Photon Emission from a Quantum Dot", Physical Review Letters **127**, 100402 (2021).

[290]M. Richter and S. Hughes, "Enhanced TEMPO Algorithm for Quantum Path Integrals with Off-Diagonal System-Bath Coupling: Applications to Photonic Quantum Networks", Physical Review Letters **128**, 167403 (2022).

[291]D. Chruściński and A. Kossakowski, "Non-Markovian Quantum Dynamics: Local versus Nonlocal", Physical Review Letters **104**, 070406 (2010).

[292]M. N. Makhonin, J. E. Dixon, R. J. Coles, B. Royall, I. J. Luxmoore, E. Clarke, M. Hugues, M. S. Skolnick, and A. M. Fox, "Waveguide Coupled Resonance Fluorescence from On-Chip Quantum Emitter", Nano Letters **14**, 6997–7002 (2014).

[293]R. Uppu et al., "Scalable integrated single-photon source", Science Advances **6**, eabc8268 (2020).

[294]Ł. Dusanowski, C. Gustin, S. Hughes, C. Schneider, and S. Höfling, "All-Optical Tuning of Indistinguishable Single Photons Generated in Three-Level Quantum Systems", Nano Letters **22**, 3562–3568 (2022).

[295]R. H. Brown and R. Q. Twiss, "Correlation between Photons in two Coherent Beams of Light", Nature **177**, 27–29 (1956).

[296]C. K. Hong, Z. Y. Ou, and L. Mandel, "Measurement of subpicosecond time intervals between two photons by interference", Physical Review Letters **59**, 2044–2046 (1987).

[297]P. Schnauber, A. Singh, J. Schall, S. I. Park, J. D. Song, S. Rodt, K. Srinivasan, S. Reitzenstein, and M. Davanco, "Indistinguishable Photons from Deterministically Integrated Single Quantum Dots in Heterogeneous GaAs/Si3N4 Quantum Photonic Circuits", Nano Letters **19**, 7164–7172 (2019).

[298]M. Pechal, L. Huthmacher, C. Eichler, S. Zeytinoğlu, A. Abdumalikov, S. Berger, A. Wallraff, and S. Filipp, "Microwave-Controlled Generation of Shaped Single Photons in Circuit Quantum Electrodynamics", Physical Review X **4**, 041010 (2014).

[299]T. H. Stievater, X. Li, D. G. Steel, D. Gammon, D. S. Katzer, D. Park, C. Piermarocchi, and L. J. Sham, "Rabi Oscillations of Excitons in Single Quantum Dots", Physical Review Letters **87**, 133603 (2001).

[300]X. Ding et al., "On-Demand Single Photons with High Extraction Efficiency and Near-Unity Indistinguishability from a Resonantly Driven Quantum Dot in a Micropillar", Physical Review Letters **116**, 020401 (2016).

[301]N. Somaschi et al., "Near-optimal single-photon sources in the solid state", Nature Photonics **10**, 340–345 (2016).

[302]J. Liu et al., "A solid-state source of strongly entangled photon pairs with high brightness and indistinguishability", Nature Nanotechnology **14**, 586–593 (2019).

[303]P.-L. Ardelt et al., "Dissipative preparation of the exciton and biexciton in self-assembled quantum dots on picosecond time scales", Physical Review B **90**, 241404 (2014).

[304]J. Quilter, A. Brash, F. Liu, M. Glässl, A. Barth, V. Axt, A. Ramsay, M. Skolnick, and A. Fox, "Phonon-Assisted Population Inversion of a Single InGaAs/GaAs Quantum Dot by Pulsed Laser Excitation", Physical Review Letters **114**, 137401 (2015).

[305]R. Manson, K. Roy-Choudhury, and S. Hughes, "Polaron master equation theory of pulse-driven phonon-assisted population inversion and single-photon emission from quantum-dot excitons", Physical Review B **93**, 155423 (2016).

[306]M. Reindl, J. H. Weber, D. Huber, C. Schimpf, S. F. Covre da Silva, S. L. Portalupi, R. Trotta, P. Michler, and A. Rastelli, "Highly indistinguishable single photons from incoherently excited quantum dots", Physical Review B **100**, 155420 (2019).

[307]M. Cosacchi, F. Ungar, M. Cygorek, A. Vagov, and V. Axt, "Emission-Frequency Separated High Quality Single-Photon Sources Enabled by Phonons", Physical Review Letters **123**, 017403 (2019).

[308]S. Thomas et al., "Bright Polarized Single-Photon Source Based on a Linear Dipole", Physical Review Letters **126**, 233601 (2021).

[309]L. Hanschke, K. A. Fischer, S. Appel, D. Lukin, J. Wierzbowski, S. Sun, R. Trivedi, J. Vučković, J. J. Finley, and K. Müller, "Quantum dot single-photon sources with ultra-low multi-photon probability", npj Quantum Information **4**, 1–6 (2018).

[310]M. E. Ware, E. A. Stinaff, D. Gammon, M. F. Doty, A. S. Bracker, D. Gershoni, V. L. Korenev, S. C. Badescu, Y. Lyanda-Geller, and T. L. Reinecke, "Polarized Fine Structure in the Photoluminescence Excitation Spectrum of a Negatively Charged Quantum Dot", Physical Review Letters **95**, 177403 (2005).

[311]O. Gazzano, S. Michaelis de Vasconcellos, C. Arnold, A. Nowak, E. Galopin, I. Sagnes, L. Lanco, A. Lemaître, and P. Senellart, "Bright solid-state sources of indistinguishable single photons", Nature Communications **4**, 1425 (2013).

[312]C. Gustin, Ł. Dusanowski, S. Höfling, and S. Hughes, "Using the Autler-Townes and ac Stark effects to optically tune the frequency of indistinguishable single photons from an on-demand source", Physical Review Research **4**, 023045 (2022).

[313]C. Gustin and S. Hughes, "Efficient Pulse-Excitation Techniques for Single Photon Sources from Quantum Dots in Optical Cavities", Advanced Quantum Technologies **3**, 1900073 (2020).

[314]E. Schöll et al., "Crux of Using the Cascaded Emission of a Three-Level Quantum Ladder System to Generate Indistinguishable Photons", Physical Review Letters **125**, 233605 (2020).

[315]Z. Koong et al., "Coherent Dynamics in Quantum Emitters under Dichromatic Excitation", Physical Review Letters **126**, 047403 (2021).

[316]Y. Karli et al., "SUPER Scheme in Action: Experimental Demonstration of Red-Detuned Excitation of a Quantum Emitter", Nano Letters **22**, 6567–6572 (2022).

[317]T. K. Bracht, M. Cygorek, T. Seidelmann, V. M. Axt, and D. E. Reiter, "Temperature-independent almost perfect photon entanglement from quantum dots via the SUPER scheme", Optica Quantum **1**, 103–107 (2023).

[318]C. G. Torun et al., *SUPER and subpicosecond coherent control of an optical qubit in a tin-vacancy color center in diamond*, arXiv:2312.05246 [quant-ph], Dec. 2023.

[319]N. Heinisch, N. Köcher, D. Bauch, and S. Schumacher, "Swing-up dynamics in quantum emitter cavity systems: Near ideal single photons and entangled photon pairs", Physical Review Research **6**, L012017 (2024).

[320]L. Vannucci and N. Gregersen, "Highly efficient and indistinguishable single-photon sources via phonon-decoupled two-color excitation", Physical Review B **107**, 195306 (2023).

[321]M. M. T. Loy, "Observation of Population Inversion by Optical Adiabatic Rapid Passage", Physical Review Letters **32**, 814–817 (1974).

[322]V. Malinovsky and J. Krause, "General theory of population transfer by adiabatic rapid passage with intense, chirped laser pulses", The European Physical Journal D - Atomic, Molecular, Optical and Plasma Physics **14**, 147–155 (2001).

[323]D. P. S. McCutcheon and A. Nazir, "Quantum dot Rabi rotations beyond the weak exciton–phonon coupling regime", New Journal of Physics **12**, 113042 (2010).

[324]D. P. S. McCutcheon, N. S. Dattani, E. M. Gauger, B. W. Lovett, and A. Nazir, "A general approach to quantum dynamics using a variational master equation: Application to phonon-damped Rabi rotations in quantum dots", Physical Review B **84**, 081305 (2011).

[325]A. Nazir and D. P. S. McCutcheon, "Modelling exciton–phonon interactions in optically driven quantum dots", Journal of Physics: Condensed Matter **28**, 103002 (2016).

[326]A. J. Ramsay, T. M. Godden, S. J. Boyle, E. M. Gauger, A. Nazir, B. W. Lovett, A. M. Fox, and M. S. Skolnick, "Phonon-Induced Rabi-Frequency Renormalization of Optically Driven Single InGaAs/GaAs Quantum Dots", Physical Review Letters **105**, 177402 (2010).

[327]S. Weiler, A. Ulhaq, S. M. Ulrich, D. Richter, M. Jetter, P. Michler, C. Roy, and S. Hughes, "Phonon-assisted incoherent excitation of a quantum dot and its emission properties", Phys. Rev. B **86**, 241304 (2012).

[328]T. K. Bracht, T. Seidelmann, T. Kuhn, V. M. Axt, and D. E. Reiter, "Phonon Wave Packet Emission during State Preparation of a Semiconductor Quantum Dot using Different Schemes", Physica Status Solidi (b) **259**, 2100649 (2022).